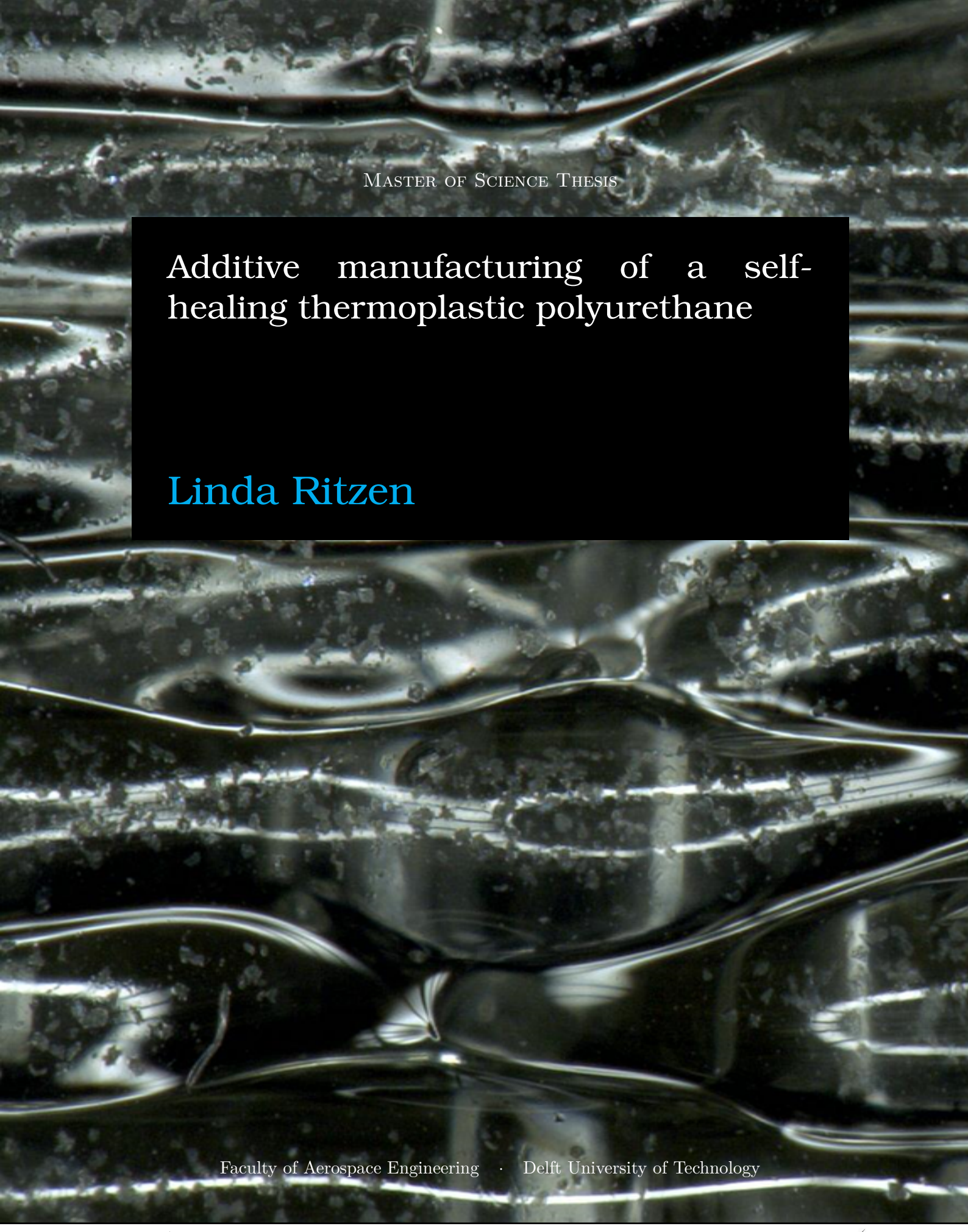

Master of Science Thesis

# Additive manufacturing of a self-healing thermoplastic polyurethane

Linda Ritzen

Faculty of Aerospace Engineering · Delft University of Technology

TU Delft Delft University of Technology

# Additive manufacturing of a self-healing thermoplastic polyurethane

Master of Science Thesis

For obtaining the degree of Master of Science in Aerospace Engineering
at Delft University of Technology

Linda Ritzen

May 20th, 2020

Faculty of Aerospace Engineering · Delft University of Technology

Delft University of Technology
Faculty of Aerospace Engineering
Department of Aerospace Structures and Materials

**GRADUATION COMMITTEE**

Dated: May 20th, 2020

Chair holder:

Prof.Dr.Ir. Sybrand van der Zwaag

Committee members:

Dr. Santiago J. García Espallargas (mentor)

Dr. Irene Fernandez Villegas

Dr. Kunal Masania

# Abstract

Additive manufacturing of smart polymers is a rapidly growing field. Additive manufacturing presents a versatile, low-waste manufacturing method for functional materials. Self-healing polymers are a type of smart polymers that are able to mend damage, either by the incorporation of an encapsulated healing agent or by intrinsic polymer design. Beside this ability to repair damage, certain types of self-healing polymers have also shown to improve interlayer adhesion of 3D printed parts due to the formation of reversible cross-links.

This thesis demonstrated the additive manufacturing of a self-healing polyurethane (CR1) by fused deposition modelling. A protocol was established in order to print with this self-healing polyurethane while minimising material loss. Measurable polymer properties that were relevant to fused deposition modelling were identified and measured in order to establish the processing window of the polymer. CR1 was synthesised, processed into a filament using a commercial filament maker and successfully printed using a modified commercial 3D printer. The elastomeric nature of the polymer combined with its high sensitivity to temperature, resulted in a narrow printing window. Beside the ability to 3D print the polymer into rectangular bars, the self-supportability of the 3D printed CR1 was demonstrated by the printing of a single-wall structure. Printing at 230 °C and 20 mm/s resulted in the most regular sample, with a very low void concentration in its cross-section.

In order to characterise the mechanical properties of the 3D printed self-healing polyurethane, a compression cut-test was employed. This test was used as a qualitative mechanical test for small quantities of polymer. The 3D printed thermoplastic polyurethane was compared to the bulk of this polymer, and also to a commercial 3D printing thermoplastic polyurethane material (Ninjaflex). The mechanical response of 3D printed CR1 showed good resemblance to that of the bulk. Furthermore, the test showed that the polymer retained its self-healing ability after printing.

# Table of Contents

# List of Figures

# List of Tables

# Nomenclature

## Symbols

| Symbol | Definition |
|---|---|
| $\beta$ | Cone angle |
| $\dot{\gamma}$ | Shear rate |
| $\eta$ | viscosity |
| $\tau$ | shear stress |
| $A$ | Area |
| $d_{infill}$ | Infill distance |
| $D$ | Diameter |
| $E'$ | Storage/elastic modulus |
| $E$" | Loss/viscous modulus |
| $G'$ | Storage/elastic shear modulus |
| $G$" | Loss or viscous shear modulus |
| $K$ | flow consistency index |
| $L$ | Length |
| $n$ | power-law constant |
| $P$ | Pressure |
| $Q$ | Volumentric flow rate |
| $r$ | Distance from the centre of a circle |
| $R$ | Radius |
| $T$ | Temperature |
| $T_d$ | Thermal degradation temperature |
| $T_g$ | Glass transition temperature |
| $T_m$ | Melting temperature |
| $T_{print}$ | Printing temperature |
| $\tan(\delta)$ | Shift between the elastic and viscous response |
| $v$ | Velocity |
| $V_{print}$ | Print-speed |

## Abbreviations

| Abbreviation | Definition |
|---|---|
| 3D | Three-dimensional |
| ABS | Acrylonitrile butadiene styrene |
| AM | Additive manufacturing |
| ATR | Attenuated total reflection |
| CAD | Computer aided design |
| D | Domains |
| DIC | Digital image correlation |
| DA | Diels-Alder |
| DART | Diels-Alder reversible thermoset |
| DCB | Double cantilever beam |
| DIW | Direct ink writing |
| DMTA | Dynamic mechanical thermal analysis |
| EHD | 2-Ethyl-1,3-Hexanediol |
| FDM | Fused deposition modelling |
| FFF | Fused filament fabrication |
| fmDA | Furan-maleimide |
| FTIR | Fourier transform infrared spectroscopy |
| LDM | Liquid deposition modelling |
| M | Matrix |
| MDI | 4,4'-Methylenebis(phenyl isocyanate) |
| PC | Polycarbonate |
| PCL | Polycaprolactone |
| PEI | Polyetherimide |
| PLA | Polylactic acid |
| STL | Stereolithography |
| TGA | Thermogravimetric analysis |
| TMA | Thermomechanical analysis |
| TPU | Thermoplastic polyurethane |
| UPyMA | Ureidopyrimidinone methacrylate |
| UV | Ultraviolet |

# Acknowledgments

Finishing this thesis would not have been possible without the support I've received from so many people. I would like to thank my supervisor, Santiago Garcia, for his mentorship throughout the thesis. His feedback and abundance of ideas definitely helped me a lot and kept me going. I would also like to thank Sybrand van der Zwaag, whose ideas and critical questions have helped me to improve the quality of my work. Thank you to Vincenzo Montano, for always answering my questions and helping me in the lab. Special thanks go out to Ana Infante Petidier, thank you so much for all your help and for the pleasant discussions about this work.

I would like to thank all the other NovAM members, and especially Shanta for keeping the group running. I feel so lucky to have been able to work in such an internationally diverse and open group, and I have felt very supported during the good and bad times of the past year.
I would also like to thank all the staff of the Delft Aerospace Structures and Materials Laboratory, especially Marlies Nijemeisland, Durga Mainali Sharma and Johan Bijleveld, for helping me with my lab-work. Special thanks go out to Gertjan Mulder, for his help in the work of the thesis, but definitely also for the mental support and company during long days in the lab.
I would like to thank Patricia Parlevliet, for our lovely conversations during my internship at Airbus and after, helping me grow as an engineer and a researcher.
I would like to thank all my friends for supporting me throughout the past years and helping me take my mind off of the thesis work. Special thanks to Laura and Krista for proofreading this report.

I would like to thank Luc, for standing by me for the past five and a half years, keeping me motivated and helping me out so much.

Ten slotte wil ik graag mijn ouders, Lenie en Jos, en mijn broertje Joeri bedanken, omdat jullie me altijd in al mijn keuzes hebben gesteund en geholpen.

"Als ik mien oege sloet, zij ik elke dag wat mier. De werlt is groet, in mien durp an de rivier."

— *Jack Poels (Rowwen Hèze) in Auto, Vliegtuug*

# Chapter 1

# Introduction

Additive manufacturing (AM), or three-dimensional (3D) printing, of smart polymers is a rapidly growing field [1, 2]. AM is defined as "the process of joining materials to make parts from 3D model data, usually layer upon layer as opposed to subtractive manufacturing and formative manufacturing methodologies" [3]. During subtractive manufacturing, a part is made by cutting away material from a solid piece of material. A major disadvantage of this method of manufacturing is the inevitability of waste. During formative manufacturing of polymers, the material is liquefied and formed by means of a mould. Although the waste of this method is lower, the method requires a mould that can quickly become complex and expensive. One of the largest benefits of AM is the possibility to manufacture complex structures that would normally require the production of many parts as a single, optimised part without the need for a mould and with relatively little waste.

AM presents a versatile, minimum-waste manufacturing method for smart materials, which are often expensive to manufacture. As a result, additive manufacturing of smart materials has become a rapidly growing field [1]. Moreover, high performance industries that increasingly apply smart polymers, for example the aerospace field, also benefit from an easily adaptable manufacturing method due to their highly customised applications.

Within the aerospace industry, the vast majority of parts produced by AM are made of metal. Metal AM can produce reliable, high quality parts that have been incorporated on for example the Ariane 6 propulsion module, where nearly 250 parts could be condensed into a single element, cutting costs by half, and reducing the production time from months to days[1]. Or Boeing, that used AM to produce replacement parts for its aircraft as well as satellite parts[2]. In the polymer field, the Airbus A350 XWB aircraft contained over 1000 parts produced by AM, made of polyetherimide (PEI)[3]. The weight reduction of the parts ranged from 33% up to to 55%, and raw material usage was decreased by 90%.

[1] https://www.eos.info/press/case_studies/future-ariane-propulsion-module-simplified-with-\3d-printing accessed October 7, 2019

[2] https://www.boeing.com/features/innovation-quarterly/nov2017/feature-thought-leadership-\3d-printing.page accessed October 7, 2019

[3] https://3dprint.com/63169/airbus-a350-xwb-3d-print/ accessed October 7, 2019

This chapter aims to familiarise the reader with the topic of this thesis: the AM of a self-healing thermoplastic polyurethane. Section 1.1 provides an introduction to the fused deposition modelling (FDM) process as a method of 3D printing. Section 1.2 establishes some measurable parameters during filament making and FDM. Section 1.3 discusses the state of the art of extrusion-based AM with self-healing polymers. Section 1.4 discusses some common mechanical tests used to characterise 3D printed parts. Section 1.5 introduces the type of polymer used in this work, a thermoplastic polyurethane. In section 1.6, a protocol for the FDM of a self-healing polyurethane is established. Section 1.7 presents the scope of this thesis and section 1.8 gives an overview of the outline of the report.

## 1.1 The fused deposition modelling process

Fused deposition modelling (FDM), also known as Fused Filament Fabrication (FFF), is an extrusion based AM process for polymers, and the most commonly used process for both amateur and professional applications [4]. The process always starts with a 3D solid computer-aided design (CAD) model in a so-called stereolithography (STL) format. In an STL file, the model is reduced into triangles. The file is then processed by a slicer, which produces a G-code consisting of commands that the printer can execute.

### FDM set-up

There are various layouts of an FDM system, but a number of components can always be distinguished, which are shown in figure 1.1. FDM machines use a filament as the input material, which is moved by gears in a feeder system. The filament is pushed through a filament guide towards the heater block. This block is heated to a set temperature such that the material can be molten and pushed out through the nozzle. The print is then created layer by layer on a print bed that is also heated in some cases.

An alternative that is in many ways similar to FDM is liquid deposition modelling (LDM), or sometimes referred to as direct ink writing (DIW) [4]. The difference between the systems is that the print-head is replaced by a syringe, and the input material is therefore also not a filament. A FDM printer can be turned into a LDM printer with some minor alterations. An advantage of this method is the improved control of the pressure throughout the system since it is directly driven by the syringe rather than by incoming filament [5]. This is especially relevant for soft materials that show pronounced shear thinning at low temperatures. Nevertheless, FDM may have an advantage over LDM when larger parts are concerned. Moreover, when printing needs to occur at temperatures beyond the thermal degradation of the polymer, the residence time of a polymer at this high temperature is greatly reduced in FDM compared to LDM.

[4] https://www.statista.com/statistics/756690/worldwide-most-used-3d-printing-technologies/ accessed October 7, 2019

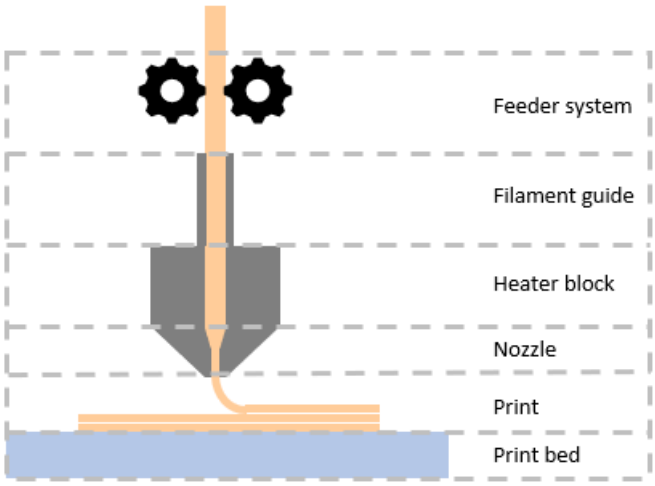


**Figure 1.1:** Schematic overview of the FDM process, divided into some key components.

### Benefits of FDM

AM methods such as FDM have several benefits compared to conventional manufacturing techniques. They enable the production of geometries that cannot be produced by other manufacturing methods, for instance those obtained from topology optimisation [6]. Moreover, this increase in complexity is often not accompanied by an increase in manufacturing costs, since no additional expertise or parts are required when the part is more or less complex. AM improves resource efficiency by reducing waste associated with conventional manufacturing processes [7]. These advantages are highlighted for applications that have low production volumes. In this case, the need for a mould is mitigated, reducing time and costs. Moreover, the waste of the method is lower compared to that of subtractive manufacturing processes such as milling [8]. For moulded parts, the significance of these advantages decreases as the production volume increases, but for some parts AM will always remain beneficial. Based on this, the choice for AM as opposed to other manufacturing methods should depend on the production volume and complexity of a part. In this case, a 3D printer and raw material are the only requisites for a wide variety of parts.

### Challenges in FDM

There remain, however, several challenges that have restricted most polymer AM methods, and FDM in particular, to non-load-bearing and prototyping applications. At the time of writing, the ASTM F2924-14 standard for AM of Titanium-6 Aluminium-4 Vanadium by powder bed fusion had been the only official standard in additive manufacturing [9]. The polymer AM field still lacks standardisation. In order to work towards the broader application of parts 3D printed using FDM, the quality of the parts needs to be increased, controlled and understood.

One of the most prominent disadvantages of FDM is inherent to the basis of the process itself, namely to the layer-by-layer deposition. The approach to building a part out of strands leaves the part with a high porosity [10], as seen in figure 1.2. Additionally, in most cases,

FDM relies on the melting of a polymer, which precludes the use of permanently cross-linked thermosets without additional steps such as post-curing. Instead, conventional thermoplastics are used, which typically rely on tangling of the polymer chains for their strength. Since a deposited layer has already partially cooled down by the time the next layer of material is deposited, there is limited opportunity for this tangling. As a consequence, the interlayer strength in parts produced by FDM is comparatively low and by extent, the anisotropy is high [11].

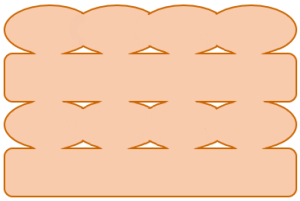

**Figure 1.2:** Schematic of the cross-section of a part produced by FDM using a [90/0] printing orientation.

### Reducing anisotropy through printing parameters

Various efforts have been made to reduce anisotropy in parts produced by FDM through process parameters, experimentally as well as numerically [12]. Air-gaps between the rows turned out to have a significant influence on the isotropy [13, 14, 15]. Through obtaining a negative air-gap, i.e. creating an overlap between two rows of material in the same layer, the anisotropy could be reduced. The direction of printing (called the raster orientation) also affected anisotropy [13, 16, 17, 15]. If the part was built using only layers in the direction parallel to a load, it would be relatively strong in tension [13, 16]. However, if the part was built with a raster orientation transverse to the load, it was relatively weak since the strength depends on the adhesion [13, 16]. The part printed in a [+45/-45] orientation failed in shear [13]. However, the layer orientation was also found to influence the residual stresses present in the print, where long rows of material increased the residual stresses at the detriment of the mechanical properties [17]. Increasing layer thickness was also shown to reduce residual stresses in the material, increasing the overall quality [17], although an increase in air gaps would decrease mechanical performance.

## 1.2 Identifying measurable parameters during filament making and FDM

While in theory, there are many methods to create a polymer filament, most commercially available filament makers rely on melt extrusion. Examples of systems that were commercially available at the time of writing were the Felfil filament maker [5] the Filabot series [6] and 3DEVO's composer and precision lines [7]. Each of these machines rely on melt extrusion

[5] https://felfil.com/, accessed 27 December 2019
[6] https://www.filabot.com/ accessed 27 December 2019
[7] https://3devo.com/filament-makers/, accessed 27 December 2019

to create filament. Therefore, the methodology will limit itself to filament making by melt extrusion. They each contain a single-screw extrusion system. The flow in extruder has already been extensively studied and described [18]. If the geometry of the extruder is well known, one can calculate the flow of certain materials in an extruder with high accuracy. However, in this thesis, the geometry of the extruder screw was unknown, since it was not published and the channel could not be disassembled. Therefore, no exact calculations could be made. Only the basic principles of the flow will be described here.

It could be argued that FDM is also a type of melt extrusion, since it relies on extruding the filament through a nozzle [8]. Instead of a screw, FDM uses pressure generated by the filament itself for extrusion. This means that the material properties relevant to filament making can also be applied to FDM. Nevertheless, there are additional material properties that can be relevant for FDM. Since the properties of the filament maker and FDM system were unknown, the methodology was based on the basic principles of melt-based extrusion. Therefore, several properties of the melt-flow behaviour of polymers will be discussed.

### Melt-flow behaviour

Characterisation of the melt flow properties of the polymer by rheology is very important in the analysis of extrusion processes. Specifically, the changing velocity of the flow throughout the system, described by the shear rate ($\dot{\gamma}$). If the viscosity ($\eta$) and the shear stress ($\tau$) of a fluid are independent of the shear rate, the fluid is considered Newtonian. If they change with the shear rate, the fluid is considered non-Newtonian, or a power-law fluid. The behaviour of these fluids is described by equation (1.1) and (1.2).

$$\tau = K \cdot \dot{\gamma}^n \tag{1.1}$$

$$\eta = K \cdot \dot{\gamma}^{n-1} \tag{1.2}$$

$K$ is the flow consistency index and $n$ is the power-law constant. If $n < 1$, the viscosity decreases with an increasing shear rate and the fluid is shear-thinning. If $n > 1$, the fluid is shear-thickening, and if $n = 1$, the fluid is Newtonian. Figure 1.3 shows the behaviour of Newtonian and non-Newtonian liquids according to equation (1.1) and 1.2. In reality, at low shear rates, polymers act like a Newtonian fluid. Shear thinning behaviour is favourable during processes such as FDM. Ideally, the increase in shear rate during the extrusion reduces the viscosity of the polymer, which increases again once it has been extruded such that the polymer can maintain its shape. The shear rate throughout the system depends on the diameter throughout the nozzle and on the speed of printing. Shear thinning behaviour also depends on the temperature of the polymer, which changes throughout the system.

### Pressure build-up during FDM

At the time of writing, various efforts at establishing numerical and analytical models of FDM had already been reported, to various degrees of success [19, 20]. These works focus on particular aspects of the FDM process, such as polymer flow in the nozzle [21, 22], residual stresses after deposition [23] and filament buckling [10]. Most of these works could not be

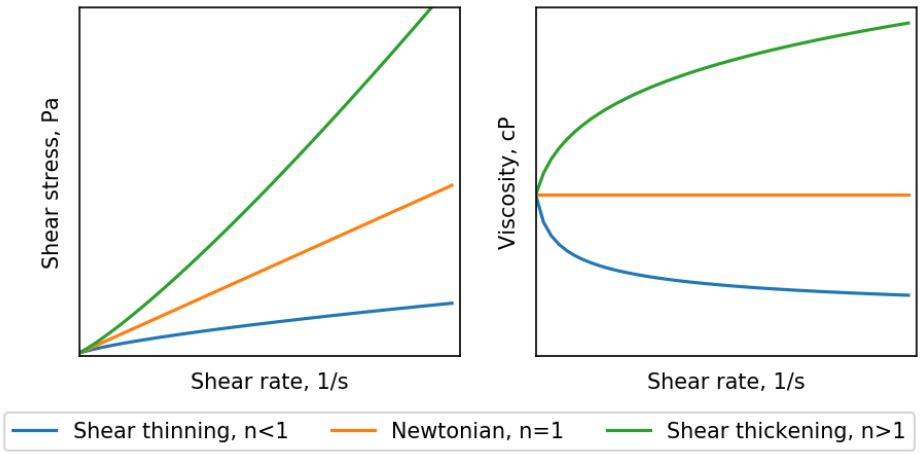


**Figure 1.3:** Flow curves of fluids with different power law coefficients.

fully validated with experiments [20]. Moreover, combining these models into a full analysis of the FDM process was neither the goal of this work, nor a feasible endeavour at the time of writing. Therefore, priorities were made in the aspects of the FDM process that would be considered. With the goal of being able to print with a novel material in mind, the flow dynamics and the pressure build-up during printing of the polymer were considered to be of primary importance.

There have been some efforts to quantify the pressure change that occurs during printing, much of it based on the work of Bellini et al. [21]. A mathematical model was developed to create a feedback system that would change the print speed based on the pressure drop in the nozzle. The hot-end of the printer is essentially divided into three sections as seen in figure 1.4:

- Section I: entrance of the nozzle whose diameter ($D_1$) is equal to the diameter of the filament, and with length $L_1$. The material is assumed to already have attained the printing temperature at this point.
- Section II: where the diameter of the nozzle changes from the diameter of the filament to the diameter of the nozzle exit with the cone angle ($\beta$).
- Section III: exit of the nozzle with diameter $D_2$ and length $L_2$.

The total pressure change in the nozzle was calculated by adding the pressure change ($\Delta P$) in each of the sections for a certain velocity in section I ($v$), according to equations (1.3) to (1.5) [21].

$$\Delta P_1 = 2L_1 \left(\frac{v}{K}\right)^{1/n} \left(\frac{n+3}{(D_1/2)^{n+1}}\right)^{1/n} \tag{1.3}$$

$$\Delta P_2 = \left(\frac{2 \cdot n}{3 \cdot tan(\beta/2)}\right) \left(\frac{1}{D_2^{3/n}} - \frac{1}{D_1^{3/n}}\right) \left(\left(\frac{D_1}{2}\right)^2 (n+3) \cdot 2^{n+3}\right)^{1/n} \tag{1.4}$$

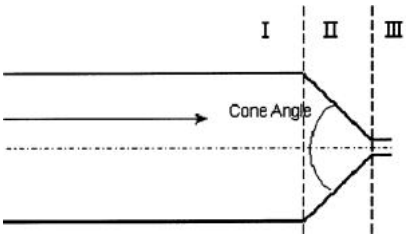


**Figure 1.4:** Hot-end simplified into three sections: section I at the entrance, section II where the diameter reduces to the diameter of section III, which is the exit [21].

$$\Delta P_3 = 2L_2 \left(\frac{v}{K}\right)^{1/n} \left(\frac{(n+3)(D_1/2)^2}{(D_2/2)^{n+3}}\right)^{1/n} \tag{1.5}$$

Although the model has been compared to finite element analyses, it had not been implemented successfully [22, 24, 21]. It does suggest that in order to reduce the change in pressure, the ratio $D_1/D_2$ could be decreased. The relationship between velocity and change in pressure is more complex, since this also influences the temperature of the material and the shear rate, which in turn influence the constants in the power law (equation (1.1)).

### Flow in the nozzle during FDM

The power-law constants can be used to describe flow with velocity components in a single direction. In order to correlate the printing results to the viscosity during printing, a relationship between the printing speed and the shear rate was established. In order to be able to quantify the flow, three key assumptions were made. Firstly, the flow was assumed to be incompressible; secondly, the flow was assumed to be fully developed at this point; thirdly, the flow velocity at the wall is assumed to be 0 (hence that there was no slipping).

Figure 1.5 shows a diagram representing the flow in the nozzle. With the assumptions that were made, the velocity profile of the liquid in the nozzle could be expressed as a function of the distance from the centre of the tube ($r$) by equation (1.6) [25]. $Q$ is the volumetric flow rate, $n$ is the power law constant and $R$ is the radius of the tube. The shear rate is the derivative of this function with respect to $r$, described in equation (1.7). Knowing the diameter of the printer nozzle, these relationships can provide an estimate of the shear rate during printing.

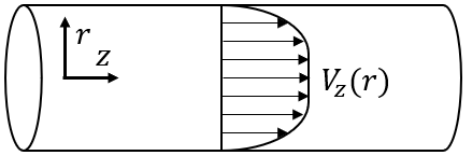


**Figure 1.5:** Simplified model of the flow in the nozzle of the printer, showing the velocity profile of the molten polymer.

$$V_z(r) = \frac{3n+1}{n+1}\left[1-\left(\frac{r}{R}\right)^{n+\frac{1}{n}}\right]\frac{Q}{\pi R^2} \tag{1.6}$$

$$|\dot{\gamma}(r)| = \frac{dV_z}{dr} = \frac{3n+1}{n}\left[\frac{r}{R}\right]^{\frac{1}{n}}\frac{Q}{\pi R^3} \tag{1.7}$$

Beside the polymer melt-dynamics, the heat transfer in the hot section of the print-head and the heat transfer through the filament would also significantly impact printing. In self-healing polymers, it is often desirable to experience a significant increase in mobility at moderate temperatures to facilitate healing. Within this context, that means that the polymer could have a significantly lower buckling force even at moderate temperatures. Finite element analyses have been used to calculate the temperature gradient throughout the filament during FDM [24]. This distribution is very much dependent on the print-head (geometry, materials, cooling system) of the set-up used, the properties of the material itself, the dimensions of the filament and the print-speed used. Within the scope of this thesis, such analyses could not be performed.

## 1.3 3D printing and self-healing materials

AM of self-healing materials has been a topic of increasing interest for reasons other than reduced anisotropy. On the one hand, AM provides a versatile manufacturing method for these materials. On the other hand, the dynamic and self-recovering properties of these materials could extend the lifetime of these parts [1, 26].

### About self-healing materials

While there are many approaches and chemistries to achieve self-healing behaviour in polymers, the process of healing follows a certain sequence of events, which starts when a damage is inflicted onto the material, as described by Hager et al. [27]. The healing process relies on the formation of a mobile phase within the material, ideally triggered by the occurrence of the damage or otherwise by an external stimulus. This mobile phase can travel to the damaged volume where the damage is (partially) mended, and the phase is immobilised again. This local, temporary mobility can be enabled by various mechanisms and as a reaction to various triggers, depending on the material. Research on self-healing materials has often focused on the recovery of mechanical properties, but other properties can also be healed, such as corrosion protection, adhesion and hydrophobicity [28].

### Extrinsically self-healing materials

In the so-called extrinsic approach, an encapsulated mending agent is released as a response to the damage which then mends the material [29]. Common encapsulation strategies are the use of microcapsules [30], fibres [31], or even microvascular networks inspired by the human skin [32]. In an extrinsically self-healing material, the damage acts as a trigger for healing to occur, which eliminates the need for an external stimulus. However, once the encapsulated

healing agent has been released, healing cannot be repeated in that area. Moreover, the material needs to be designed in such a way that the crack is directed towards the healing particle, that it breaks the particle and that the volume of the crack can be filled sufficiently by the volume of that particle [33].

AM has been an attractive manufacturing method for microvascular networks, since a 3D network can be printed and then dissolved, leaving hollow fibres that can be filled with healing agent [32]. Hansen et al. [34] used liquid deposition modelling and two fugitive inks to print a dual microvascular network that was then covered with epoxy. One network contained epoxy resin and the other an epoxy hardener. Wu et al. [35] created a microvascular network by printing a fugitive ink into a supporting photo-curable gel reservoir. The system was cured and the fugitive ink was dissolved and removed, after which it could be filled with a healing agent.

### Intrinsically self-healing materials

An alternative to the extrinsic healing mechanism is intrinsic healing, where the healing properties of the material are inherent to the material itself. In intrinsically self-healing polymers, the healing ability relies on the dynamic nature of the interactions between polymer chains, often as a result of dynamic or reversible bonds which can be chemical and/or physical in nature [28]. An example of these reversible bonds are the Diels-Alder bonds used in the research of Davidson et al., Appuhamillage et al. and Yang et al. [36, 26, 37]. In intrinsically self-healing polymers, healing can be repeated a multitude of times in the same area and the requirement of a crack piercing a certain area before growing beyond a certain volume is mitigated. However, in many cases, an external trigger such as heat is required to facilitate the healing process.

AM of intrinsically healing polymers has gained increasing attention over the past years [1]. Overall, LDM has been the preferred method for AM of self-healing polymers, since it mitigates requirement for a filament. The quality of the filament has a great influence on the printing process and the quality of the outcome.

**Hydrogels** Particularly hydrogels have been showing high potential for LDM, since they can be tailored to show shear-thinning behaviour that allows for extrusion at ambient temperatures [38, 39]. The shear stress required for extrusion can be determined through rheological measurements and easily replicated by the syringe. Ideally, the material should behave like a solid where the store, or elastic, modulus ($G'$) should be greater than the loss, or viscous, modulus ($G$”) at low shear rates while being smaller at the shear rate of extrusion [5]. In the case of cross-linked hydrogels, a post-treatment has been a necessity in most cases [40, 39, 41].

**Other self-healing polymers** Beside hydrogels and the work of Yang and co-workers mentioned in section 1.1, there are several other reports of LDM with self-healing materials. For instance, the LDM of polymers that aim to recover properties other than mechanical integrity, such as electrical conductivity [42, 43]. In an effort to increase the mechanical properties of

the printed material, Kuang et al. [44] used a resin that was photocured by ultraviolet (UV) radiation upon deposition. The resin was aliphatic urethane diacrylate, blended with polycaprolactone (PCL), with the inclusion of Silicon oxide nanoparticles in order to tune the rheological behaviour. The polymer retained its self-healing behaviour after printing. They printed a variety of 3D structures, which can be seen in figure 1.6.

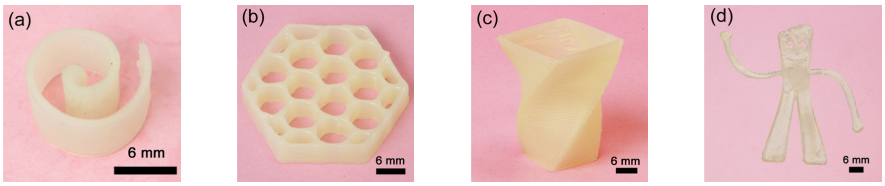


**(a)** Archemedian spiral. **(b)** Honeycomb. **(c)** Hollow vase. **(d)** Gumby model.

**Figure 1.6:** Pictures of three-dimensional structures printed by UV-assisted LDM of a blend of aliphatic urethane diacrylate blended with PCL and Silicon oxide nanoparticles [44].

FDM has thus far been a less popular method to print self-healing polymers. The need for a filament requires more material and there is less control of the process since the pressure is applied indirectly by the incoming material. However, FDM has certain advantages over LDM. The volume of the print is not restricted to the volume of the syringe but instead to the amount of filament available. If the polymer cannot reach the required viscosity at temperatures before its thermal degradation temperature, FDM can be the preferred option since the residence time of the polymer under this heat is lower.

A successful example of a self-healing polymer that can be 3D printed using FDM is Surlyn ionomer by Dupont. Surlyn is known to have self-healing properties as a response to ballistic impact [45], and has shown to restore mechanical properties after cutting [46]. Surlyn is an ionomer, whose self-healing behaviour has been attributed to the formation of dynamic cross-links by ionic species incorporated into the polymeric structure. The commercially available T-lyne filament[8] (shown in figure 1.7) contains Surlyn ionomer and has shown to have a slightly reduced anisotropy when compared to other commercial filaments [37]. There have also been several works that used Surlyn ionomer pellets to create filaments of various blends for FDM [47, 48]. Calderón-Villajos et al. [49] reported on the self-healing characteristic of 3D printed composites of Surlyn and multi-walled carbon nanotubes. Although 3D printing reduced the tensile strength of the polymer, the self-healing ability was not altered by the process.

[8] https://taulman3d.com/t-lyne-spec.html accessed November 11, 2019


**(a)** T-lyne filament.

**(b)** 3D printed T-Lyne.

**Figure 1.7:** Filament and a print made of T-lyne filament, a polymer containing Surlyn Ionomer[8].

### Reducing anisotropy with self-healing polymers

Another approach to address anisotropy in 3D printed parts has been through material design. Recently, the use of materials containing reversible bonds has been explored as an alternative method toward reduced anisotropy in parts. Bonds that can be dissociated by an elevation in temperature and that can reform in between layers of a printed part have shown to enhance the interlayer strength and thereby reduce anisotropy. Davidson et al. [36] demonstrated this concept by printing with a blend of commercially available polylactic acid (PLA) and different concentrations of a novel synthetic polymer containing furan-maleimide (fmDA) adducts as a mending agent which forms reversible cross-links through the (retro) Diels-Alder (DA) reaction. The DA reaction proved particularly suitable, since the breaking of these bonds occurred at 120 °C, while the reformation of the bonds upon cooling occurred at 40 °C. This implied that the polymer can form these bonds for some time after deposition and between molecules in different layers of the print. Tensile tests of prints with different, unidirectional printing directions were performed and a decrease in anisotropy was observed, which the authors attributed to the formation of the Diels-Alder bonds in-between the layers of the print. The blends also showed an increased diffusion of the layers compared to regular PLA, as can be seen in figure 1.8.

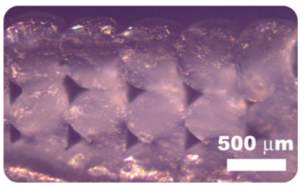


**(a)** PLA.

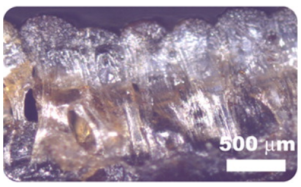


**(b)** PLA + fmDA.

**Figure 1.8:** Microscopic images of the cross sections of 3D printed PLA and PLA+fmDA [36].

The work of Davidson et al. was continued by Appuhamillage et al. [26], who investigated PLA blend with 25 wt% 'mending agent' at different cross-linking densities within the ureidopyrimidinone methacrylate (UPyMA) motifs. Through tensile tests, they established that an increase in cross-link density accompanied a decrease in anisotropy by measuring the toughness as well as tensile strength. The healing performance of the prints was also tested, by taking the fractured surfaces of a print that was broken after a tensile test, heating them

to 120 °C and pushing them together. Repeated tensile tests showed a recovery of 77% of the original tensile strength of the fully cross-linked blend.

Yang et al. [37] presented a series of Diels-Alder reversible thermoset (DART) polymers. Tensile tests in different printing directions also showed a reduction in anisotropy. The properties were compared to various commercial thermoplastic polyurethanes (NinjaFlex, SemiFlex and Cheetah), and T-Lyne, a polyethylene copolymer that contains Surlyn ionomer. The anisotropy of the DART polymers was significantly lower than that of the polyurethanes, and slightly lower than that of T-Lyne. However, the polymers were not rigid enough to maintain structural integrity to print arbitrary geometries.

These works have established the possibility of reduction of anisotropy in 3D printed parts through the incorporation of reversible cross-links. They have also demonstrated that the self-healing properties enabled by these reversible cross-links can still facilitate self-healing behaviour after printing.

## 1.4 Mechanical testing of 3D printed parts

When the AM of novel polymers, and specifically polymers with the ability to heal mechanical properties is performed, the mechanical characterisation of these prints needs to also be addressed. The processing by AM might affect the mechanical properties as well as the self-healing ability. When a 3D printed part is tested, the response is a result of not only the material used, but also the geometry that results from the processing method. Significant improvements in the mechanical integrity of 3D printed parts has been achieved through tailoring of the printing parameters [13, 16, 17, 15]. This complicates the mechanical comparison of 3D printed parts using different materials.

There is a range of mechanical testing methods available that address various mechanical properties of 3D printed parts [50]. In this section, some of these methods will be shown and elaborated on, namely tensile testing and fracture toughness testing.

### 1.4.1 Tensile testing

The most common method to assess the mechanical performance and anisotropy of 3D printed parts has thus far been by tensile testing [36, 26, 37]. Tensile samples were cut out of a print in several directions. The printing directions yielding the most extreme results are shown in figure 1.9. The printing direction displayed in figure 1.9a typically shows the highest tensile strength, since the loading of the sample aligns the direction of the printed strands. In this case the strength is dictated by the mechanical strength of the bulk polymer or even larger due to the alignment seen in some polymers [51]. The printing direction shown in figure 1.9b is expected to show the lowest tensile strength, since in this case it depends on the interlayer adhesion. Tensile tests using dog-bone specimens have the advantage of being a standardised test method [52] which yields reliable results that may be compared to other work using the same method.

**(a)** Tensile sample with printing direction aligned with the direction of the tension. This direction is typically the strongest (highest failure stress/toughness) of the print since the tension pulls on the aligned fibres, in which the polymer may also have aligned itself during deposition.

**(b)** Tensile sample with the printing direction aligned perpendicular to the tension. This direction is typically the weakest (lowest failure stress/toughness) of the print, since the results rely on the interlayer diffusion.

**Figure 1.9:** Schematics of tensile samples using printing patterns that yield the most extreme results.

Tensile samples could easily be cut from (3D printed) sheets of a polymer. However, in order to comply with ASTM standards, the samples needed to have a minimum length of 63.5 mm and five samples for each direction would need to be tested. When testing elastomers, the clamping of the samples could also reduce the quality of the results due to a different transfer of the forces through the sample. Alternatively, the ASTM standard test methods for vulcanised rubber and thermoplastic elastomers - tension [53] could be used.

### 1.4.2 Double cantilever beam for mode I failure

Fracture mechanics provide a more specific way to study the interlayer properties of 3D printed parts. The double cantilever beam (DCB) test is standardised for the characterisation of interlayer properties of fibre-reinforced polymer-matrix composites [54], but it has also been applied to 3D printed parts [55, 56]. DCB samples are typically rectangular bars where a crack is introduced by placing a teflon insert in-between the two middle layers of part of the bar, shown in figure 1.10. The crack is then opened in tension to induce a mode I fracture. In a mode I fracture, the crack propagates due to a tensile stress normal to the plane of the crack. The primary output of the test is the mode I interlaminar fracture toughness.

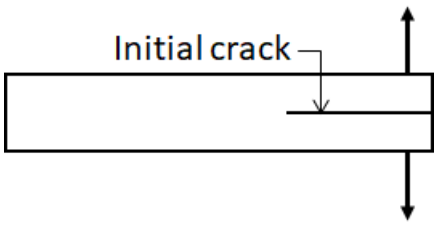


**Figure 1.10:** Schematic of a possible DCB configuration to test the mode I interlaminar fracture toughness.

Spoerk et al. [55] applied the DCB test to characterise 3D printed PLA samples with mixed results. They found that the test had limited applicability. The geometry of some samples did not allow the preparation of the samples. Other samples had a delamination energy below the detection limit of the measurement equipment, and some samples failed within the load-line, instead of a mode I failure between the layers. A trend was seen towards an increasing delamination energy and an increase in printing temperature, as well as with a decrease in layer height. Aliheidari et al. [56] successfully used the DCB test for 3D printed acrylonitrile

butadiene styrene (ABS) at three different temperatures. They also found that the inter laminar fracture toughness did increase when the printing temperature was increased.

### 1.4.3 Trouser tear testing for mode III failure

Davis et al. [57] presented a testing method to measure the mechanical strength of the welding zone produced during 3D printing called the trouser tear test. The test was an adaptation of ASTM D1938-14 for the tear propagation resistance of films and thin sheets [58]. Walls consisting of a single strand were printed, a pre-crack was created by pausing the print halfway through and inserting a polytetrafluoroethylene tape. The two halves were then pulled away from one another to induce a mode III failure and open the crack, as shown in figure 1.11. In mode III failure, the stress acts parallel to the plane of the crack and parallel to the crack front. They used the test to capture the effect of printing temperature and printing speed on the tearing energy of acrylonitrile butadiene styrene (ABS). The tearing energy depended on the printing temperature, but not on the printing speed.

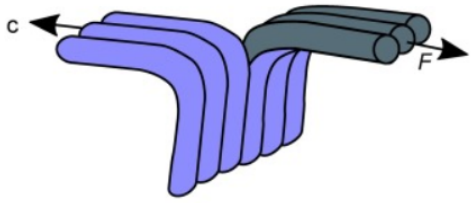


**Figure 1.11:** Schematic of the trouser tear test [57].

## 1.5 Self-healing polyurethanes as a potential 3D printing material

Polyurethanes are a broad and versatile family of polymers. Polyurethanes can have many different forms, such as foams, fibres or elastomers, and can be applied in a variety of high-end and low-end applications. What these polymers have in common is the presence of urethane groups, which, in most cases, result from a poly-addition reaction between an isocyanate group and a hydroxyl group as seen in figure 1.12. A notable property of the urethane bond is its ability to form hydrogen bonds through the N-H group.

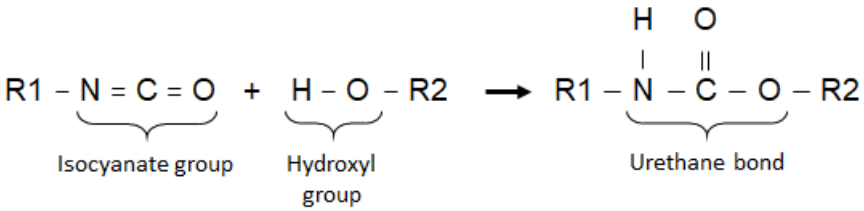


**Figure 1.12:** Chemical reaction that creates a urethane bond from a isocyanate group and a hydroxyl group.

Thermoplastic polyurethanes (TPU's) are a sub-class of polyurethanes that often use three primary components. There are two molecules that contain a hydroxyl group: a long-chain

diol, and a short-chain diol. These are called the polyol and the chain extender, respectively. The final component is a diisocyanate. The reaction between the diisocyanate and the chain extender occurs at a faster rate than that of the diisocyanate and the polyol, which results in a so-called segmented polymer. One segment called the hard segment consists of alternating diisocyanate-chain extender sequences, which results in a rigid chain with a high amount of urethane bonds. The other segment consists of the polyol and is called the soft segment. The resulting polymer can be considered a copolymer of the hard and the soft segment.

By careful selection of the components of a polyurethane, a thermoplastic elastomer can be synthesised. If the hard segment and the soft segment of the polymer chain are incompatible, a phase separation in the material can occur as the hard segments cluster together into blocks through hydrogen bonding, which is illustrated in figure 1.13. The hard blocks, having a high concentration of hydrogen bonds due to the nature of the urethane bond, are interspersed by the soft blocks. The resulting material is a thermoplastic elastomer, where the hydrogen-bonded hard blocks act as physical cross-links. At elevated temperatures, these cross-links can dissociate allowing the polymer to melt, in contrast with thermoset elastomers. The degree of phase separation depends on components, their molar ratio, reaction conditions and manufacturing process. As a result, TPU's can combine high flexibility with high strength and tunable properties, while maintaining relatively low production costs [59].

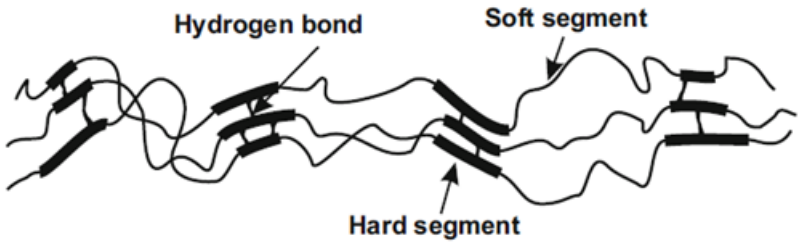


**Figure 1.13:** Phase separation in thermoplastic polyurethanes, with hydrogen bonds between the hard domains [59].

At the time of writing, there were numerous commercially available thermoplastic polyurethane filaments for FDM, such as Real filament TPU 98A [9], Ninjatek's Ninjaflex [10] and Ultimaker TPU 95A [11].

Phase segregation, such as that found in polyurethanes, can also provide a useful basis for self-healing materials [60]. Yang et al [61] demonstrated a self-healing polyurethane chemistry using hexamethylene diisocyanate, 1,4-butanediol as the chain extender and a PCL diol as the polyol. Dibutyltin dilaurate was used as a catalyst. The polymer was drawn into fibres with a 200 $\mu$m diameter. The healing was facilitated by the hydrogen bonds in the hard segments and was assisted by the shape memory behaviour of the material. After 120 minutes of healing at 65 °C, 85% of the failure strength and strain was restored.

[9] http://real-filament.com/datasheets/MSDS/EN/Real%20filament%20TPU%2098A.pdf accessed November 15, 2019
[10] https://ninjatek.com/ninjaflex/ accessed November 15, 2019
[11] https://ultimaker.com/materials/tpu-95a accessed November 15, 2019

From a conceptual point of view, the considerations in the design of self-healing polymers display an overlap with those of material design for additive manufacturing. This overlap is primarily seen in the desired increase in mobility at moderate conditions/temperatures. In the case of self-healing materials, this behaviour facilitates the repair of damage; in the case of additive manufacturing it facilitates the deposition or fusing of the material. This overlap suggest that the properties of self-healing materials in particular might be a good match with FDM. Moreover, some properties inherent to these materials might provide additional benefits to parts produced by AM, such as prolonged lifetime, stress relaxation and the ability to reversibly cross link in between layers.

## 1.6 Establishing a protocol for the FDM with self-healing elastomers

The first step towards printing with CR1 was to gain an understanding of the material in the context of FDM. The lack of information available about AM with self-healing elastomers with high toughness demanded the establishment of a protocol to guide the processing of AM into a filament and then into a print. This protocol would be applied to the polymer in this study and to comparable polymers in the future.

The processing from bulk polymer to printed part was first schematised in figure 1.14. Ideally, the process should be a feedback loop, in which results and observations made during filament making and printing and their results would influence the settings of the filament making. Additionally, these results could be used to make alterations to the polymer in order to tune its properties to ease the manufacturing. This was, however, outside of the scope of the thesis and is therefore represented by dashed lines.

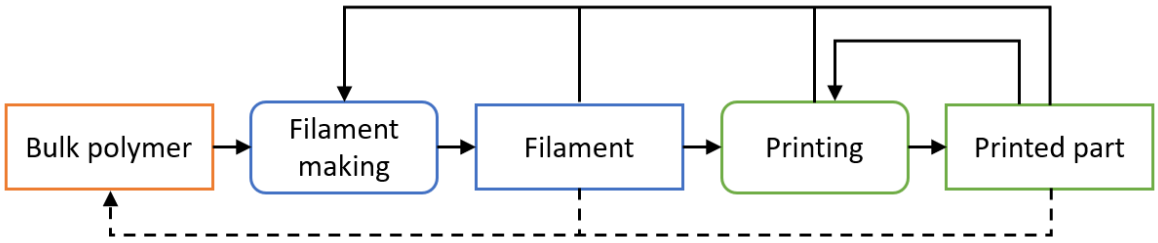


**Figure 1.14:** Suggested approach for AM with novel polymers. The dashed arrows are excluded from the scope of the thesis.

Figure 1.15 shows the elaborated processes for filament making and printing. In order to be more broadly applicable, it was preferable to establish a material characterisation procedure that was independent of the specifics of the filament maker and FDM set-up used.

Figure 1.15a shows the suggested procedure for filament making. The bulk material would be characterised in order to find material properties relevant for filament making, which were translated into a range of settings: the temperature of the print-head during printing ($T_{print}$) and the print-speed $V_{print}$. During the process, the settings were adjusted according to observations. Finally, the filament was characterised again, which, if needed, could be used to improve the process. The filament needed to meet several requirements:

- The filament needed to resemble the bulk polymer in colour and transparency.
- FTIR measurements of the filament should not reveal blending with polymers previously present in the filament maker.
- The filament needed to be free of bubbles.
- There should be no water present in the filament.
- The filament should contain regions of 50 cm in length with a diameter with a standard deviation of at most 0.1 mm.

Once a filament was created that fulfilled the requirements, the methodology for FDM could be started as displayed in figure 1.15b. The first important outcome was the ability to print at all. Combining the knowledge of the bulk polymer and its filament form with knowledge of the limits of the printer set-up, some settings could be suggested. Similarly to the filament making methodology, observations during printing could be used to establish printing settings and the prints were characterised in order to further inform the optimal settings for FDM.

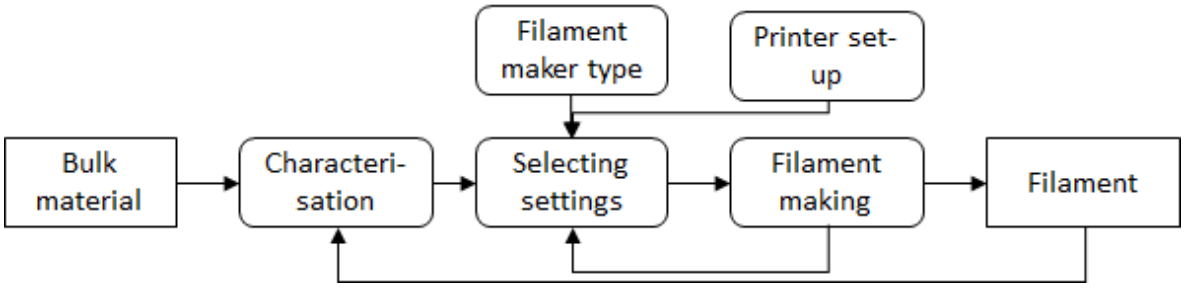


**(a)** Proposed methodology for filament making.

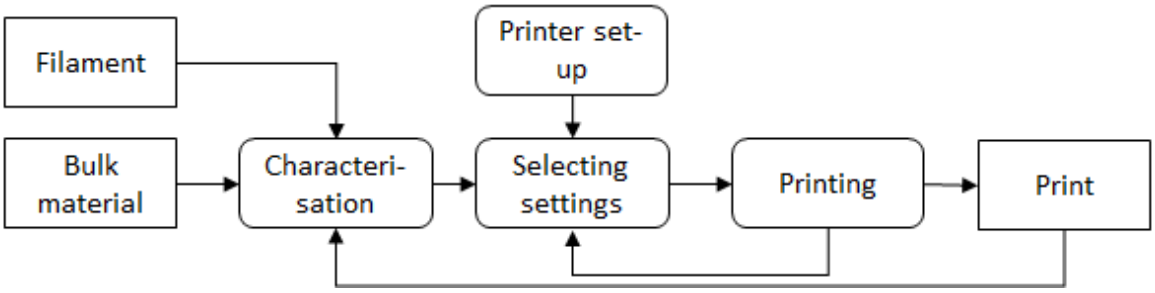


**(b)** Proposed methodology for FDM.

**Figure 1.15:** Incorporating characterisation and set-up into the approach. Material characterisation and observations during processing were used to optimise the processes.

## 1.7 Scope

The scope of the thesis is to lay the groundwork for FDM with self-healing TPU's by printing with CR1. The assessment of CR1 as a 3D printing material was done in two parts. During the first part, the polymer was characterised such that it could be processed into a filament that could then be used in a 3D printer. The second part was the assessment of the 3D printed CR1. The performance 3D printed CR1 was studied by comparing it to bulk CR1 and to a commercial 3D printing TPU filament.

## 1.8 Outline

The main body of the report is divided into 5 chapters. In chapter 2, the materials and experimental set-up are discussed. Chapter 3 discusses the characterisation of the bulk polymer. In chapter 4, the process and results of filament making with CR1 are discussed. Chapter 5 discusses the FDM with CR1 and presents the characterisation of 3D printed CR1. Finally, in chapter 6, conclusions and recommendations based on the research are presented.

# Chapter 2

# Materials and experimental set-up

In this chapter, the starting point of the work executed during this thesis is presented. The procedure followed during the thesis was very much iterative, which is why this chapter presents only the starting point of the work. Section 2.1 shows the polymer components used to synthesise CR1 and discusses its synthesis procedure. Some commonly available details of Ninjaflex, the commercial polymer used as a reference, can be found in section 2.2, as well as the print-settings used. The filament production set-up is described in section 2.3, and the starting set-up of the 3D printer in section 2.4. Section 2.5 describes the material characterisation methods used during the thesis. Finally, section 2.6 discusses the protocol that was used to characterise CR1 for filament making and for 3D printing.

## 2.1 Polymer synthesis

### 2.1.1 Materials

The long diol used to create CR1 named DEV2099 was provided by Croda Nederland B.V. The chain extender was 2-Ethyl-1,3-Hexanediol (EHD), 97%, mixture of isomers, Sigma-Aldrich, and the diisocyanate was 4,4'-Methylenebis(phenyl isocyanate) (MDI), 98%, Sigma-Aldrich. Figure 2.1 displays the chemical structure of each of the components.

### 2.1.2 Synthesis procedure

The molecular weight and molar ratio of the polyurethane components are displayed in table 2.1. There was a slight excess of isocyanate groups when compared to diol groups (1.1:1). On the one hand, this ensured that the polymer chains were always terminated with isocyanate groups and enabled the synthesis of a high-molecular weight polyurethane [62]. However, this could also lead to undesirable reactions. Allophanates can form as a reaction between isocyanate groups and urethane bonds and result in a permanent cross-link between two chains.

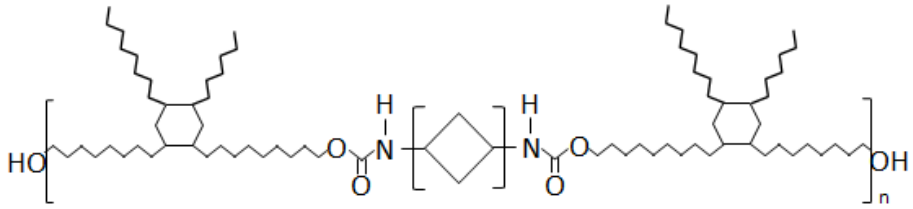


**(a)** The polyol: DEV2099.

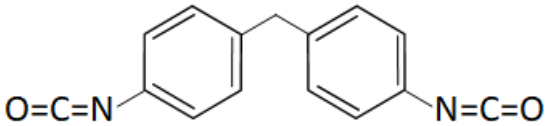


**(b)** The diisocyanate: MDI.

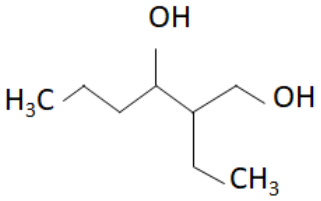


**(c)** The chain extender: EHD.

**Figure 2.1:** Raw materials used for the synthesis of CR1.

Since the polymer was required to be melt-processable, the formation of allophanates was undesirable. Allophanates tend to form at elevated temperatures (above 170 °C) and therefore it was important to reduce the mixing speed in order to limit friction and thereby temperature increase during mixing [63]. Since the reaction between MDI and EHD was favourable to the reaction between MDI and priplast, the hard segment concentration was expected to be equal to the mass ratio between priplast and EHD, which came down to 26%.

**Table 2.1:** Molar mass and molar ratio of the polyurethane components.

| | **Molar mass, g/mol** | **Molar ratio** |
|---|---|---|
| DEV2099 | 2000 | 1 |
| EHD | 118.17 | 0.6 |
| MDI | 250.25 | 1.7 |

Due to the high viscosity of DEV2099 at room temperature, the first step of the process was to place it into an oven at 75 °C for 2 hours to reduce its viscosity and remove entrapped air. Then, 90 grams of DEV2099 was transferred into a polypropylene cup and placed back into the oven at 60 °C. The weight of the other components was calculated base don the weight of DEV2099. The bottle containing MDI was removed from the freezer and left at room temperature for 40 minutes in order to limit the condensation of water onto the diisocyanate. When the priplast had been in the oven for 40 minutes, the MDI was weighed into a glass jar, adding 1 gram to compensate for residue after pouring. At this same time, the Priplast was removed from the oven and EHD was weighed and added to the cup. The diol mixture and the MDI were placed in an oven separately at 55 °C for roughly 45 minutes, or until the MDI had just fully liquefied. Both containers were removed from the oven and the MDI was added to the diol mixture on a scale. The cup was mixed using a SpeedMixer$^{TM}$ DAC 400.2 VAC-P, degassed to 40 mbar for 2 minutes and then mixed at 1800 rpm for 45 seconds. Once removed from the speed mixer, the mixture was poured into a petri-dish lined with nylon foil and placed into an oven at 65 deg for 18 hours.

### 2.1.3 Synthesis results

The results of the synthesis were transparent plaques, an example of which can be seen in figure 2.2. A total of 9 batches of CR1 were synthesised (named CR1_1 through CR1_9), each with a thickness of about 5 mm and weighing roughly 80 grams. After vacuum mixing as the mixture was poured out into a mould, the viscosity of the polymer increased rapidly, resulting in a significant amount of residue in the cups. Initial investigation of the residue in the cups revealed un-reacted groups, and the residue in the cup was therefore discarded.

The plaques that were synthesised had a high thickness and an irregular surface due to the film used in the moulds. Therefore, an additional plaque of the polymer was poured into a mould to form a sheet with a thickness of 3.5 mm: CR1_0. This plaque was used for measurements requiring a constant thickness, such as rheology and DMTA.

The plaques showed typical elastomeric properties, i.e. quick recovery of large deformations. In spite of the vacuum applied during mixing, the plaques showed considerable amounts of air bubbles, although the goal was not to create a bubble-free polymer, since it would be cut up into smaller pieces and reprocessed in any case. The bubbles in each of the plaques were not too abundant and their size exceeded several millimetres.

**Figure 2.2:** Plaque of the as-synthesised CR1.

## 2.2 Ninjaflex samples

Ninjaflex filament with a diameter of 1.75 mm was purchased from 123-3d. Thermal properties of Ninjaflex (provided by the manufacturer) are shown in table 2.2, as well as the printer settings recommended by the manufacturer [1].

While printing the Ninjaflex samples, the print settings in appendix B were used. For rheology samples, a printing temperature of 225 °C, print speed of 20 mm/s and a print-bed temperature of 55 °C were used. For the samples used during mechanical testing, the print-speed was always 20 mm/s and the print-bed temperature was 30 °C, while the print-head temperature and the infill distance were varied.

[1] https://ninjatek.com/ninjaflex/

**Table 2.2:** Properties and recommended printer settings of Ninjaflex [1].

| Property | Value |
|---|---|
| Glass transition temperature | -35 °C |
| Melting temperature | 216 °C |
| Recommended nozzle temperature | 225 - 235 °C |
| Recommended print-bed temperature | 25 - 40 °C |
| Recommended printing speed | 15 - 35 mm/s |

## 2.3 Filament production set-up

The filament was prepared using a 3DEVO Next 1.0 - ADVANCED filament maker, shown in figure 2.3 [2]. The machine came equipped with a single nitride extruder screw and 4 heating zones that could be set individually up to 450 °C ($T_1$ to $T_4$, where $T_1$ was closest to the exit of the extruder). Two fans with adjustable fan speed and orientations cooled the filament as right at the exit of the extruder section. The diameter of the filament was controlled by drawing on the material using a puller system, the speed of which was adjusted based on measurements by an optical sensor. Finally, the filament was collected onto a spool.


**(a)** The filament maker [2]. **(b)** The filament drawing and winding section.

**Figure 2.3:** 3DEVO next 1.0 - ADVANCED filament maker.

[2] https://www.3devo.com/wp-content/uploads/2016/09/3Devo-Flyer.pdf

## 2.4 Fused deposition modelling: initial set-up

The 3D printer used was the Ultimaker 2+, seen in figure 2.4a. The Ultimaker 2+ normally prints 2.85 mm filament and uses a so-called bowden system. In this system, the feeder wheels are located at the back of the printer and they feed the filament into the printehead through a tube. Various components of the Ultimaker 2+ may be customised, but the customisation most relevant to this thesis was the replacement of the printhead and feeding system. In order to be able to print with flexible filament, the print-head of the Ultimaker 2+ was changed for a direct-drive system: the E3D titan aero seen in figure 2.4b. This way, the distance between the feeder wheels and the print-head was much smaller, reducing the change of the filament to buckle.

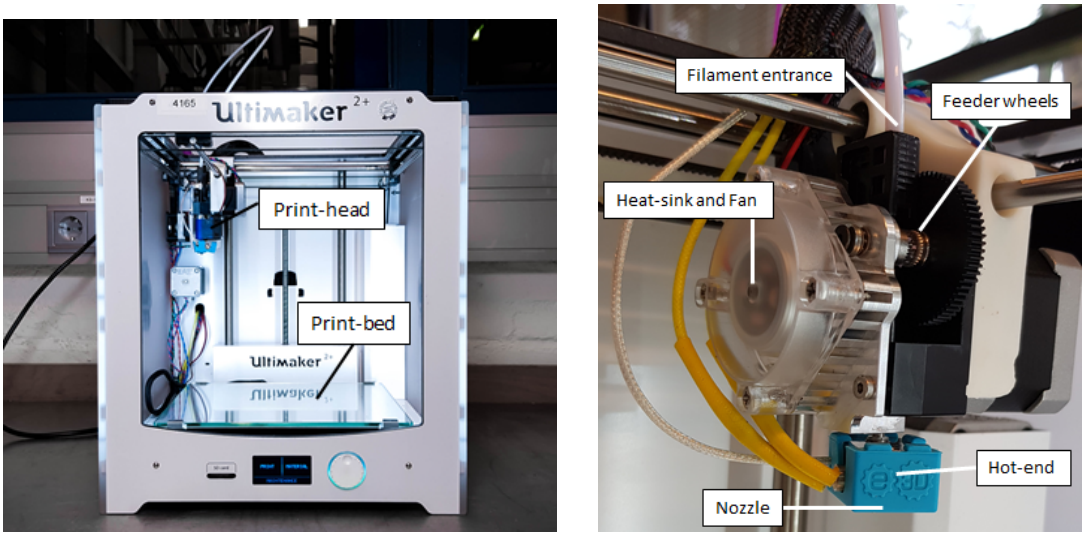


**(a)** The Ultimaker 2+. **(b)** The E3D titan aero print-head.

**Figure 2.4:** Initial 3D printing set-up.

## 2.5 Characterisation techniques

In section 1.2, some measurable polymer parameters useful for filament making and FDM were identified. Based on these parameters, characterisation methods were selected.

### 2.5.1 Fourier transform infrared spectroscopy

Fourier transform infrared spectroscopy (FTIR) is a quick, non-destructive test that can be used to study the chemical composition of a polymer. The resulting spectrum displays the energies that are involved in certain types of asymmetrical vibrations of chemical bonds. A PerkinElmer Spectrum 100 FT-IR spectrometer was used to conduct FTIR measurements of in representative areas of each batch, CR1 synthesised at Croda, the filament and the prints. Spectra were conducted from 4000 $cm^{-}1$ to 500 $cm^{-1}$ using the average of 8 scans.

*Note: within this thesis, FTIR was used primarily to get a quick impression of any chemical changes in the polymer. Therefore, the results are not included in the main body of the report, but can instead be found in appendix A.*

### 2.5.2 Thermogravimetric analysis

Thermogravimetric analysis (TGA) was used to study the degradation behaviour of the polymer. The degradation temperature ($T_d$) of a polymer puts a hard limit on the temperature at which it can be processed. There are two main curves that can be drawn using data from thermogravimetric analysis. $T_d$ can be determined as the temperature at which a certain percentage of the weight is lost. Alternatively, the infliction point can be found by plotting the derivative of the weight-temperature curve. Performing TGA on the filament had the purpose of revealing any water that could have been incorporated into the filament could be seen in a TGA analysis as a mass drop at 100 °C. TGA measurements were conducted using a PerkinElmer TGA 4000 under nitrogen atmosphere. The TGA was run from 30 °C to 600 °C at 5 °C per minute.

### 2.5.3 Differential scanning calorimetry

Thermal transitions of the polymer were studied using differential scanning calorimetry (DSC). During DSC measurement, the amount of energy required to increase the temperature of a sample is measured. Thermal transitions are reflected in a change in this heat flow. This method can be used to identify the glass transition temperature ($T_g$), the melting temperature ($T_m$) and the recrystallisation temperature of the polymer. Additionally, since thermal processing can introduce residual stresses into the material, DSC can be used to reveal their presence and study the temperature at which they are relieved.

DSC measurements were conducted with a DSC 250 by TA instruments, using an empty pan as a reference. There were different programmes for the bulk and the filament.

- For the bulk: first, the sample was cooled down to -30 °C and kept there for 5 minutes. Then, the temperature was increased to 150 °C at 5 °C per minute, after which it stayed at 150 °C for 5 minutes. Next, the sample was cooled back down to -30 °C at 5 °C per minute, to stay at -30 °C for 5 minutes. It was then heated up again to 250 °C at 5 °C per minute, stayed there for 5 minutes and then cooled back to 25 °C at 5 °C per minute.
- For the filament: the DSC was used to study the thermal stresses in the polymer. Therefore, there was no initial heating and cooling cycle. Instead, the sample was cooled down to -30 °C and stabilised at -30 °C for 5 minutes. Then it was heated to 250 °C at 5 °C per minute.

### 2.5.4 Attenuated total reflection FTIR

Attenuated total reflection (ATR) imaging is a type of FTIR. An FTIR microscope in ATR imaging mode collects the IR-spectra throughout a sample in 'pixels' that can be combined

to form a 2D space. By comparing the spectra throughout this space, a structure can be distinguished. This technique was useful to document the chemical changes in a material throughout an area of the surface of a sample in more detail. Previous work had suggested that the chosen polyurethanes exhibit domains with a size of several tens of micrometres that could be distinguished by ATR imaging. Beside the molar composition and the synthesis procedure, the thermal history of the polymer also significantly contributes to the degree of phase separation [64]. Within this work, ATR imaging was used to study the phase separation of CR1 and its changes as a result of processing. A Perkin Elmer Spotlight 200i FTIR microscope system was used in ATR mode. The area covered was 500 $\mu$m by 500 $\mu$m in size, with a pixel size of 1.65 $\mu$m. For each pixel, a total of 2 scans were conducted with the wavenumber range set to 4000 to 750 $cm^{-1}$. ImageSpectra software was used to distinguish different structures within the scans.

### 2.5.5 Rheology

Rheology was used to study the thermomechanical properties of the polymer under shear. Similar to DMTA an oscillatory load is applied, but in this case the load is a shear load. The following measurements were performed:

- An amplitude sweep where the amplitude of the deformation was increased at constant frequency and at room temperature. From this measurement, a point in the linear-viscoelastic region was established that could be used to perform the next experiments.
- A temperature sweep, in which the viscoelastic response over a range of temperatures was recorded. The temperature at which the viscous modulus ($G''$) crosses the elastic modulus ($G'$) marks the temperature at which (for these conditions) the polymer starts behaving more like a liquid than like a solid. Alternatively, the complex viscosity can be plotted to show its change with temperature.
- Shear rate analyses at various temperatures. These analyses can be used to find the power-law constants of the polymer at different temperatures. The temperature where $G''$ crosses $G'$ can be used as a starting point. Shear rate analyses can be used to study the response of the viscosity $\eta$ and the shear stress $\tau$ to an increasing shear rate $\dot{\gamma}$. The results include the power law constants that can be used to determine the shear rate during FDM. Additionally, the $\dot{\gamma} - \eta$ curve can be compared to that of a similar polymer that is commercially available for FDM. Ideally, the viscosity of the polymer shows a steep drop at a shear rate above the one experienced during FDM. This means that the polymer is easily malleable under stress, but can retain its shape once it leaves the nozzle, when the stress is no longer applied. These measurements account for temperature as well as speed and and can therefore be used to say something about printing temperature as well as speed. Su et al. [5] used amplitude sweep rheology on top of changing the shear-rate to determine printing settings. The point where $G'$ and $G$" cross and the viscous modulus becomes larger marked the shear stress at which the polymer starts behaving 'liquid-like'. The LDM printing set-up allowed for precise control of the stress and shear rate exerted on the polymers composites.

A Haake Mars III (ThermoScientific) rheometer was used with flat plates with a diameter of 8 mm. Three types of measurements were conducted.

- An amplitude sweep from 10 $Nm^{-}2$ to 1000 $Nm^{-}2$ at a frequency of 1 Hz.
- A temperature sweep from 30 °C to 250°C back to 30 °C at 1 °C per minute. The shear strain was constant at 0.001.
- Shear rate analysis with different temperatures: at 200 °C, 210 °C and from 220 °C to 240 °C with 5 °C increments. The shear rate was varied from $1{\cdot}10^{-3}$ to $1{\cdot}10^{3}$ logarithmically.

Shear rate analyses were also performed for Ninjaflex. The recommended printing temperature of Ninjaflex was 225 °C to 235 °C. While printing, it was observed that Ninjaflex could also be printed at 205 °C. Therefore, shear rate analysis were performed at temperatures ranging from 205 °C to 235 °C at 5 °C increments. Prior to the measurements, the samples were heated to the desired temperature and kept there for 10 minutes under Nitrogen atmosphere.

### 2.5.6 Dynamic mechanical thermal analysis

Therefore, dynamic mechanical thermal analysis (DMTA) was a useful tool to study the viscoelastic behaviour of the polymer under compression/tension. During DMTA measurements an oscillating force is applied and the sample response is collected. In viscoelastic polymers, the response can be divided into an elastic response and a viscous response.

DMTA measurements were performed using a TA-RSA G2 Solids Analyser using rectangular samples cut from a sheet of CR1 measuring 10 mm in width and 2.6 mm in thickness. The linear viscoelastic regime had already been determined from the rheology measurements. Based on these, a constant strain of 0.1%, an oscillation strain of 0.1% and a frequency of 1 Hz were applied. A heat ramp from -10 °C to 150 °C back to -10 °C was conducted.

### 2.5.7 Thermomechanical analysis

Thermomechanical analysis (TMA) studies the change in size of a sample throughout a range of temperatures under a small pre-load. This way, the change in shape of the filament as it heats up could be studied and compared to that of unprocessed CR1.

A Perkin Elmer TMA 4000 was used with an expansion probe. Samples were put between an aluminium pan and a lid. The bulk was assumed to have an isotropic response and was only measured in 1 direction. The filament was measured in the axial direction and in the lateral direction. A relatively thick piece of filament was used, with a diameter of 3.32 mm, in order to improve the accuracy of the measurements. Additionally, the expansion of the cup and the lid was also measured and subtracted from the results. The procedure that was used was always the same. A force of 2 grams was applied to the sample in the holder. The sample was stabilised at 20 °C for 10 minutes, and then it was heated to 120 °C with a heating rate of 5 °C per minute. The final temperature of 120 °C was chosen such that the sample would not be compressed due to the force of 2 grams that was applied throughout the experiments.

### 2.5.8 Optical microscopy

Microscopic pictures were taken using a Keyence VHX-2000.

### 2.5.9 The compression cut test

In order to study the mechanical properties of small quantities of elastomer, a compression cut test was employed. A compression cutting test for rubbers was described by Holt in 1934 [65]. In this test set-up, the sample was compressed between a flat plate and a cutting tool. Although Holt concluded that the test could not be considered a replacement for tensile tests (or a replacement for any common test for elastomers for that matter), the data still provided a measure for the resistance against cutting or shearing, typically quantified as the cutting force, defined as the force at which the blade starts to cut through the sample.

Figure 2.5 shows a schematic drawing of a sample used for this test. The sample was printed with the layers stacking in the Z-direction. The printing pattern of each layer would be identical.

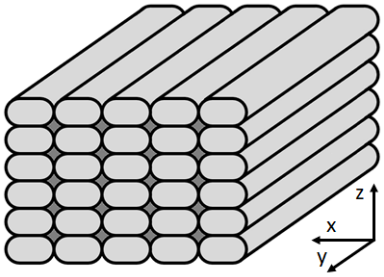


**Figure 2.5:** Schematic of a 3D printed part with a constant raster orientation of [90°].

The sample in figure 2.5 can be tested in three directions. In order to save resources, only the two most extreme cases were tested: the XZ-plane and the YZ-plane, shown in figure 2.6. The results from the prints could be compared to one another, to those of the bulk and those of a commercial 3D printing filament. Since the method had not been employed in this way before, trials were conducted using Ninjaflex, the results of which can be seen in appendix D.

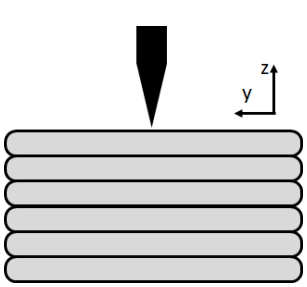


**(a)** Schematic of a cut test where the sample is cut in the XZ-plane.

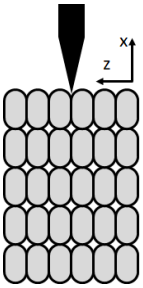


**(b)** Schematic of a cut test where the sample is cut in the YZ-plane.

**Figure 2.6:** Schematics of cut tests where a print is cut in the directions that are expected to yield the most extreme results.

The mechanical testing was performed in an Instron Model 3365 universal testing system with a 1kN load cell. Prints measuring 1 cm by 2 cm and 4 mm in height were cut into cubes measuring 4 mm. The test set-up used can be seen in figure 2.7a. In order to prevent samples from moving during the test, they were attached to the bottom platform with double-sided tape. A regular blade was used, the profile of which can be seen in figure 2.7b. The angle of the tip was 18°, the length of the tip was 0.75 mm and the width of the blade was 0.20 mm. The sample was compressed between the support structure and the razor at a constant speed of 10 mm/s down to 3.8 mm compression at an ambient temperature of 20 °C. The test was captured using a Celestron handheld digital microscope.

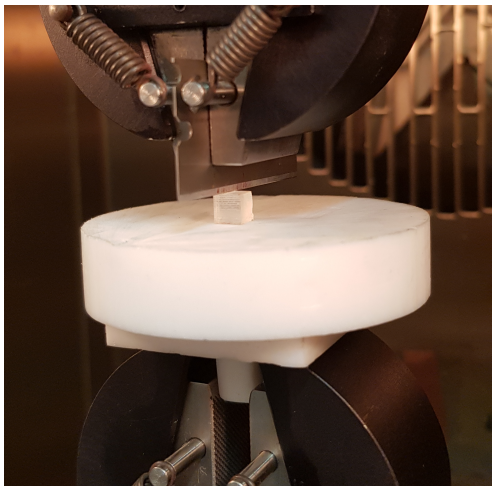

**(a)** Set-up of the compression cut test.


**(b)** Geometry of the blade tip.

**Figure 2.7:** Pictures of the experimental set-up of the compression cut test.

Each set of samples contained 4 samples: two to be tested in the direction parallel to the printing direction, shown in figure 2.6a (direction XZ), and two to be tested in the direction of layer stacking during printing, shown in figure 2.6b (direction YZ). In the case of samples that were also healed, the samples were placed in an oven at 40 °C for 24 hours, based on previous work [66]. After healing, the samples were left to cool down for 1 hour prior to the second test.

## 2.6 Overview: final protocol

The final testing protocol that was used in the thesis is shown in figure 2.8. The protocol aimed to also be applicable to other TPU's. Some experiments relied on the outputs of other experiments. Therefore, they were required to be performed in a certain order. Additionally, while not illustrated in the schematic, FTIR should always be the first measurement. If the synthesis was not successful, performing other experiments with this material will not yield useful results. Characterisation experiments were conducted on the filament for quality assessment but also to predict printing processes. Finally, the prints themselves also required characterisation.

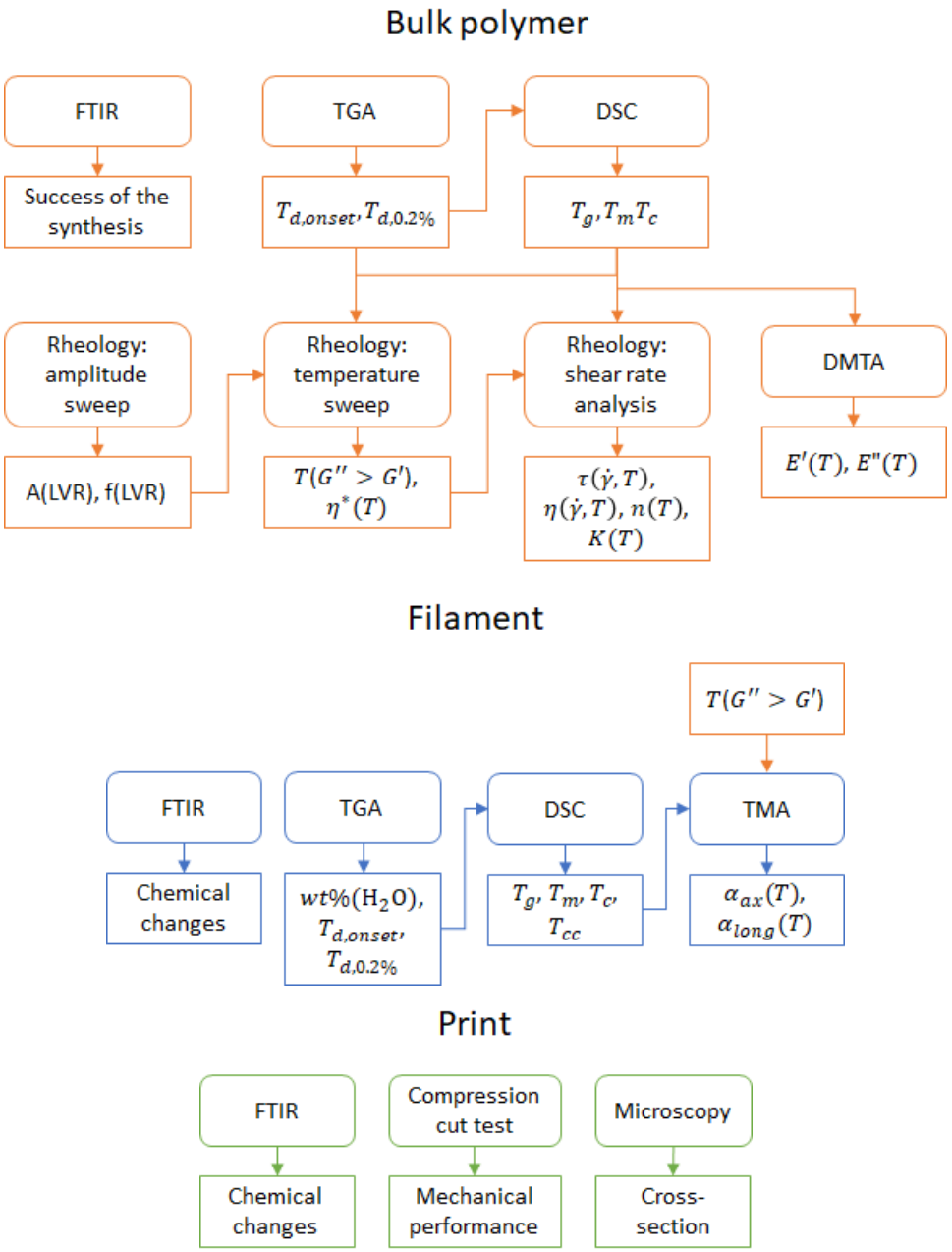


**Figure 2.8:** Summary of the characterisation experiments that were conducted on the bulk, filament, and prints, including the results from bulk and filament characterisation that were used as inputs for these experiments

# Chapter 3

# Bulk polymer characterisation

This chapter presents and discusses the results of the first step in the thesis: the characterisation of the bulk material. Section 3.1 shows and discusses all the results of the characterisation techniques applied to the bulk CR1 section 3.2 presents some conclusions and recommendations made based on the results of the synthesis of CR1 and its characterisation.

## 3.1 Characterisation results

### 3.1.1 TGA

The results from the TGA analysis can be seen in figure 3.1. From the weight loss curve, a thermal degradation temperature $T_d$ of 290 °C was deduced. When investigating the derivative of the weight loss, the derivative increased at 250°. In order to make any definitive conclusions based on these results, they should be combined with knowledge from literature about the degradation behaviour of the polymer.

While the exact degradation reactions of polyurethanes are highly dependent on their components, research on the topic has lead to some generic conclusions about the degradation of polyurethanes [67]. Typical degradation behaviour of polyurethanes can be divided into two stages. The first stage involves the thermolysis of the urethane bonds. This has been associated with the production of carbon dioxide [68, 69]. The second stage is the degradation of the polyol. A higher urethane group concentration is generally associated with a lower thermal stability in polyurethanes [70]. The high immiscibility of the polyol and the hard segment, which should result in relatively large hydrogen bonded hard blocks where the urethane bond concentration is high. Additionally, as seen in figure 2.1a, the polyol also contains urethane bonds. Finally, the effect of mechanical stresses that are applied during processing should not be ignored. Shear stresses in particular can accelerate the degradation of polymers by scission of polymer chains yielding free radicals [71].

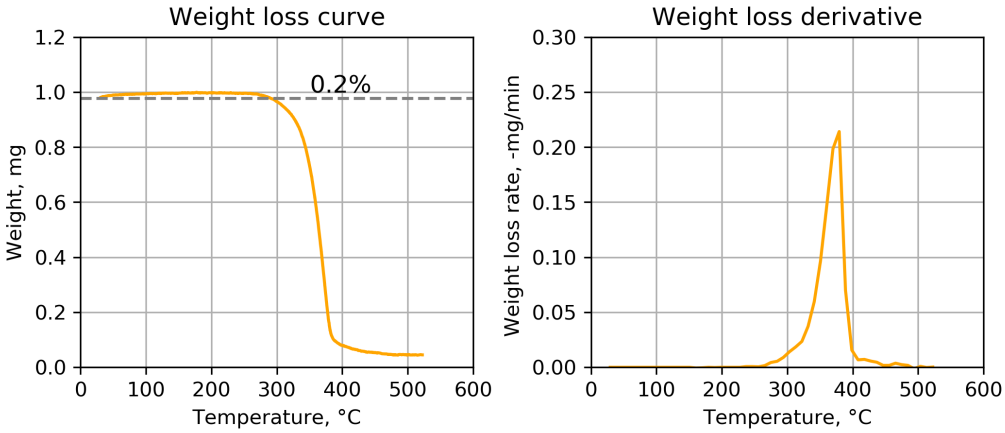


**Figure 3.1:** Results from the TGA analysis of bulk CR1.

This meant that even at lower temperatures where the weight loss was not yet significant, there may be considerable degradation of the urethane bonds in the polymer and consequently of its properties. Therefore, while 290 °C would typically be the considered as the degradation temperature of the polymer, the onset of te degradation could be marked already at 250 °C or even lower when shear stresses are applied.

### 3.1.2 DSC

Figure 3.2 shows the results of the second heating of the DSC experiment. Taking the midpoint at half height of the drop of the heating curve, a glass transition temperature ($T_g$) of 5.5 °C was found. Additionally, a small endothermic event in the heating curve was observed at roughly 205 °C of the heating curve, which was not reflected in the cooling curve. The scale of the event was small, which could mean that it was an artefact. However, the event was reproducible across measurements and even in a different DSC machine. In other works where similar peaks have been observed, they were attributed to the dissociation of hydrogen bonds [59].

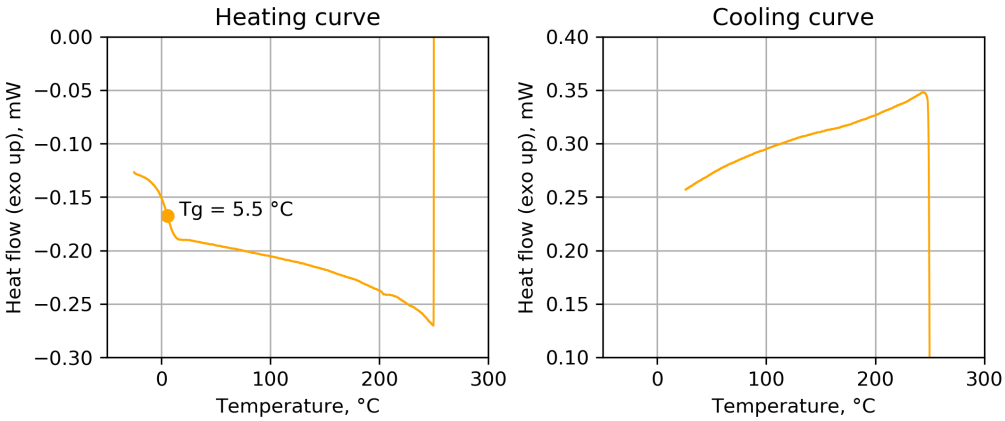


**Figure 3.2:** Results from the DSC analysis of bulk CR1.

### 3.1.3 ATR-imaging

Figure 3.3 displays the ATR image of the bulk CR1. Based on the absorption spectra, the structure could be divided into a matrix and domains. The shape of the domains varied, and their size varied from several $\mu$m to nearly 100 $\mu$m in length. The exact shape of the domains could not be fully derived from the map presented in figure 3.3, given that ATR is a two-dimensional technique. The image was quantified in a 350 $\mu$m by 350 $\mu$m window in the centre. The domains covered a total of 10.04% of the area. The average size of the domains was 592 $\mu$m, and there were a total of 20 domains in the area.

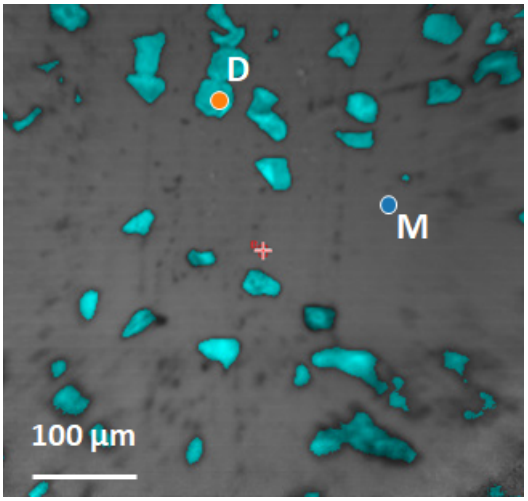


**Figure 3.3:** ATR image of CR1 bulk, distinguishing the structure of FTIR spectra throughout the scan. A point in the matrix is marked by **M**, and a point in the domains is marked by **D**.

In order to study the composition of these two domains, the absorbance spectra of two representative points in the ATR-image were compared. These points are marked in figure 3.3 as point **D** (marking the domains) and point **M** (marking the matrix). Figure 3.4 shows the normalised absorbance spectra of the matrix and the domains. Clearly, several peaks within the spectra differed significantly between the matrix and the domains. The absence of a peak at 2250 $cm^{-1}$ confirmed that there were no isocyanate groups present, and therefore that all the MDI had reacted [72]. Some peaks that are key to the synthesis of polyurethanes are elaborated below.

- **3325 $cm^{-1}$**: associated with the stretching vibration of hydrogen bonded N-H groups or the amide II band, which shifts to a higher frequency when these hydrogen bonds are broken [73].
- **2925 $cm^{-1}$**: the stretching of the C-H bonds in aliphatic compounds [74].
- **1700 $cm^{-1}$**: the amide I band. The largest contribution to this peak is from the stretching vibrations of C=O, and its relatively low frequency suggests hydrogen bonding [73].

Since the polyol that composed the soft segment contained long aliphatic sections, the matrix was associated with a higher concentration of the polyol (or the soft segment) of the polyurethane. The amide I peak at 1700-1640 $cm^{-1}$ can be associated with the C=O stretching vibration. This vibration is also sensitive to hydrogen bonding, shifting to a lower frequency once hydrogen bonding is introduced [73]. This can be seen in the spectra of the domains, indicating that the concentration of hydrogen bonding of C=O bonds is higher in these domains. The other group involved in hydrogen bonding is the N-H group, which also shifted to a lower wavenumber. Based on this, it was suggested that the domains contained a higher concentration of the hydrogen bonded hard segment.

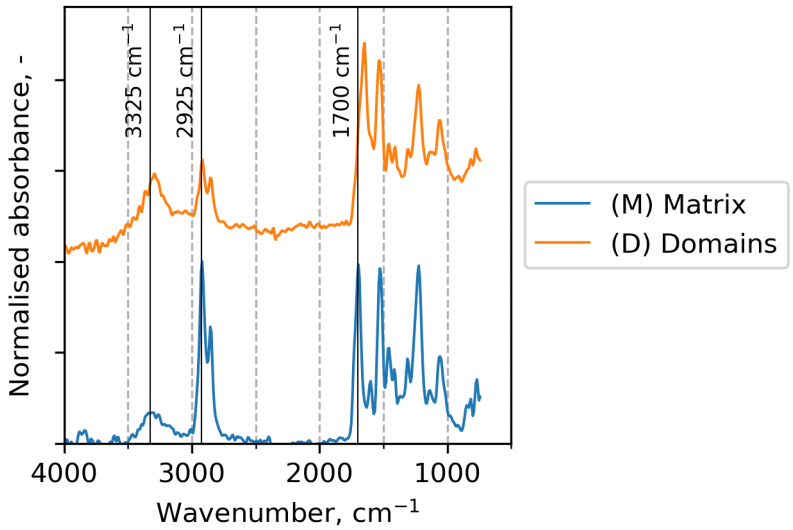


**Figure 3.4:** Spectra of the matrix and the domains of bulk CR1, as marked in figure 3.3.

### The origin of the structure of CR1

While studying the composition of the regions distinguished in ATR imaging could be used to suggest their composition, their size could not be ignored. The size of the domains was larger than what one would expect to see in segmented TPU's. Hard phases of typical thermoplastic polyurethanes have been reported up to several tens of nanometres [75, 76], while the phase separation seen in figure 3.3 shows domains with lengths as large as several tens of micrometres. First of all, it should be noted that a division between the domains seen in figure 3.3 cannot be separated strictly into hard domains and soft domains. Rather, one could say that the absorbance spectrum of the matrix indicated the presence of a higher concentration of the soft segment, while the absorbance spectrum of the domains indicated the presence of a higher concentration of the hard segment of the polyurethane.

In any case, the presence of these relatively large domains indicates the clustering of hard segments of CR1. This behaviour has been attributed to segmented polymers with sufficient thermodynamic incompatibility. Similar behaviour has been reported by Chen et al. [77] when studying the formation of domains detectable by optical microscopy during the co polymerisation of a model polyurethane system. A model was suggested for the formation of

these domains for polymers with various concentrations of the hard segment, illustrated in figure 3.5a. Due to a high immiscibility between the diisocyanate and the polyol that were used, the diisocyanate tended to segregate into clusters. When the chain extender was introduced, the urethane bond formation between the chain extender and the diisocyanate occured within these clusters, resulting in a large domains consisting of primarily hard segment. Figure 3.5b shows the result of cross-polarised microscopy of a thermoplastic polyurethane from their work, in which domains can be seen that look visually similar to those seen in figure 3.3. Based on this work it was assumed that the domains in CR1 had indeed formed due to the clustering of hard segments.

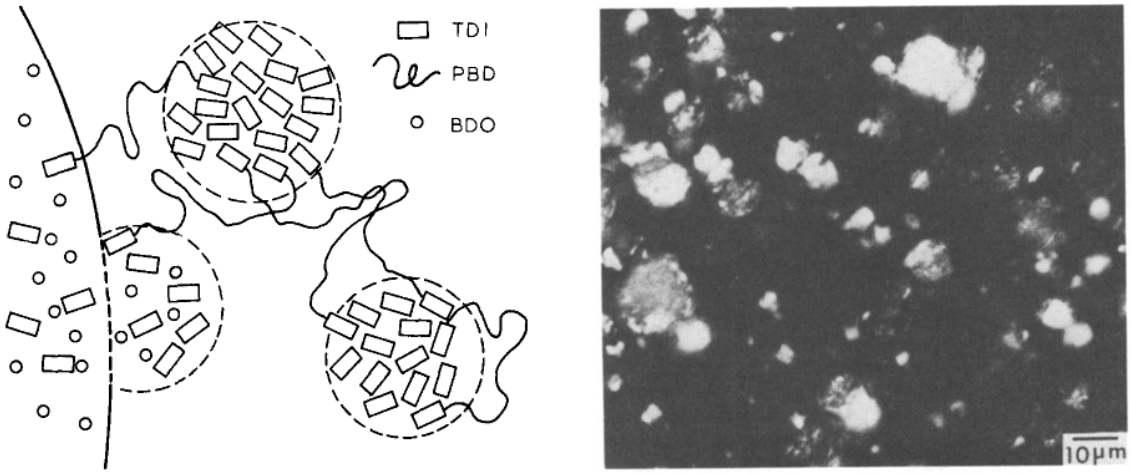


**(a)** Schematic illustration of the formation of large domains containing concentrations of hard blocks.

**(b)** Cross-polarised microscopy of a thermoplastic polyurethane, showing the formed domains, dispersed into a matrix.

**Figure 3.5:** Results of the work of Chen et al. on the clustering of hard segments into domains visible with microscopy [77].

### 3.1.4 Rheology

Figure 3.6 shows the results of the temperature sweep rheology. The elastic modulus and the viscous modulus crossed one another at roughly 195 °C. Above this temperature, the polymer was expected to behave more like a viscous liquid, which made it an important point for melt-processing. Based on these results, 195 °C was suggested as a lower-limit for the processing temperatures.

The next step was to perform shear rate analyses at different temperatures above this cross-point. Figure 3.7 shows the shear rate analyses of both Ninjaflex and CR1. Comparing figure 3.7b to figure 3.7a, it became clear that CR1 had a different rheological behaviour than Ninjaflex. A notable difference was the shape of the curves: the Ninjaflex curves were flat until they reached a certain shear rate, typically between $10^1$ 1/s and $10^2$ 1/s. For CR1, this behaviour was less stable. Another observation was that the viscosity of Ninjaflex was below $10^3$ at printing temperatures, for shear rates up to 15 1/s. CR1 only reaches these values at 225 °C. Some of the curves in figure 3.7b end prematurely, because the applied shear stress exceeded the critical shear stress of the polymer and it failed.

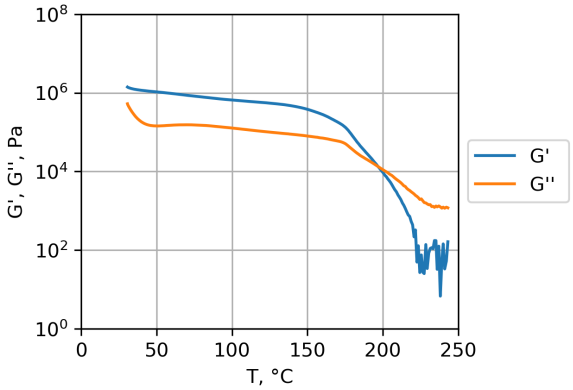


**Figure 3.6:** Storage modulus and loss modulus during the temperature sweep of CR1.

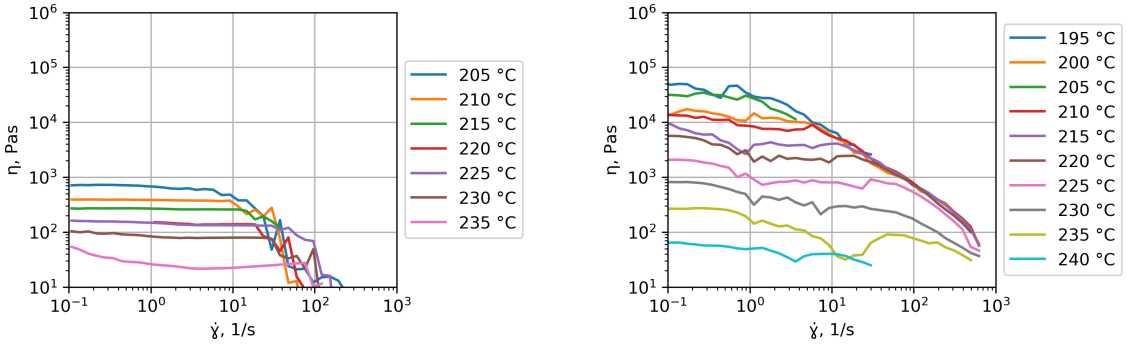


**(a)** Shear-rate analyses for Ninjaflex at different temperatures.

**(b)** Shear-rate analyses for CR1 at different temperatures.

**Figure 3.7:** Results of the shear rate analyses.

The 235 °C curve showed a drop in viscosity and then shear thickening at a shear rate of around $10^1$ 1/s. A possible explanation for this could be slipping between a plate of the rheometer and the sample during these measurements.

The relationship between shear rate and shear stress for CR1 at different temperatures is shown in figure 3.8. A power law curve was fitted to each graph and the power law constants were calculated according to equation (1.1) and shown in table 3.1.

**Table 3.1:** Power law constant of CR1 at different temperatures.

| | **Temperature, °C** | | | | | | | | | |
|---|---|---|---|---|---|---|---|---|---|---|
| | 195 | 200 | 205 | 210 | 215 | 220 | 225 | 230 | 235 | 240 |
| **n, -** | 0.71 | 0.89 | 0.95 | 0.82 | 0.92 | 0.93 | 0.95 | 0.96 | 0.98 | 0.98 |
| **K, Pa·s** | $2.0{\cdot}10^4$ | $1.2{\cdot}10^4$ | $2.5{\cdot}10^4$ | $7.8{\cdot}10^3$ | $7.8{\cdot}10^3$ | $4.9{\cdot}10^3$ | $4.7{\cdot}10^3$ | $4.9{\cdot}10^3$ | 215 | 42 |

The power law coefficient $n$ increased with the temperature, which means that the polymer acts more and more like a Newtonian fluid. $K$ decreased with temperature, indeed showing a decrease in the overall viscosity of the polymer. This agreed with the decreasingly viscous

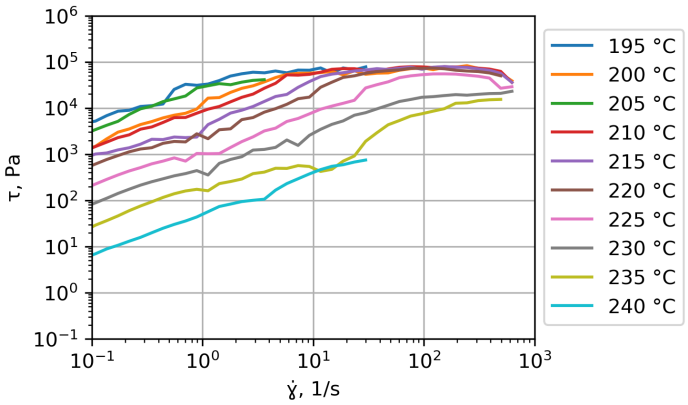


**Figure 3.8:** Shear rate versus shear stress of CR1 at increasing temperatures. These curves could be used to calculate the power law constants of CR1 at these temperatures.

behaviour at elevated temperatures that was seen in figure 3.6. While the polymer showed shear-thinning behaviour at lower temperatures, $n$ approached 1 at higher temperatures.

Based on the comparison with Ninjaflex, 220 °C was chosen as the lower boundary for the printhead temperature. A shear rate rheology measurement were also conducted at 245 °C and 250 °C, but since these measurements failed before a shear rate of $10^{-1}$, it suggested that the viscosity of the polymer was too low to retain sufficient consistency during the measurement, which suggested that it would also not have enough consistency to be printed into a cohesive filament. Based on these measurements and calculations, the range of temperatures that could be suitable for FDM were established to be between 220 °C and 240 °C.

### 3.1.5 DMTA

Results of the DMTA measurements are shown in figure 3.9. DMTA was used to analyse the response of the polymer to repetitive small strain under an increasing temperature. This behaviour should aid in the prediction of the polymers behaviour under compression during FDM and during mechanical testing. Given the set-up of the printer, it was expected that the polymer would already heat up to some extent before entering the hot section of the printer. Therefore, any knowledge about the viscoelastic behaviour under tension and compression was useful in understanding FDM outcomes.

Similarly to rheology, this response is divided into an elastic component (the storage modulus $E'$) and a viscous component (the loss modulus $E''$). The shift between the elastic and the viscous response is represented as $\tan(\delta)$. These curves for CR1 are shown in figure 3.9. In the DMTA curve, the $T_g$ can be identified at three points: the onset of decline in $E'$, the peak in $E$" and the peak in $\tan(\delta)$. The onset of the decline in $E'$ marked the $T_g$ at 9.5 °C. The peak in $E$" marked it at 13.5 °C, and the peak in $\tan(\delta)$ occurred at 18.5 °C. These temperatures were considerably higher than the glass transition temperature measured during DSC, which is not abnormal [78].

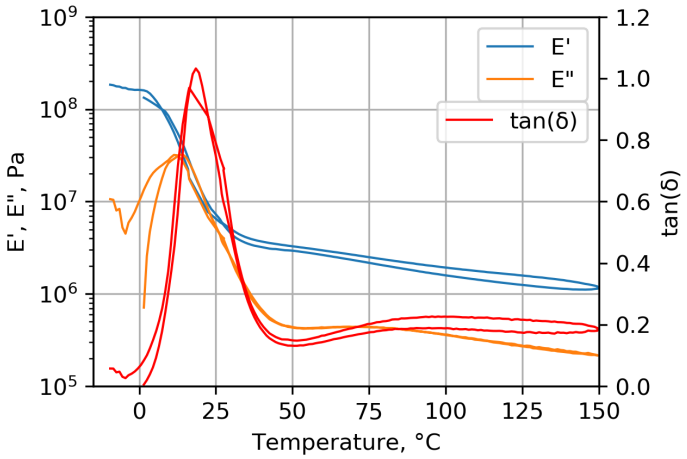


**Figure 3.9:** DMTA curves of bulk CR1.

Figure 3.9 bears some resemblance to figure 3.6. The polymer was going through a thermal transition at room temperature. This meant that the mechanical properties of the polymer were highly sensitive to the temperature. The polymer becoming mobile at such moderate temperatures indicated that the temperature before the hot section of the print head must be kept as low as possible in order to prevent buckling and clogging of the system.

## 3.2 Final remarks

TGA measurements showed that degradation of the polymer initiated at a temperature of roughly 250 °C, while 0.2 % weight loss was accumulated only at 290 °C. Based on this information, it would be preferable to process the polymer at a temperature below 250 °C, in order to prevent thermal degradation of the urethane bonds.

However, the crossing of the viscous and elastic modulus of CR1 at 195 °C observed during rheology suggested that processing of CR1 should occur at temperatures well exceeding 195 °C. Rheology revealed that the viscosity of CR1 only resembles that of commercial filament Ninjaflex at temperatures above 225 °C. Therefore, the temperature range for printing was suggested to be between 220 °C and 240 °C. The 220 °C was chosen as a temperature at which one would expect no printing given the results presented in figure 3.7. The upper limit of 240 °C was selected based on the availability of rheology data.

DMTA results revealed that the viscoelastic response of the polymer was rapidly changing at room temperature, since the onset of decline of the storage modulus occurred at 9.5 °C, and would not plateau until 30 °C. This revealed that the temperature of the filament would have a significant effect on the ability to print at certain temperatures and print-speeds.

# Chapter 4

# Filament making

Based on the results and recommendations in chapter 3, the next stage of the thesis could be started: the filament production. In order to transform a plaque of polymer into a filament using the 3DEVO NEXT 1.0 ADVANCED, the polymer first needed to be processed into granules, the process of which is described in section 4.1. Next, the appropriate settings of the filament maker needed to be established, the starting point of which can be found in section 4.2. Then, these were adjusted until a sufficient quality of filament was obtained, as shown in section 4.3. In order to save time and material during the filament making, the settings were chosen based on visual observations. Once these were established, however, the filament was characterised, the results of which are presented in section 4.4. Based on these results, some final remarks were made about the feasibility and quality of filament making with CR1 using the 3DEVO NEXT 1.0 ADVANCED in section 4.5.

## 4.1 Granulate production

In order to be processable by the 3DEVO NEXT 1.0 ADVANCED, the polymer needed to be processed into granules of a size of at most 3.5 mm in each direction. Several approaches were attempted in order to create these granules. The high toughness and high flexibility of CR1 resulted in issues in its processing. A first trial by immersing the polymer in liquid nitrogen and hitting with a hammer did not result in any shattering of the polymer.

Next, a mould was produced as a flat aluminium plate containing holes with a diameter of 3 mm. The concept was based on heating the polymer and pressing it into the plate, such that a thin sheet with small pillars would be created that could easily be cut up into granules of the desired size. However, moulding the polymer at moderate temperatures required high forces, which then made it impossible to remove the samples from the mould.

Another approach that was attempted was the use of a rotor mill: the Pulverisette 14 premium by Fritsch. Using the cutting rotor, a 0.8 mm sieve (the coarsest available at the time) and liquid nitrogen for cooling, the polymer could be shredded into a coarse powder. However, even under liquid nitrogen cooling, the polymer tended to generate heat to the point of it melting and even degrading, causing it to be smeared instead of cut by the instrument. Two hours were required to process 60 grams of CR1 into only 5 grams of the powder. Moreover, the relatively small size of the pellets was undesirable, for reasons explained in section 4.3. Fritsch offers sieves with a hole diameter of up to 6 mm, so a 4 mm or 2 mm sieve could also be used [1]. These were however not directly available at the time of the thesis, and this was therefore left as a recommendation.

Finally, the solution that was opted for was cutting the polymer by hand into 2-3 mm pieces. Although labour intensive, this method resulted in pellets of the correct size while there was no requirement for the investment in additional equipment. A picture of the granules can be seen in figure 4.1.

**Figure 4.1:** A batch of pellets cut from a CR1 plaque.

## 4.2 Machine settings: starting point

Initial machine settings were chosen based on the results presented in chapter 3. The highest temperature in the four heating zones was $T_2$, the second closest to the exit, at 200 °C. $T_1$ was chosen to be lower, at 190 °C, in order to allow the filament to cool down slightly before the exit, making it easier to form into the correct shape and thickness. The screw rotation was set to the standard for PLA: 6.5 RPM. The fan power was maximised such that the polymer would cool down before touching the feeder wheels. Finally, the filament thickness was set to 3.00 mm, which was the larger filament size for the chosen printhead.

[1] https://www.fritsch-international.com/sample-preparation/milling/rotor-beater-mills/details/product/pulverisette-14-premium-line/accessories/

**Table 4.1:** Initial settings of the 3DEVO Next - ADVANCED filament maker for CR1.

| T1 | T2 | T3 | T4 | Screw RPM | Percentage fan power | Filament thickness |
|---|---|---|---|---|---|---|
| 190 °C | 200 °C | 195 °C | 180 °C | 6.5 RPM | 100 % | 3.00 mm |

## 4.3 Results

It turned out that using the 3DEVO NEXT 1.0 - ADVANCED filament maker for CR1 was not straightforward. Due to the relatively small distance between the heated sections and the inlet of the extruder screw, the temperature at the inlet was high enough to cause the pellets of CR1 to quickly "heal" together into larger chunks. Therefore, the pellets were added gradually. Nevertheless, the inflow of material into the extruder was unsteady, which resulted in an unsteady diameter of the filament. As a result, a filament diameter of 3 mm could not be obtained, and the filament thickness was reduced to 1.75 mm. The processing temperatures were found by increasing the temperatures mentioned in section 4.2 with 5 °C increments. The screw RPM was chosen such that it would enable sufficient heating of the polymer over time, while also being compatible with the lower limit on the speed of the puller wheels.

The final settings of the 3DEVO NEXT 1.0 - Advanced can ben seen in section 4.3. The set-up of the filament maker put a limit on the quality of the filament that could be attained. The resulting filament showed significant variations in thickness, from sections with a diameter of 1.3 mm to sections with a diameter of 2.3 mm. This meant that a significant amount of the filament was of no use for printing.

**Table 4.2:** Final settings of the 3DEVO Next - ADVANCED filament maker for CR1.

| T1 | T2 | T3 | T4 | Screw RPM | Percentage fan power | Filament thickness |
|---|---|---|---|---|---|---|
| 210 C | 220 °C | 215 °C | 200 °C | 6.5 RPM | 60 % | 1.7 mm |

It took 3 hours to process 200 grams of pellets, out of which no more than 35 grams of useful filament could be made each time. Filament making was conducted a total of 3 times.

**Figure 4.2:** Photo of the CR1 filament.

## 4.4 Characterisation

### 4.4.1 TGA

Figure 4.3 displays the results of the TGA measurements of the filament, compared to the bulk polymer. First of all, there was no weight loss at 100 °C, which ruled out the presence of moisture in the filament. Moisture in the filament would result in the formation of gas bubbles during FDM, since the printing temperature would exceed the boiling point of water.

There was, however, a difference in the degradation behaviour of the bulk and of the filament, where the curve of the filament has shifted to a higher temperature, although the temperature of 0.2% weight loss has lowered to 256 °C. This was also seen in repeat measurements. A possible cause of this increased thermal resistance was the presence of a higher amount of hydrogen bonding in the filament when compared to the bulk.

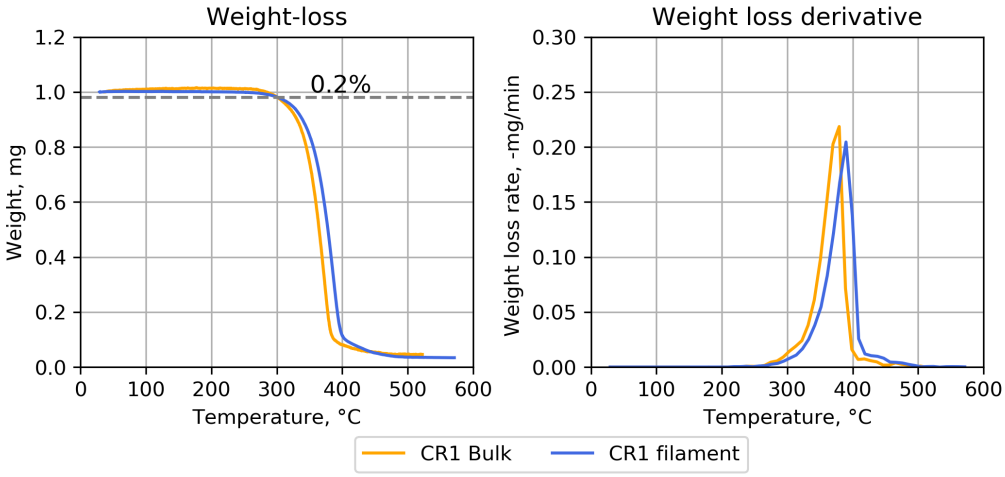


**Figure 4.3:** Results from the TGA analysis of the filament compared to those of the bulk.

### 4.4.2 DSC

Figure 4.4 shows the results of the DSC measurement of the filament, compared to the bulk. The measurement was from the first heating. At low temperatures, the behaviour of the bulk and the filament was comparable, although the signal iwas always slightly lower for the filament. At 13 °C, the signal starts to deviate. An immediately obvious difference between the DSC of the filament and the bulk is the endothermic peak at 48 °C. During the filament making, the material was stretched in order to control the diameter. As a result, it was expected that phase mixing occurred (with or without hydrogen bonding between the hard segment and the soft segment), which likely resulted in the presence of this peak [79]. The peak may be attributed to the reorganisation of the polymer and the relief of any stresses induced during filament making. It confirmed the presence of residual stresses caused by processing and an increase in mobility at 48 °C in order to relieve these stresses.

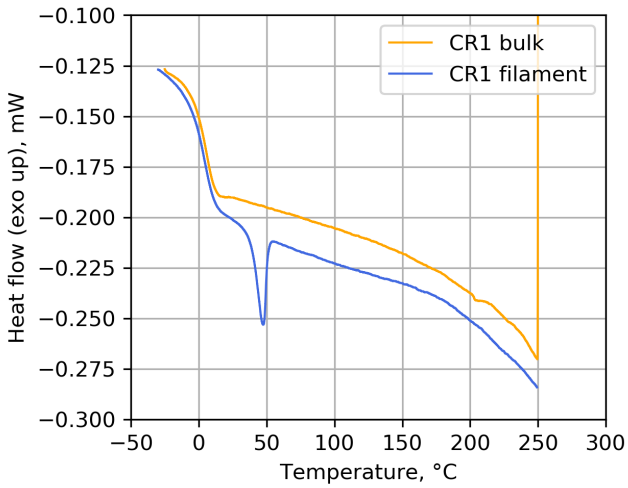


**Figure 4.4:** Heating curve of the DSC measurement of CR1 filament.

### 4.4.3 ATR-imaging

Figure 4.5 shows the results of the structure analysis by ATR-imaging of the filament and the bulk CR1. The structure of both samples appeared similar, with domains with a size of several tens of micrometers. The structure of the filament appears to contain fewer domains with a size exceeding 50 $\mu$m, while containing more domains with a size smaller than 10 $\mu$m. The total area of the domains with respect to the area of the matrix did not change significantly. The total domains area coverage did not change significantly: it was 10.04% in the bulk and 10.01% in the filament. The average domain size remained unchanged at 592 $\mu m^2$.

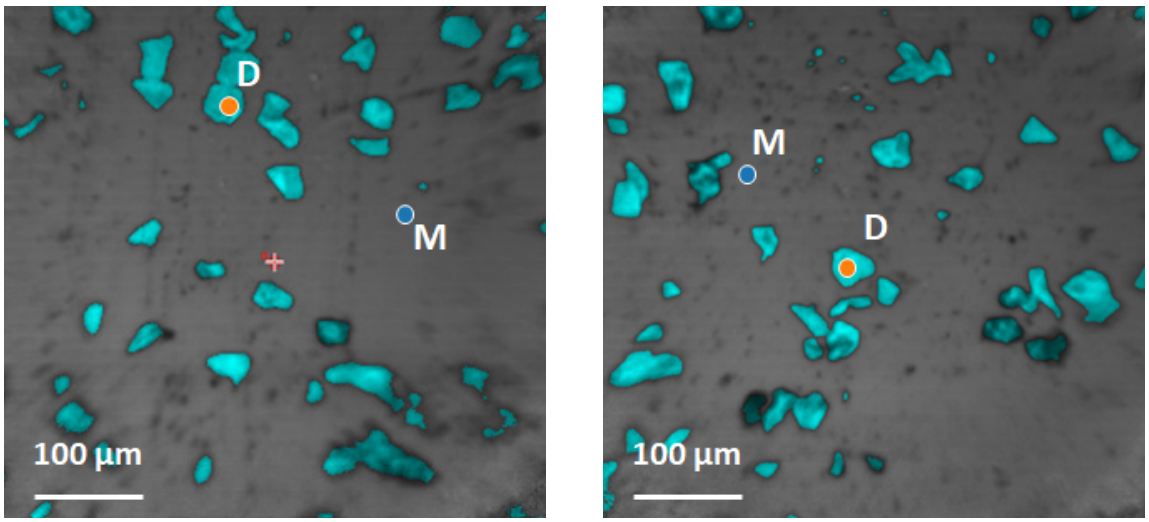


**(a)** Bulk CR1. **(b)** Filament.

**Figure 4.5:** ATR image of the surface of CR1 filament, distinguishing the structure of FTIR spectra throughout the scan. A point in the matrix is marked by **M**, and a point in the domains is marked by **D**.

Next, the composition of these phases was compared in figure 4.6. Comparing the spectra of the matrix and the domains, there were no significant shifts of the peaks in the spectrum of the filament compared to that of the bulk.

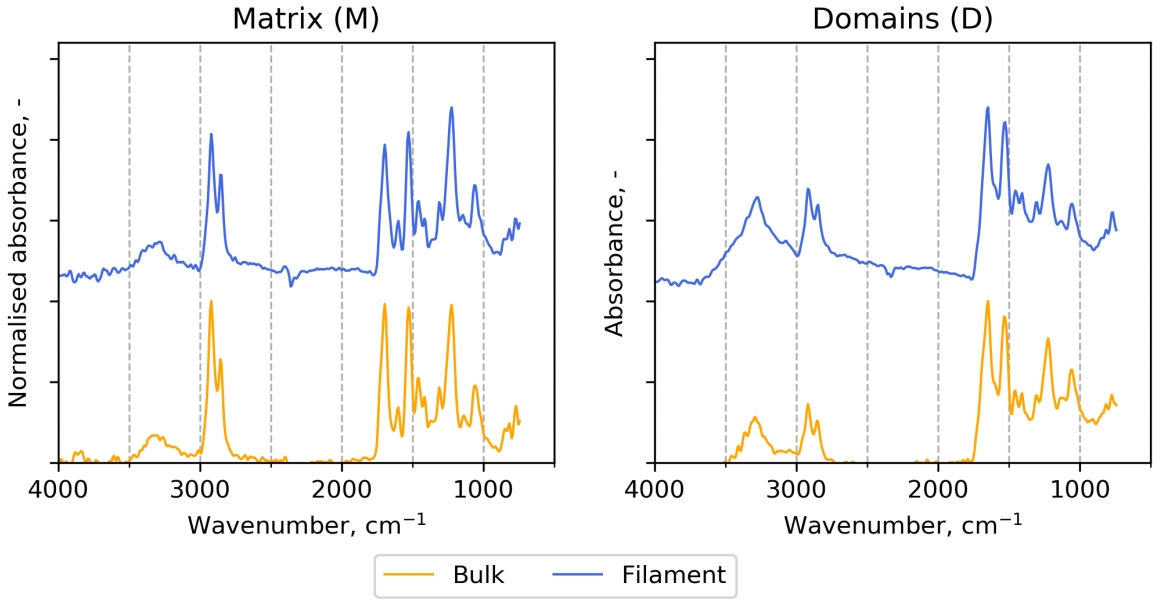


**Figure 4.6:** Absorbance spectra of the matrix and domains of the bulk CR1 and CR1 filament.

### 4.4.4 TMA

The endothermic peak observed in figure 4.4 raised a question: if there were residual stresses in the filament that were relieved when it was heated up, would these also cause a change in the dimensions of the filament? In order to answer this question, a TMA analysis was conducted on the bulk polymer, as well as on the filament in both the lateral and axial direction, the results of which are shown in figure 4.7.

The bulk measurement revealed that the polymer had a slight thermal expansion. The filament shrunk axially while it expanded laterally, this meant that the filament would increase in diameter during FDM. If the temperature was increased beyond 120 °C, the curve first became flat and then started to shrink. For the lateral direction of the filament, the shrinking was accelerated. Since the channel of the filament only slightly exceeded the 1.75 mm diameter, the increase in thickness caused the filament to get stuck when it was heated and expanding. For this reason, the diameter of the filament maker was adjusted down to 1.7 mm.

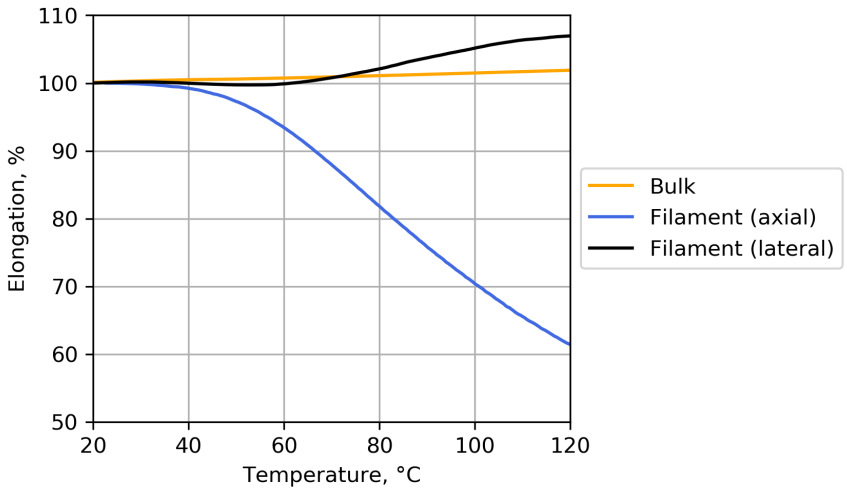


**Figure 4.7:** TMA results of the CR1 bulk and CR1 filament.

## 4.5 Final remarks

This chapter has shown the successful processing of CR1 into a filament fit for 3D printing by FDM. The filament fulfilled the requirements mentioned in section 1.6. The filament was visually similar to bulk CR1 and did not contain voids. Even though the cross-over temperature of the elastic modulus and the viscous modulus was 195 °C, the temperature in the filament maker needed to be increased to 220 °C in order to be able to process the polymer successfully into a filament.

Characterisation of the filament indeed revealed that it was possible to produce a filament of CR1 with properties very similar to those of the bulk. ATR imaging revealed no significant changes in the structure of the polymer and TGA and DSC excluded the presence of water or residue polymer from the filament maker. Nevertheless, the method of filament making introduced some thermal stresses into the filament, visible by the endothermic peak at 45 °C, resulting in a change in the dimensions of the filament.

# Chapter 5

# Fused deposition modelling of CR1

This chapter describes the results of FDM with CR1. Section 5.1 discusses the additional alterations made to the 3D printer. Section 5.2 describes the preparations made before FDM with CR1. Section 5.3 shows the results of FDM, and section 5.4 discusses the characterisation of the print with the best optical quality. Finally, section 5.5 presents the results of mechanical testing of the 3D printed CR1 sample, compared to bulk CR1 and Ninjaflex.

## 5.1 Machine alterations and settings

The set-up described in chapter 2 was set up to work with Ninjaflex, but initial trials with CR1 revealed that the set-up was inadequate. It turned out to have insufficient cooling between the feeder wheels and the hot-end. This caused the CR1 filament to buckle and block the print-head. Therefore, a combination of the E3D Titan extruder with a V6 hot-end was chosen. The connection between the axes of the printer and the print-head was produced using a stereolithography 3D printer (Formlabs form 2). In order to help the material to maintain stability after exiting the nozzle, an additional fan was installed and a duct was printed using the Formlabs form 2; it was attached with a rig printed by the Ultimaker 2+ itself. The printhead can be seen in figure 5.1. The nozzle was also changed from a 0.4 mm exit to a 0.8 mm exit, in order to reduce the pressure build-up in the nozzle and therefore make printing easier.

G-code files for printing were generated using CURA software (4.3.0), the settings of which can be found in appendix B. Certain printing parameters were kept constant while others were varied. The settings that were varied were the printing temperature ($T_{print}$), the printing speed ($V_{print}$) and the infill line distance ($d_{infill}$). $d_{infill}$ was kept at 0.8 mm for the CR1 samples, based on recommendations by Ultimaker. The layer height was set to 0.4 mm, which is relatively high for FDM, but this reduced the back-pressure during printing. Finally, the print-bed temperature was set to 30 °C.

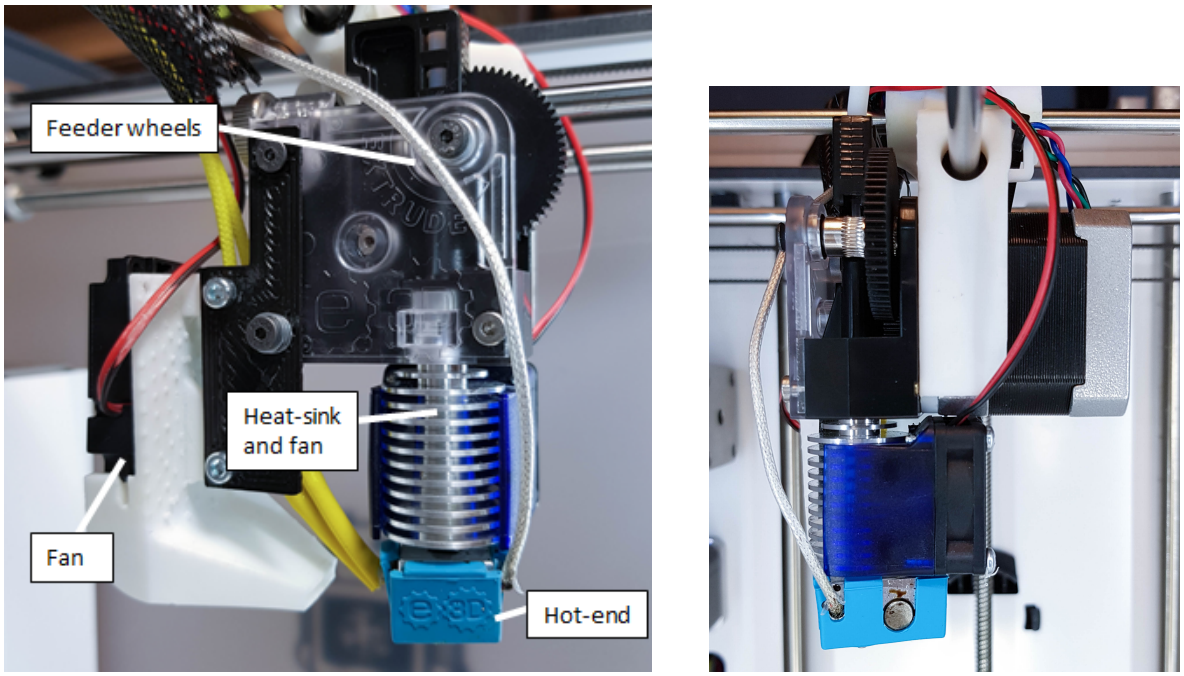


**(a)** Left side of the modified printhead, marking some important components.

**(b)** Front of the modified printhead.

**Figure 5.1:** Modified printhead, with a Titan Aero extruder and V6 hot-end.

## 5.2 Preparations before FDM

### Geometry of the prints

The polymers were printed into a rectangular bar measuring 1 by 2 cm and 0.5 cm in height. A picture of the print preview by CURA can be seen in figure 5.2. The printing direction was chosen such that there would be fewer direction changes during printing.

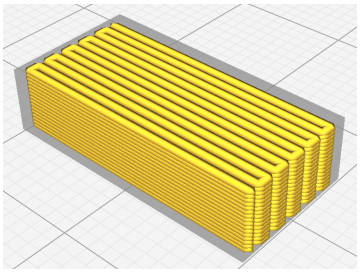

**Figure 5.2:** Print preview of the samples in CURA.

### Preparing the filament

Each print required 40 cm of filament. To select suitable filament, the diameter was measured once every 5 cm using a caliper. If the average diameter was between 1.55 mm and 1.70 mm with a standard deviation of at most 0.1 mm, the filament was employed. The filament diameter in CURA was adjusted to the average in order to compensate the feed rate.

### Selecting the print-settings

The volumetric flow rate for each speed could be calculated according to equation (5.1) and can be found in table 5.1. Since the cross sectional area ($A$) of the nozzle exit was constant at 0.8 mm, the print speed was a linear function of the volumetric flow rate. Since the print-speed could easily be altered in the software, this was chosen as a variable.

$$Q = V_{print} \cdot A \tag{5.1}$$

**Table 5.1:** Conversion of the printing speed to the volumetric flow rate in the printer.

| $V_{print}$, **mm/s** | 1 | 5 | 10 | 20 | 40 |
|---|---|---|---|---|---|
| $Q$, **mm$^3$/s** | 0.50 | 2.51 | 5.03 | 10.5 | 20.11 |

Based on this volumetric flow rate and the nozzle diameter, the viscosity of the polymer in the nozzle exit could be deduced from the rheology measurements in section 3.1.4. Using the power law constants in table 3.1 and the volumetric flow rate from table 5.1, the shear rate experienced by the polymer in the nozzle during FDM was calculated according to equation (1.7). From the shear rate analyses in figure 3.7b, the viscosity at this shear rate and temperature could be obtained. The resulting viscosity as a function of print speed can be seen in figure 5.3.

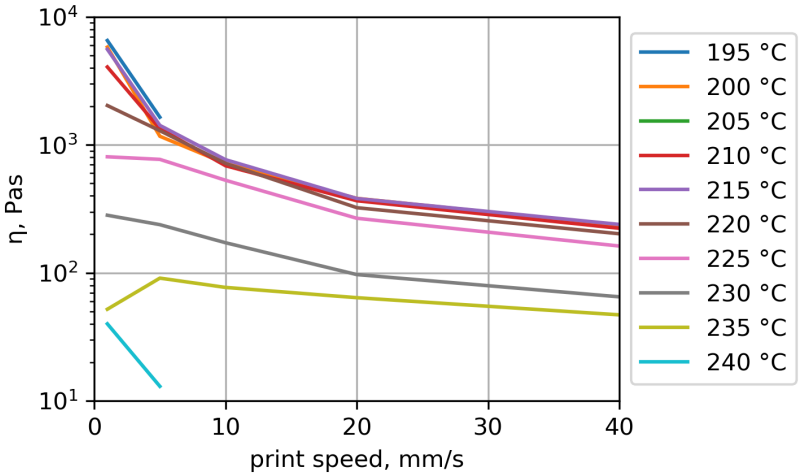


**Figure 5.3:** Viscosity of CR1 at the different printing temperatures and printing speeds.

The final matrix of tested print-speeds and print temperatures can be seen in table 5.2. If the print failed within the first layer, it would be attempted three more times. If it failed three times in the first layer, it would be counted as not possible.

**Table 5.2:** Test matrix with the settings for the 3D printing of CR1.

| | | $V_{print}$, mm/s | | | | |
|---|---|---|---|---|---|---|
| | | **1** | **5** | **10** | **20** | **40** |
| $T_{print}$, °C | **220** | 220_1 | 220_5 | 220_10 | 220_20 | 220_40 |
| | **225** | 225_1 | 225_5 | 225_10 | 225_20 | 225_40 |
| | **230** | 230_1 | 230_5 | 230_10 | 230_20 | 230_40 |
| | **235** | 235_1 | 235_5 | 235_10 | 235_20 | 235_40 |
| | **240** | 240_1 | 240_5 | 240_10 | 240_20 | 240_40 |

## 5.3 Printing rectangular samples with CR1

The results of the thickness measurements of the piece of filament used for each printing condition can be found in table 5.3.

**Table 5.3:** Average thickness of the filaments used during the printing.

| | | $V_{print}$, mm/s | | | | |
|---|---|---|---|---|---|---|
| | | **1** | **5** | **10** | **20** | **40** |
| $T_{print}$, °C | **220** | 1.60 ± 0.03 | 1.60 ± 0.03 | 1.60 ± 0.03 | 1.69 ± 0.05 | 1.72 ± 0.04 |
| | **225** | 1.58 ± 0.06 | 1.58 ± 0.06 | 1.59 ± 0.06 | 1.59 ± 0.06 | 1.56 ± 0.04 |
| | **230** | 1.65 ± 0.04 | 1.61 ± 0.06 | 1.58 ± 0.09 | 1.58 ± 0.04 | 1.69 ± 0.06 |
| | **235** | 1.65 ± 0.04 | 1.56 ± 0.09 | 1.53 ± 0.06 | 1.67 ± 0.06 | 1.67 ± 0.09 |
| | **240** | 1.56 ± 0.06 | 1.63 ± 0.09 | 1.69 ± 0.06 | 1.65 ± 0.9 | 1.63 ± 0.09 |

The results of FDM with CR1 at different printing speeds and different temperatures are shown in table 5.4. The filament was inserted after the print-head had heated up, so that there was no chance of it softening without moving down the printhead.

**Table 5.4:** Results of FDM with CR1 at different printing speeds and different temperatures.

| | | $V_{print}$, mm/s | | | | |
|---|---|---|---|---|---|---|
| | | **1** | **5** | **10** | **20** | **40** |
| $T_{print}$, °C | **220** | Nothing | Nothing | Nothing | Nothing | Nothing |
| | **225** | Nothing | **Worked** | **Worked** | **Worked** | Failed (4) |
| | **230** | Nothing | **Worked** | **Worked** | **Worked** | Nothing |
| | **235** | Nothing | Nothing | **Worked** | **Worked** | Nothing |
| | **240** | Nothing | Nothing | Nothing | Nothing | Nothing |

The lowest and the highest printing speeds (1 mm/s and 40 mm/s) did not result in successful printing. Similarly, the lowest and the highest temperatures (220 °C and 240 °C) did not result in successful printing. The lowest temperature resulted in insufficient flow, while the highest temperature resulted in gas formation, increasing pressure in the nozzle.

As can be seen in figure 5.4, finding out when printing was possible was not a simple matter of viscosity. The ability to print could instead rely on the interplay of a variety of properties. The contact area between the filament and the print-channel, the thermal conductivity of the polymer and the print speed determined the temperature distribution of the filament. The complicating factor for elastomers was their low buckling load. The DMTA results of CR1 showed that the polymer was in a thermal transition and therefore especially sensitive to temperature changes, this severely limited the range of printing temperature and speed.

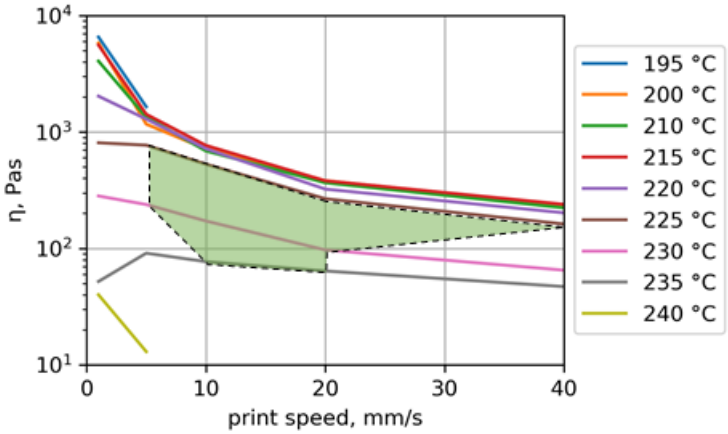


**Figure 5.4:** Viscosity of CR1 at different temperatures and different speeds, connecting the points where printing was possible to mark a window within which printing was possible.

Figure 5.5 shows pictures of the 3D printed samples. A large difference in quality can be seen between the samples. Samples printed at 225 °C were of relatively poor quality, with a high porosity visible on the outside of the specimens. Samples printed at 230 °C and 235 °C looked more regular, where the sample printed at 230 °C and 20 mm/s had the best quality based on this visual inspection. Another notable characteristic of the samples printed at 235 °C was their over-extrusion at the ends, causing the material to leak over. This over-extrusion could be the result of swelling of the polymer.

Figure 5.6 shows the microscopic pictures of the CR1 sample printed at 230 °C and 20 mm/s. The sample was 4.8 mm in height and 9.6 mm in width at the bottom and 9.3 mm at the top. There were no notable boundaries or air-gaps between the rows of deposited filament on the inside of the specimen, only between the subsequent layers. The cross-section of the print was regular, and contained barely any voids. The side of the sample was also slightly more regular, although the height of the layers did change throughout their length.

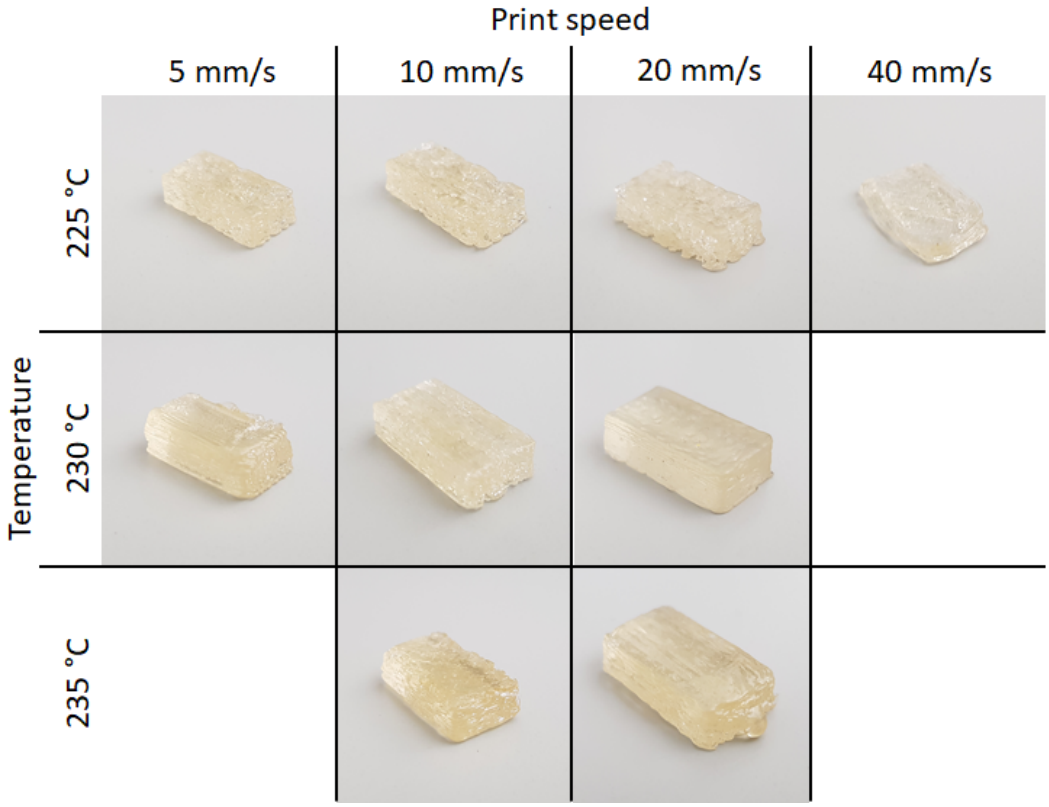


**Figure 5.5:** Pictures of the parts 3D printed with CR1.

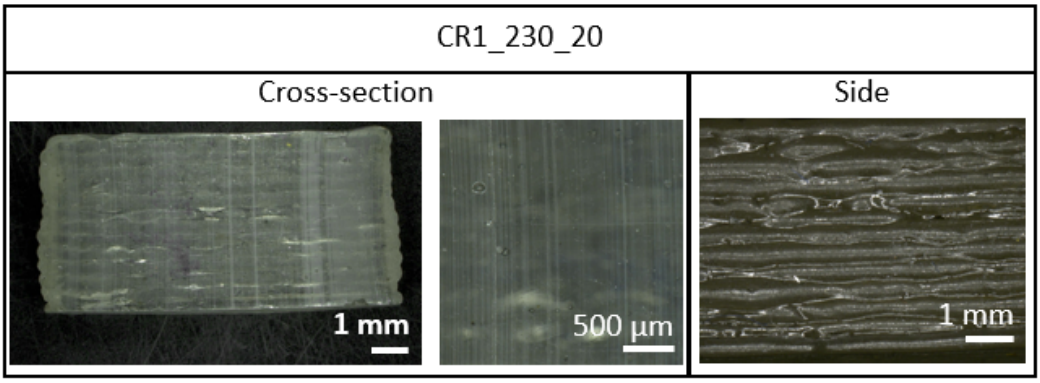


**Figure 5.6:** Microscopic pictures of the CR1_230_20 print: the cross-section (left), a close-up of the cross-section (middle) and the side (right)

### Demonstration of self-supportability

In order to demonstrate the polymers ability to self-support, a hollow-vase structure was printed with Ninjaflex, with CR1 at 230 °C and 10 mm/s and with CR1 at 230 °C and 20 mm/s. The resulting prints, seen in figure 5.7 showed that CR1 was indeed able to self-support a single wall structure after printing. Figure 5.8 shows microscopic pictures of the single wall of the Ninjlaflex print and one of the CR1 prints. Clearly, the quality of the CR1 print was lower, since the layers were less consistent due to an inconstant pressure in the nozzle (presumably caused by filament thickness variation). The CR1 print at 230 °C and 20 mm/s was more consistent than the one printed at 230 °C and 10 mm/s. Nevertheless, these results show good potential of CR1 to be used for more complex prints, since the printed filaments could retain sufficient stability after deposition to not collapse in this structure.

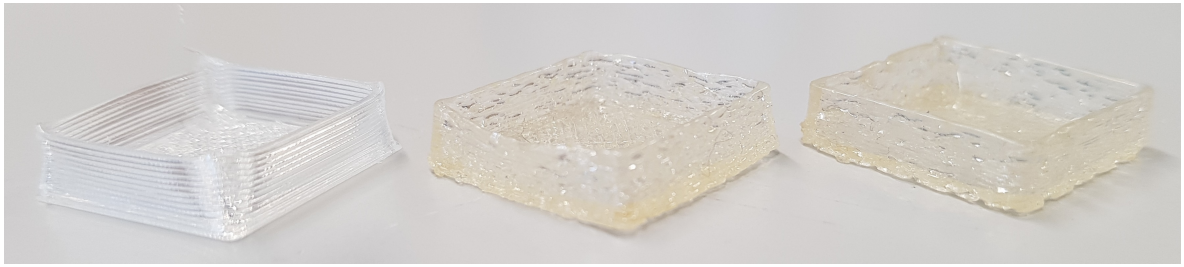

**Figure 5.7:** 3D printed hollow-vase structure with a wall of a single line. With a ninjaflex sample on the left, and two CR1 samples in the middle (230 °C, 10 mm/s) and on the right (230 °C and 20 mm/s).

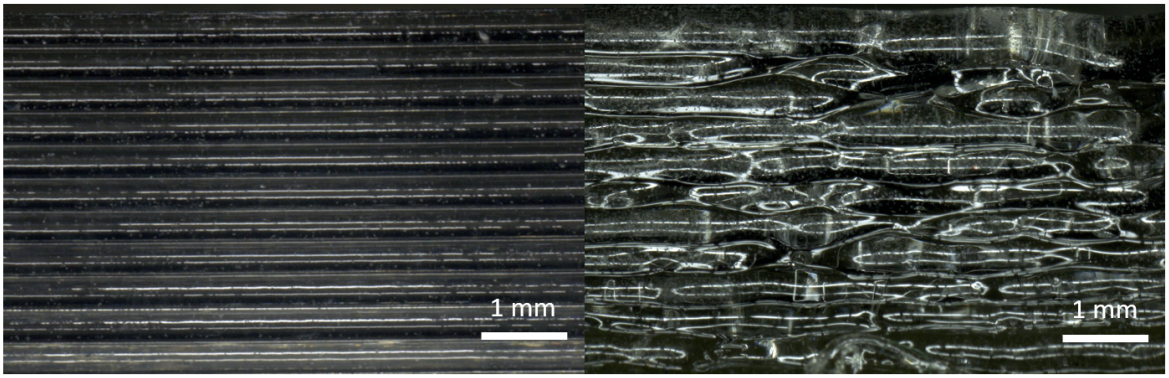


**Figure 5.8:** Microscopic pictures of the single line walls of 3D printed Ninjaflex (left) and CR1 (right, 230 °C, 20 mm/s).

## 5.4 Characterisation

### 5.4.1 ATR-imaging

Figure 5.9 displays the ATR images of the 3D printed CR1 samples. There were significant differences in the distribution of the hard domains throughout the area in each print. The total area of the domains, the average domain size and the number of domains of each print, as well as the untreated CR1 and the CR1 filament can be seen in table 5.5. As discussed in section 4.4.3, the structure of the filament did not change significantly from that of the untreated CR1. 3D printing did however have a significant impact on this structure.

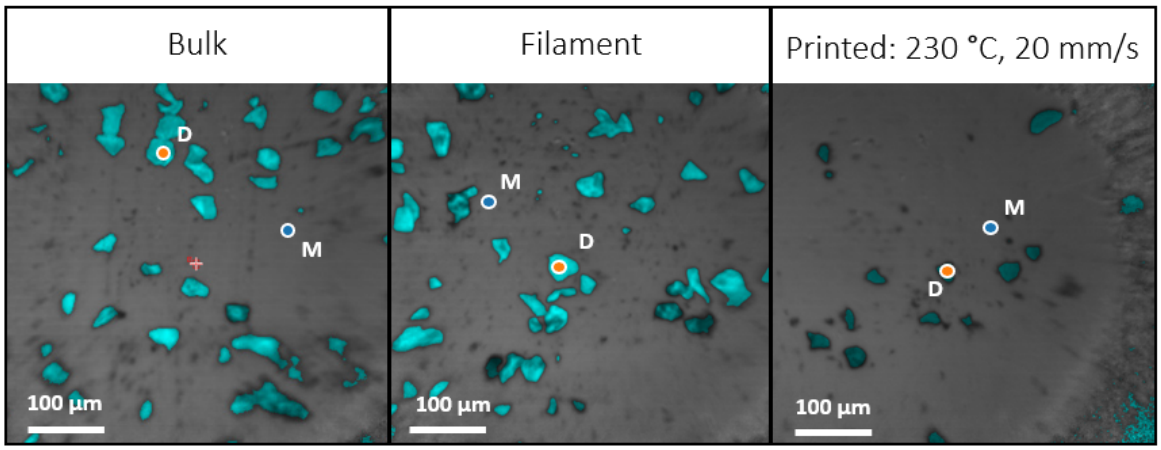


**Figure 5.9:** ATR images of CR1 bulk, filament and of 3D printed CR1 (230 °C and 20 mm/s).

First, the structure of each of the ATR images in figure 5.9 was analysed and quantified in table 5.5. Compared to the bulk and the filament, the 3D printed CR1 had fewer domains. The average domain size was also smaller and the number of domains lower. The shapes of these domains were also more rounded and more regular. Some other the samples did have more domains, covering a larger portion of the surface.

**Table 5.5:** Analysis of the ATR images of bulk CR1, filament made of CR1 and 3D printed CR1 in figure 5.9.

| | Domains area % | Average domain size $\mu m^2$ | Number of domains - |
|---|---|---|---|
| Bulk | 10.04 | 592 | 20 |
| Filament | 10.01 | 592 | 19 |
| Printed: 230 °C, 20 mm/s | 3.23 | 310 | 12 |

In order to learn more about these differences, the FTIR spectra of the domains and the matrices of the ATR images were also considered. Figure 5.10 shows the spectra of the matrix and the domains of the different prints, compared to that of the bulk polymer. In both the matrix and the domains there was a good overlap throughout most of the spectra.In the matrix, the peak at 2900 $cm^{-1}$ was slightly reduced. Since this peak was associated with

the C-H bonds in the soft segment, this suggested that the domains in the print contained a smaller concentration of the soft segment.

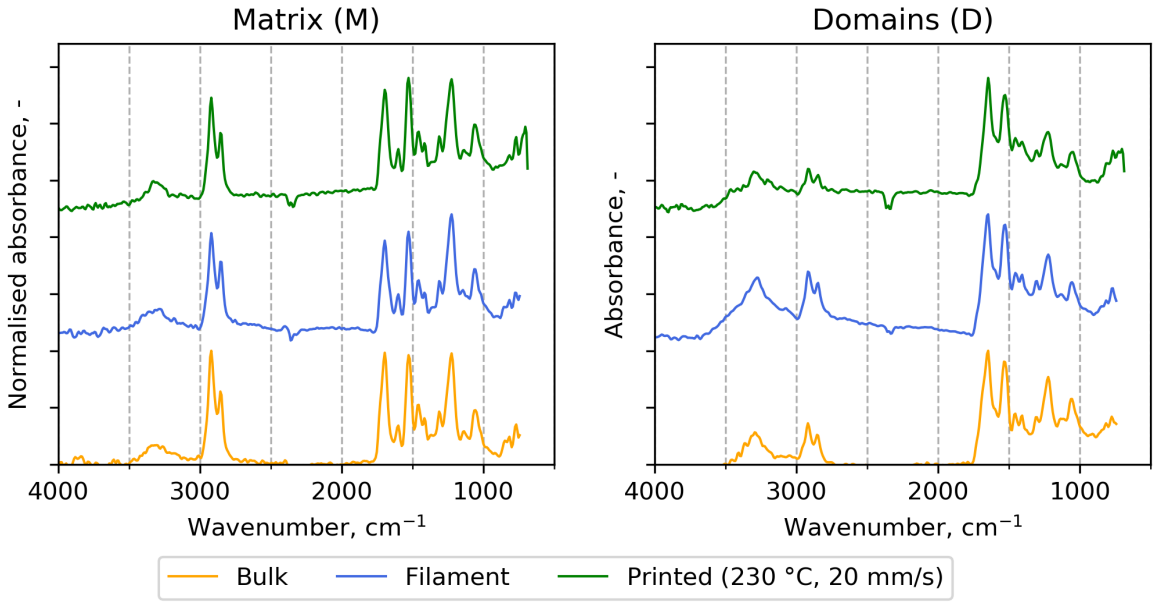


**Figure 5.10:** Spectra of the matrix and domains of the CR1 bulk, filament and print (230 °C, 20 mm/s).

During FDM, the polymer underwent several changes that influenced the shape, size and composition of the domains in the spectra [79, 80]. As the temperature of the polymer was increased in the printhead, the domains containing high concentrations of hard segment would need to disband and dissolve in order to attain sufficient mobility [81]. The application of mechanical stresses experienced by the melt during the extrusion could aid in further separation of these domains. Once extruded, the polymer cooled down, while the hard segments of the polymer were expected to cluster again into new domains. The size and shape of these domains in TPU's have been shown to depend on the cooling procedure [80]. The mobility of the hard-segments to form domains would depend on the temperature during deposition and on the cooling rate.

A schematic representation of the structural changes in CR1 during FDM is shown in figure 5.11. In the filament, the hard segments were hydrogen bonded into hard blocks, which were clustered together into domains. During heating of the polymer in the nozzle, the hard domains were disassociated in order to allow the polymer to flow and to be extruded. After deposition, the polymer would cool down and the hard segments would attempt to cluster back into domains. The cool-down rate would depend on the printing speed and the printing temperature. Since the printing speed was constant for all the prints, the printing temperature was the main variable.

Figure 5.11 presents three cases. In the first example the polymer was cooled down relatively quickly, resulting in a large dispersion of the hard segments into the matrix and the formation of a few clusters. In the middle case, the mobility was high enough to allow some of the hard segments to cluster together, but limited mobility still resulted in the incorporation of the soft segment into these domains. In the bottom case the polymer had sufficient mobility to reform domains similar to those of the filament.

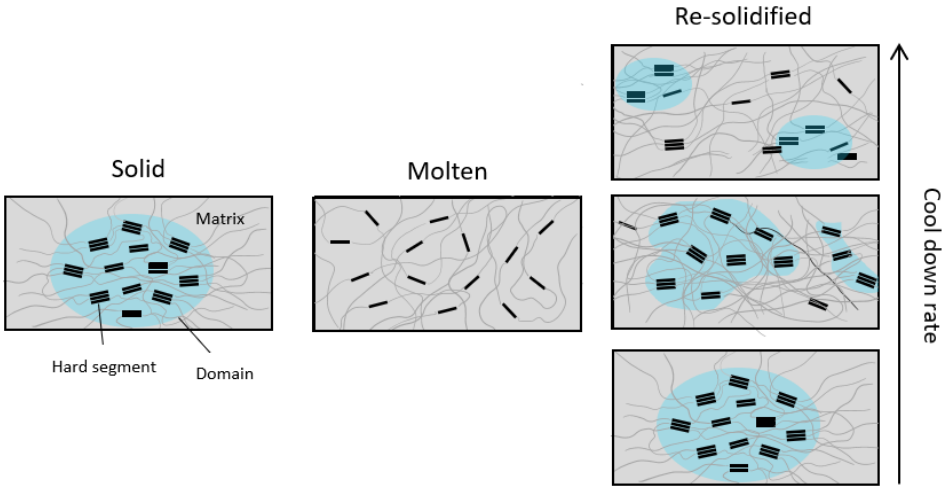


**Figure 5.11:** Schematic drawing of the cluster dissociation and reformation during FDM, depending on the cool-down rate.

## 5.5 Mechanical testing - compression cut test

The print was subjected to the compression cut test, described in chapter 2. Trials of this test are discussed in appendix D. Beside the print, a reference sample of bulk CR1 and a 3D printed Ninjaflex sample were also tested.

Figure 5.12 shows the response of one of the bulk CR1 samples. The response could be divided into 4 regions, combined with pictures taken during the test in figure 5.13, the response of the polymer during these regions could be described.

- The first region between 0.0 mm and 1.0 mm was a linear compression of the sample, with a slope of 8.1 N/mm. During this response, the sample overall was compressed, and only the top of the sample was also deformed due to the blade.
- The second region between 1.0 mm and 2.4 mm was non-linear compression, which could have various causes. The compression behaviour of elastomers is not necessarily linear at higher deformations. The compressive behaviour at different displacements can depend on a number of variables, such as the temperature, load case, strain rate and the polymer itself [82]. Moreover, multiple geometric changes were observed. Material was crowded away by local indentation of the blade, while at the same time the sides of the sample were bulging outwards. At a certain deformation, the friction forces at

the bottom of the sample were overcome, causing the contact surface to expand and leading to a change of the boundary conditions.

- The third region between 2.4 mm and 2.8 mm was another linear regime, with a higher slope than the initial deformation: 55 N/mm. There appear to be fewer geometrical changes in this region, which could suggest that the response is pure compression. However, due to the complexity of the transition region it was not possible to confirm this.
- The fourth region from 2.8 mm to 3.0 mm captured the failure of the sample.

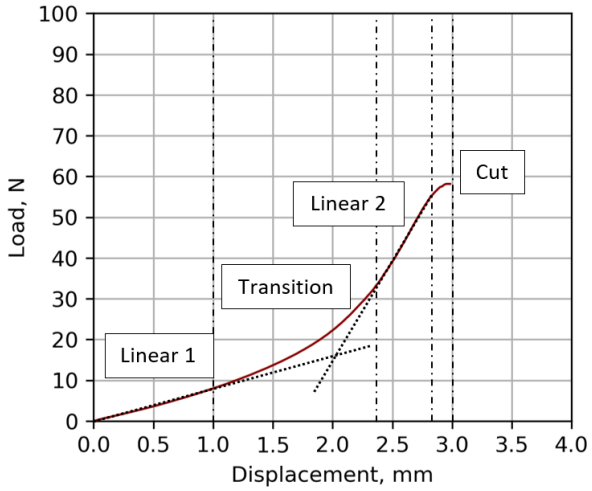


**Figure 5.12:** Force-displacement curve of one of the CR1 bulk samples, indicating the different regions of the response.

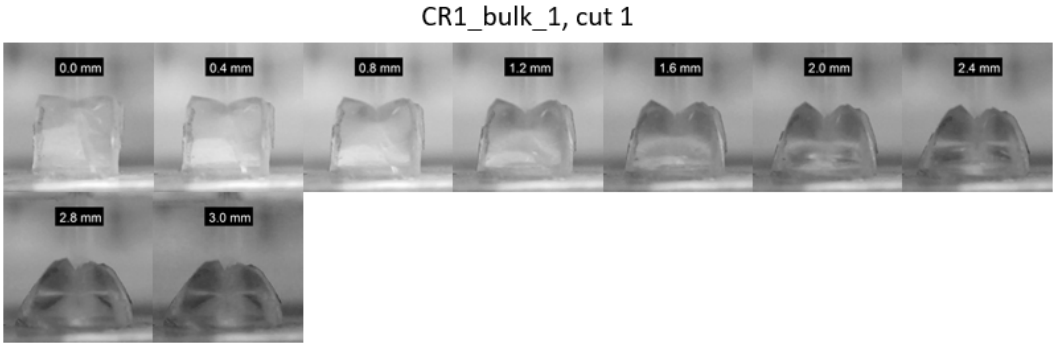


**Figure 5.13:** Stills of compression cut test of CR1 bulk sample 1.

The force-displacement curves of all of the CR1 samples can be seen in figure 5.14. While for the bulk polymer, the test indeed resulted in partial cutting of the samples, the set-up with the current parameters did not result in any cutting of the 3D printed samples. The other three regions could still be distinguished in the responses.

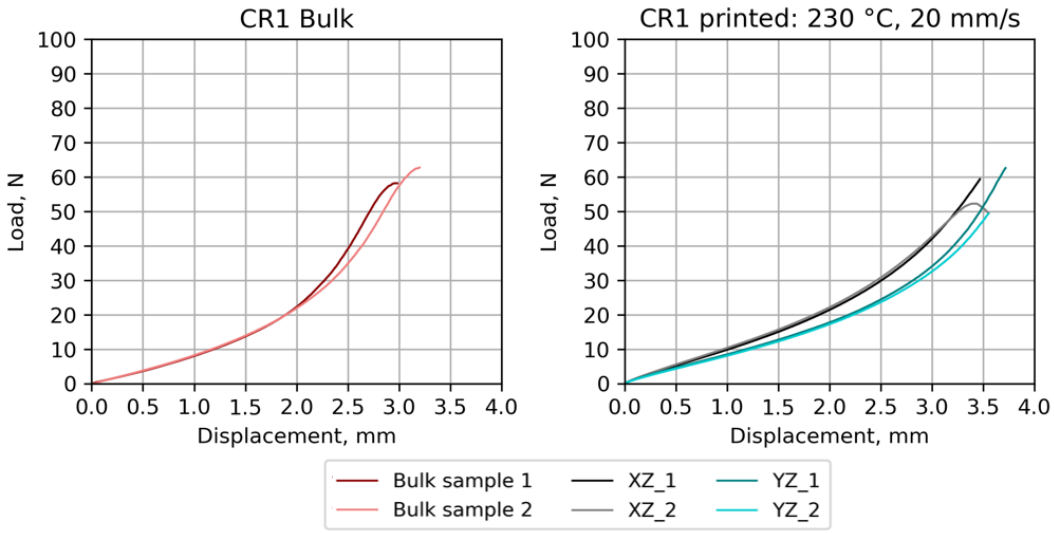


**Figure 5.14:** Force-displacement curves of the compression cut tests of the 3D printed CR1 and bulk CR1.

Overall, the first linear response of the printed samples spanned a longer displacement. In the bulk samples, the transition region started at 1.0 mm, while for the 3D printed samples it started between 1.6 mm and 1.9 mm. Furthermore, the displacement over which the transition region occurred was different for the prints. The second linear region of the prints also started at a larger displacement (2.9 mm vs 3.2-3.3 mm).

There was a difference between the responses of the XZ samples and the YZ samples. The initial slope of the YZ samples was 84% of that of the XZ samples. The slope of the second linear response of the YZ samples was 96% of that of the XZ samples. This indicated that there was some sort anisotropy in the sample. This anisotropy could have been the result of geometrical factors. As seen when discussing the bulk sample, the response measured during this test is complex and dependent on the interplay of a large number of parameters that change constantly during the test.

Compared to the bulk, the force in the printed samples throughout the test was lower for the same displacement, which was likely the result of geometrical factors. At a higher displacement, during the second linear region, the effect of the geometry was assumed to be smaller (because any voids would have been compressed). The slope of this region in the measurements of the print were 78% of that of the bulk in de XZ direction, and 75% in the YZ direction. Due to the limited amount of information available about the polymer, it was not possible to make a well-grounded judgement of the implications of the results presented in figure 5.14.

The self-healing behaviour of CR1 was tested, comparing untreated CR1 to 3D printed CR1 (printed at 230 °C and 20 mm/s) and to Ninjaflex (printed at 235 °C, 20 mm/s and with an infill distance of 0.5 mm). Since the CR1 samples were not successfully cut by the compression cut test, cuts were made artificially with the instron after the first compression cut test.

The force-displacement curves of these experiments can be seen in figure 5.15. The force-displacement curves of 3D printed Ninjaflex were substantially different from those of CR1. These curves showed a region of near–linear compression, followed by a drop. Stills of the test of the XZ_1 sample are shown in figure 5.16. Compared to the response seen when testing the CR1 sample (figure 5.13), the deformation was similar. The force of failure was higher than that of CR1 (bulk), 115 N compared to 60 N. Similar to the printed CR1 sample, a difference in the slope of these samples was seen between the XZ direction and the YZ direction. This difference was much larger than that seen in the CR1 prints. Cutting also occurred at different forces, but at similar displacements.

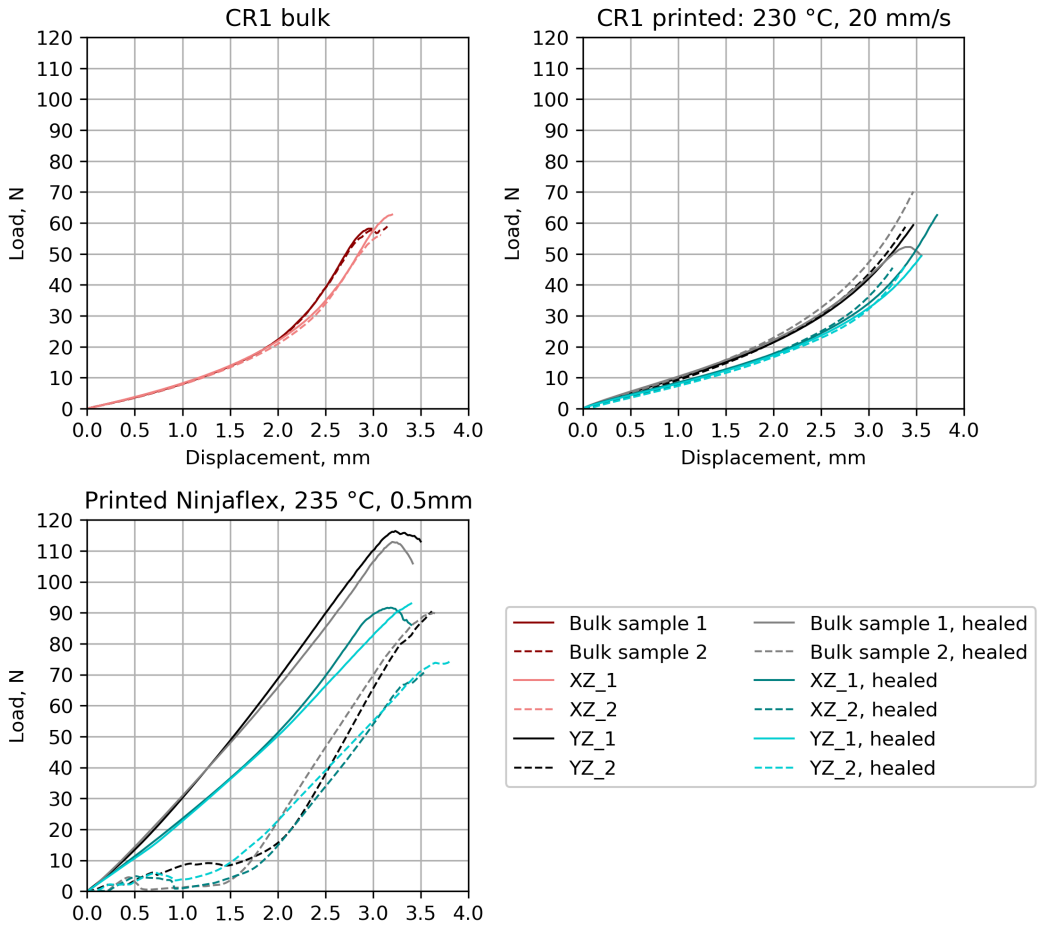


**Figure 5.15:** Force-displacement curves of the healing experiment, showing the response of the samples during the first cut and the second cut after healing.

The results of the bulk samples showed a good overlap in the force-displacement curves of the specimens after healing when compared to the first loading. The same could be said for the 3D printed sample, which also showed good overlap between the initial loading and the loading of the cut and healed sample. The force-displacement curves of Ninjaflex reflected its complete lack of self-healing ability. The forces remained relatively low until around 1.5 mm, when the bottom of the first cut was reached.

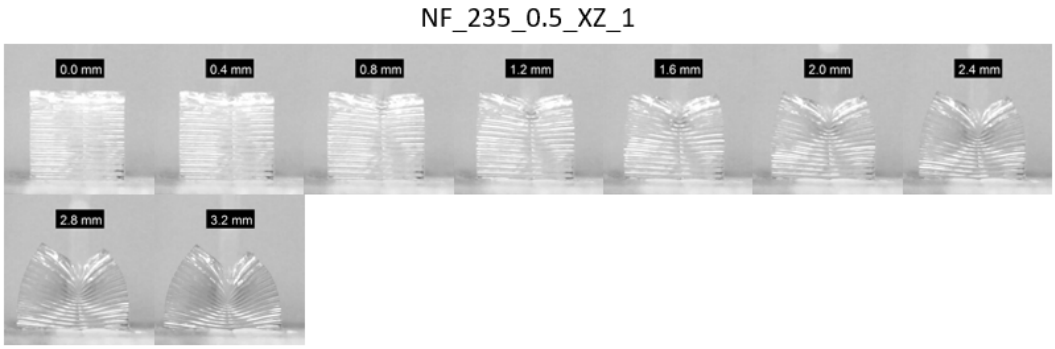


**Figure 5.16:** Stills of compression cut test of Bulk sample 1.

Microscopic pictures of the XZ_1 sample of the 3D printed CR1 after the second cut are shown in figure 5.17. The sample did not fail in the same position twice. Instead, a new, separate cut was formed. Notably, the second test of the printed sample did result in a cut in the sample, which did not happen during the first test. This failure was not seen in the force-displacement curves of these samples.

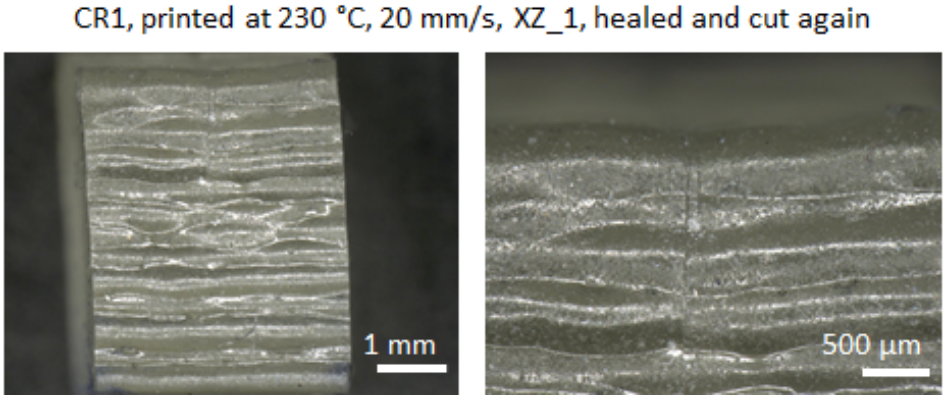


**Figure 5.17:** Microscopic pictures of XZ_1 of 3D printed CR1 after the second cut.

Microscopic pictures of the Ninjaflex sample (figure 5.18) revealed that the second loading of these samples resulted in the opening of the cut made during the first test, which was then deepened during the second test. Microscopic pictures of the other samples can be found in appendix E.

In summary, the printing appeared to not have a significant influence on the mechanical behaviour of CR1 under the compression cut test. The polymer also retained its self-healing ability after printing.

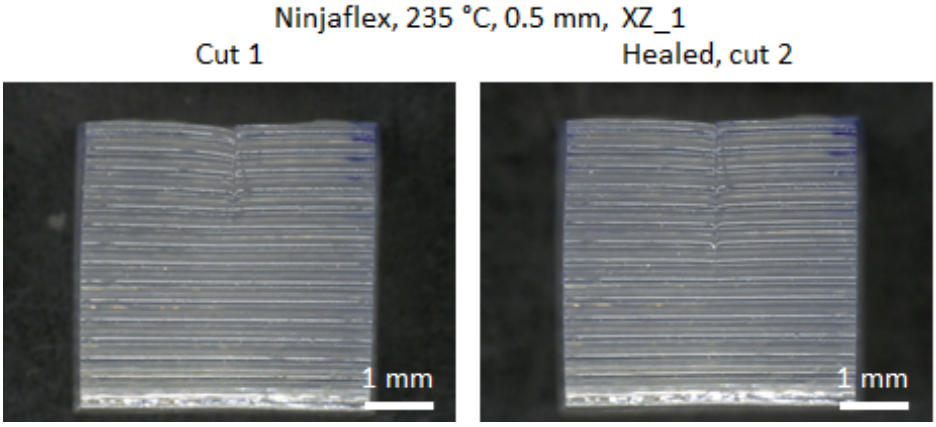


**Figure 5.18:** Microscopic pictures of sample XZ_1 of 3D printed Ninjaflex: after the first cut (left) and the second cut (right).

# Chapter 6

# Conclusions and recommendations

In this chapter, the conclusion and recommendations of the thesis are presented. Section 6.1 discusses the conclusions and section 6.2 discusses some recommendations for future work.

## 6.1 Conclusions

### 6.1.1 Processing of CR1 by filament making and FDM

This thesis successfully demonstrated 3D printing with a self-healing polyurethane: CR1. The following conclusions could be drawn from the processing part of the thesis.

*Using material characterisation techniques and a reference polymer (Ninjaflex in this case), a window of print-head temperature could be established. Rheology and TGA were the most useful techniques for this polymer.*
After synthesising CR1 into the bulk polymer, material characterisation was performed in order to establish relevant characteristics of the polymer behaviour in the context of FDM. TGA revealed the initiation of thermal degradation of the polymer at 250 °C. DSC did not reveal a melting peak in the polymer, which made sense due to its amorphous nature. Rheology did reveal a softening of the polymer above 195 °C. Comparing the viscosity of the polymer as a function of shear rate and temperature to that of a commercial TPU (Ninjaflex) revealed that the viscosity of CR1 was only in the range of that of Ninjaflex at temperatures above 225 °C, which was indeed the lowest temperature at which printing was possible. 3D printing of this very tough but very elastomeric polymer resulted in a very limited range of print-settings. The ability to print could not be reduced to viscosity alone.

*CR1 could be successfully printed at temperatures between 225 °C and 235 °C, with the speed ranging between 5 mm/s and 20 mm/s* Different combinations of print-head temperature and print speed were attempted in order to establish a window of settings within which CR1 could be 3D printed. This window turned out to be relatively small, with the temperature ranging between 225 °C and 235 °C, and the print speed between 5 mm/s and 20 mm/s. The prints

with the best visual quality and accuracy were achieved at 230 °C, with 20 mm/s resulting in the lowest void content and highest accuracy.

*The current set-up was sufficient to print with highly flexible, temperature-sensitive and irregular filaments.* Numerous changes were made to the printing set-up in order to be able to print CR1 with it and obtain high quality results. In spite of the irregular filament with a varying diameter and the low buckling force of the filament due to the elastomeric nature of the polymer, which became soft quickly with an increase in temperature, it was possible to print with the current set-up. This suggested that FDM with similar polymers could also be possible.

*Parts with very low void content could be obtained with little optimisation of the print settings.* By varying the print-speed and printing temperature, samples with very low void content could already be obtained. From microscopic pictures, a printing temperature of 230 °C and 20 mm/s resulted in parts with the fewest voids, highest regularity and without internal boundaries between filaments showing.

### 6.1.2 Mechanical testing of 3D printed CR1

The following conclusions could be drawn about the mechanical testing of 3D printed CR1.

*The compression cut test could be applied as a qualitative and comparative method to study the mechanical properties of 3D printed elastomers when small amounts of material are available. The current set-up was not suitable to characterise the failure of the CR1 samples, but could be used to compare their compressive behaviour and self-healing ability.*
The compression cut test had already been applied to elastomers, but it has also been a common test for foods. The set-up was validated for Ninjaflex, but the combination of low stiffness and high toughness of CR1 resulted in an inability to capture failure of these samples with the displacement used in this work. However, the stiffness of the samples could be tested, and an experiment to characterise the self-healing behaviour of the polymer was also conducted yielding useful results.

*3D printed CR1 showed a compressive behaviour very similar to that of bulk CR1, even without much optimisation.* The curves of the response of the CR1 samples could be divided into three sections: two linear responses connected by a nonlinear transition. This transition initiated at a higher displacement for the prints, possibly owing to effects of the geometry created by the 3D printing. In the response of the prints, a difference could be seen between the response in the XZ direction and the YZ direction, where the XZ direction was generally stiffer (i.e. it required more force to produce the same displacement).

*3D printed CR1 retained at least part of its self-healing property.*
The compression cut test was applied to characterise the self-healing behaviour of a reference unprocessed CR1, 3D printed CR1 and 3D printed Ninjaflex. There was no significant difference between the force-displacement curves of the CR1 samples upon their first loading and upon loading after a cut had been introduced and healed. Microscopic pictures of the cuts revealed that new cuts were made in the samples, rather than the reopening of previous cuts. In the response of the Ninjaflex sample, however, the loading re-opened the previous cut, causing the force to remain low until the blade had reached the bottom of this cut.

## 6.2 Recommendations

### 6.2.1 Processing of CR1 by filament making and FDM

The work presented in this thesis has laid the groundwork for AM with self-healing TPU's. The ability to easily tailor TPU's opens a whole range of possibilities fur further exploration of this subject. However, several issues were encountered during the thesis that could not be resolved in time and thus remain recommendations for further work. In order to perform a wider range of mechanical tests that can be compared to other works and provide more useful information about the performance of the 3D printed CR1 parts.

The ability to create a filament of a reasonable quality highlights the potential of CR1 as a 3D printing material. However, the processing was not without problems that should definitely be addressed in further work on this topic. The following recommendations were made with respect to the filament making process:

- Granulate production: the Pulverisette 14 premium by Fritsch with liquid nitrogen cooling appeared to be the most promising option for granulate production in terms of efficiency. However, due to the equipment available it could not be used successfully during the thesis. It was therefore recommended to use the Pulverisette with a 4 mm or a 2 mm sieve in order to obtain granules fit for the 3DEVO NEXT 1.0 - ADVANCED, liquid nitrogen should be added continuously using the available connection.
- Filament making: the issue of granules fusing at the entrance should be addressed, since this resulted in large fluctuations in the filament diameter and therefore large losses of material. A suggested solution would be the insertion of the granules at a lower temperature, but it must be ensured that there is no chance of water condensation. One could also use a different filament maker. Alternatively, for short lengths of filament, one could attempt to mould filament of a specific diameter and length to ensure accuracy.

The FDM process could also be improved in some areas.

- The printer could be further adjusted to work with the low buckling load of the filament, for instance by implementing a more efficient cooling system. Cooling the filament below its glass transition temperature of 5.5 °C should increase its buckling load, making the printing easier and perhaps even make the window in which printing was possible larger.
- In order to acquire a better understanding of the printing process and the reasons why printing is possible under certain conditions and settings but not others, a more advanced print-head could be used. There have been several in which smart systems have been incorporated in print-heads in order to monitor certain aspects of 3D printing, such as in-line rheology [83], measurement of the feed-force [84]. The temperature of the print-head could also be measured during printing. This was attempted during the thesis using an infrared camera, but it was not possible to obtain useful information by only measuring on the surface of the print-head. Therefore, in-line temperature measurements could provide useful information that could be used when studying the structural integrity of the filament during printing.

### 6.2.2 Mechanical testing of 3D printed CR1

The compression cut test was used in this thesis to study the mechanical properties of 3D printed CR1. Several other mechanical testing methods have been suggested in section 1.4. However, the applicability of the compression cut test to small quantities of material definitely provides an advantage over many other tests. Recommendations for the test set-up of the compression cut test as applied here are described in appendix D.5. Additional recommendations for further testing of CR1 are listed below.

- In order to interpret the results from the compression cut test of CR1, compressive tests of bulk CR1 should be performed in order to characterise its compressive response.
- In order to study the strains that occurred during the compression cut test, direct image correlation (DIC) could be used.
- The tests should slightly be adjusted to capture failure more accurately. Instead of a blade, a cutting tool could be developed with a very well defined tip radius, such as in the work of Holt [65]. The influence of the usage of this blade on the results should be studied.

### 6.2.3 Developing CR1 towards a self-healing 3D printing filament

Several things can be changed about the polymer in order to make it more suitable for 3D printing. These changes should focus on obtaining a rheological behaviour that is more favourable for 3D printing. However, if the aim is not to lose the high toughness, the high tensile strength of the polymer, as well as its self-healing ability, the effects of these changes on those properties should not be neglected.

- Altering the properties of the bulk polymer. Since polyurethanes like CR1 provide a versatile platform for property tuning, various alterations can be made to make it more suitable for 3D printing.
  - Changing the hard segment concentration by changing the molar ratio of the components. An increase in hard segment has been related to a higher tensile modulus and lower elongation at break [85].
  - Changing the components, the diisocyanate, chain extender and polyol can be changed.
    - The effect of two other diisocyanates on the mechanical properties and self-healing ability of CR1 has already been tested [66]. There has also been work on TPU's with mixtures of diisocyanates [59].
  - Blending CR1 with another polymer. Although TPU is seldom blended with other polymers due to its inherently easily tunable system, there are applications for which TPU is blended with other polymers, such as polycarbonate (PC) [86].

# Bibliography


[1] Shafranek, R.T., Millik, S.C., Smith, P.T., Lee, C., Boydston, A.J., and Nelson, A. "Stimuli-responsive materials in additive manufacturing". In: *Progress in Polymer Science* (2019).

[2] Zhang, Z., Demir, K.G., and Gu, G.X. "Developments in 4D-printing: a review on current smart materials, technologies, and applications". In: *International Journal of Smart and Nano Materials* 10.3 (2019), pp. 205–224.

[3] ASTM. "52900-15 Standard Terminology for Additive Manufacturing—General Principles—Terminology". In: (2015).

[4] Lewis, J.A. and Gratson, G.M. "Direct writing in three dimensions". In: *Materials today* 7.7-8 (2004), pp. 32–39.

[5] Su, J., Gao, W., Trinh, K., Kenderes, S.M., Tekin Pulatsu, E., Zhang, C., Whittington, A., Lin, M., and Lin, J. "4D printing of polyurethane paint-based composites". In: *International Journal of Smart and Nano Materials* (2019), pp. 1–12.

[6] Brackett, D., Ashcroft, I., and Hague, R. "Topology optimization for additive manufacturing". In: *Proceedings of the solid freeform fabrication symposium, Austin, TX*. Vol. 1. S. 2011, pp. 348–362.

[7] Ford, S. and Despeisse, M. "Additive manufacturing and sustainability: an exploratory study of the advantages and challenges". In: *Journal of Cleaner Production* 137 (2016), pp. 1573–1587.

[8] Gibson, I., Rosen, D.W., Stucker, B., et al. *Additive manufacturing technologies*. Vol. 17. Springer, 2014.

[9] ASTM. "F2924-14, Standard Specification for Additive Manufacturing Titanium-6 Aluminum-4 Vanadium with Powder Bed Fusion". In: (2014).

[10] Agarwala, M.K., Jamalabad, V.R., Langrana, N.A., Safari, A., Whalen, P.J., and Danforth, S.C. "Structural quality of parts processed by fused deposition". In: *Rapid Prototyping Journal* 2.4 (1996), pp. 4–19.

[11] Wool, R.P. *Strength of polymer interfaces*. Tech. rep. ILLINOIS UNIV AT URBANA-CHAMPAIGN, 1990.

[12] Mohamed, O.A., Masood, S.H., and Bhowmik, J.L. "Optimization of fused deposition modeling process parameters: a review of current research and future prospects". In: *Advances in Manufacturing* 3.1 (2015), pp. 42–53.

[13] Ahn, S., Montero, M., Odell, D., Roundy, S., and Wright, P.K. "Anisotropic material properties of fused deposition modeling ABS". In: *Rapid prototyping journal* 8.4 (2002), pp. 248–257.

[14] Chin Ang, K., Fai Leong, K., Kai Chua, C., and Chandrasekaran, M. "Investigation of the mechanical properties and porosity relationships in fused deposition modelling-fabricated porous structures". In: *Rapid Prototyping Journal* 12.2 (2006), pp. 100–105.

[15] Rayegani, F. and Onwubolu, G.C. "Fused deposition modelling (FDM) process parameter prediction and optimization using group method for data handling (GMDH) and differential evolution (DE)". In: *The International Journal of Advanced Manufacturing Technology* 73.1-4 (2014), pp. 509–519.

[16] Chung Wang, C., Lin, T., and Hu, S. "Optimizing the rapid prototyping process by integrating the Taguchi method with the Gray relational analysis". In: *Rapid prototyping journal* 13.5 (2007), pp. 304–315.

[17] Masood, S.H., Mau, K., and Song, W.Q. "Tensile properties of processed FDM polycarbonate material". In: *Materials Science Forum*. Vol. 654. Trans Tech Publ. 2010, pp. 2556–2559.

[18] Rauwendaal, C. *Polymer extrusion*. Carl Hanser Verlag GmbH Co KG, 2014.

[19] Turner, B.N., Strong, R., and Gold, S.A. "A review of melt extrusion additive manufacturing processes: I. Process design and modeling". In: *Rapid Prototyping Journal* (2014).

[20] Bikas, H., Stavropoulos, P., and Chryssolouris, G. "Additive manufacturing methods and modelling approaches: a critical review". In: *The International Journal of Advanced Manufacturing Technology* 83.1-4 (2016), pp. 389–405.

[21] Bellini, A., Güçeri, S., and Bertoldi, M. "Liquefier dynamics in fused deposition". In: *J. Manuf. Sci. Eng.* 126.2 (2004), pp. 237–246.

[22] Ramanath, H.S., Chua, C.K., Leong, K.F., and Shah, K.D. "Melt flow behaviour of poly-$\varepsilon$-caprolactone in fused deposition modelling". In: *Journal of Materials Science: Materials in Medicine* 19.7 (2008), pp. 2541–2550.

[23] Armillotta, A., Bellotti, M., and Cavallaro, M. "Warpage of FDM parts: Experimental tests and analytic model". In: *Robotics and Computer-Integrated Manufacturing* 50 (2018), pp. 140–152.

[24] Mostafa, N., Syed, H.M., Igor, S., and Andrew, G. "A study of melt flow analysis of an ABS-Iron composite in fused deposition modelling process". In: *Tsinghua Science & Technology* 14 (2009), pp. 29–37.

[25] Darby, R. and Chhabra, R.P. *Chemical engineering fluid mechanics*. CRC Press, 2016.

[26] Appuhamillage, G.A., Reagan, J.C., Khorsandi, S., Davidson, J.R., Voit, W., and Smaldone, R.A. "3D printed remendable polylactic acid blends with uniform mechanical strength enabled by a dynamic Diels–Alder reaction". In: *Polymer Chemistry* 8.13 (2017), pp. 2087–2092.

[27] Hager, M.D., Greil, P., Leyens, C., van der Zwaag, S., and Schubert, U.S. "Self-healing materials". In: *Advanced Materials* 22.47 (2010), pp. 5424–5430.

[28] Garcia, S.J. "Effect of polymer architecture on the intrinsic self-healing character of polymers". In: *European Polymer Journal* 53 (2014), pp. 118–125.

[29] Dry, C.M. and Sottos, N.R. "Passive smart self-repair in polymer matrix composite materials". In: *Smart Structures and Materials 1993: Smart Materials*. Vol. 1916. International Society for Optics and Photonics. 1993, pp. 438–444.

[30] White, S.R., Sottos, N.R., Geubelle, P.H., Moore, J.S., Kessler, M.R., Sriram, S.R., Brown, E.N., and Viswanathan, S. "Autonomic healing of polymer composites". In: *Nature* 409.6822 (2001), p. 794.

[31] Bleay, S.M., Loader, C.B., Hawyes, V.J., Humberstone, L., and Curtis, P.T. "A smart repair system for polymer matrix composites". In: *Composites Part A: Applied Science and Manufacturing* 32.12 (2001), pp. 1767–1776.

[32] Toohey, K.S., Sottos, N.R., Lewis, J.A., Moore, J.S., and White, S.R. "Self-healing materials with microvascular networks". In: *Nature materials* 6.8 (2007), p. 581.

[33] Ponnusami, S.A., Krishnasamy, J., Turteltaub, S., and van der Zwaag, S. "A cohesive-zone crack healing model for self-healing materials". In: *International Journal of Solids and Structures* 134 (2018), pp. 249–263.

[34] Hansen, C.J., Wu, W., Toohey, K.S., Sottos, N.R., White, S.R., and Lewis, J.A. "Self-healing materials with interpenetrating microvascular networks". In: *Advanced Materials* 21.41 (2009), pp. 4143–4147.

[35] Wu, W., DeConinck, A., and Lewis, J.A. "Omnidirectional printing of 3D microvascular networks". In: *Advanced materials* 23.24 (2011), H178–H183.

[36] Davidson, J.R., Appuhamillage, G.A., Thompson, C.M., Voit, W., and Smaldone, R.A. "Design paradigm utilizing reversible Diels–Alder reactions to enhance the mechanical properties of 3D printed materials". In: *ACS applied materials & interfaces* 8.26 (2016), pp. 16961–16966.

[37] Yang, K., Grant, J.C., Lamey, P., Joshi-Imre, A., Lund, B.R., Smaldone, R.A., and Voit, W. "Diels-Alder reversible thermoset 3D printing: isotropic thermoset polymers via fused filament fabrication". In: *Advanced functional materials* 27.24 (2017), p. 1700318.

[38] Zhang, M., Vora, A., Han, W., Wojtecki, R.J., Maune, H., Le, A.B.A., Thompson, L.E., McClelland, G.M., Ribet, F., Engler, A.C., et al. "Dual-responsive hydrogels for direct-write 3D printing". In: *Macromolecules* 48.18 (2015), pp. 6482–6488.

[39] Nadgorny, M., Xiao, Z., and Connal, L.A. "2D and 3D-printing of self-healing gels: design and extrusion of self-rolling objects". In: *Molecular Systems Design & Engineering* 2.3 (2017), pp. 283–292.

[40] Highley, C.B., Rodell, C.B., and Burdick, J.A. "Direct 3D printing of shear-thinning hydrogels into self-healing hydrogels". In: *Advanced Materials* 27.34 (2015), pp. 5075–5079.

[41] Nadgorny, M., Collins, J., Xiao, Z., Scales, P.J., and Connal, L.A. "3D-printing of dynamic self-healing cryogels with tuneable properties". In: *Polymer Chemistry* 9.13 (2018), pp. 1684–1692.

[42] Wu, T., Gray, E., and Chen, B. "A self-healing, adaptive and conductive polymer composite ink for 3D printing of gas sensors". In: *Journal of Materials Chemistry C* 6.23 (2018), pp. 6200–6207.

[43] Kee, S., Haque, M. A., Corzo, D., Alshareef, H.N., and Baran, D. "Self-Healing and Stretchable 3D-Printed Organic Thermoelectrics". In: *Advanced Functional Materials* (2019), p. 1905426.

[44] Kuang, X., Chen, K., Dunn, C.K., Wu, J., Li, V.C.F., and Qi, H.J. "3D printing of highly stretchable, shape-memory, and self-healing elastomer toward novel 4D printing". In: *ACS applied materials & interfaces* 10.8 (2018), pp. 7381–7388.

[45] Varley, R.J. and van der Zwaag, S. "Towards an understanding of thermally activated self-healing of an ionomer system during ballistic penetration". In: *Acta Materialia* 56.19 (2008), pp. 5737–5750.

[46] García-Huete, N., Post, W., Laza, J. Manuel, Vilas, J. Luis, León, L.M., and García, S.J. "Effect of the blend ratio on the shape memory and self-healing behaviour of ionomer-polycyclooctene crosslinked polymer blends". In: *European Polymer Journal* 98 (2018), pp. 154–161.

[47] Zhao, Z., Peng, F., Cavicchi, K.A., Cakmak, M., Weiss, R.A., and Vogt, B.D. "Three-dimensional printed shape memory objects based on an olefin ionomer of zinc-neutralized poly (ethylene-co-methacrylic acid)". In: *ACS applied materials & interfaces* 9.32 (2017), pp. 27239–27249.

[48] Peng, F., Zhao, Z., Xia, X., Cakmak, M., and Vogt, B.D. "Enhanced Impact Resistance of Three-Dimensional-Printed Parts with Structured Filaments". In: *ACS applied materials & interfaces* 10.18 (2018), pp. 16087–16094.

[49] Calderón-Villajos, R., López, A.J., Peponi, L., Manzano-Santamaría, J., and Ureña, A. "3D-printed self-healing composite polymer reinforced with carbon nanotubes". In: *Materials Letters* 249 (2019), pp. 91–94.

[50] Dizon, J.R.C., Espera Jr, A.H., Chen, Q., and Advincula, R.C. "Mechanical characterization of 3D-printed polymers". In: *Additive Manufacturing* 20 (2018), pp. 44–67.

[51] Burghardt, W.R., Brown, E.F., Auad, M.L., and Kornfield, J.A. "Molecular orientation of a commercial thermotropic liquid crystalline polymer in simple shear and complex flow". In: *Rheologica acta* 44.5 (2005), pp. 446–456.

[52] ASTM. "D638-14 Standard test method for tensile properties of plastics". In: (2014).

[53] ASTM. "D412-16 Standard test methods for vulcanized rubber and thermoplastic elastomers-tension". In: (2006).

[54] ASTM. "D5528-13 Standard Test Method for Mode I Interlaminar Fracture Toughness of Unidirectional Fiber-Reinforced Polymer Matrix Composites". In: (2013).

[55] Spoerk, M., Arbeiter, F., Cajner, H., Sapkota, J., and Holzer, C. "Parametric optimization of intra-and inter-layer strengths in parts produced by extrusion-based additive manufacturing of poly (lactic acid)". In: *Journal of applied polymer science* 134.41 (2017), p. 45401.

[56] Aliheidari, N., Tripuraneni, R., Ameli, A., and Nadimpalli, S. "Fracture resistance measurement of fused deposition modeling 3D printed polymers". In: *Polymer Testing* 60 (2017), pp. 94–101.

[57] Davis, C.S., Hillgartner, K.E., Han, S.H., and Seppala, J.E. "Mechanical strength of welding zones produced by polymer extrusion additive manufacturing". In: *Additive manufacturing* 16 (2017), pp. 162–166.

[58] ASTM. "D1938-14, Standard Test Method for Tear Propagation Resistance (Trouser Tear) of Plastic Film and Thin Sheeting by a Single-Tear Method". In: (2014).

[59] Prisacariu, C. *Polyurethane elastomers: from morphology to mechanical aspects*. Springer Science & Business Media, 2011.

[60] Sivakova, S., Bohnsack, D.A., Mackay, M.E., Suwanmala, P., and Rowan, S.J. "Utilization of a combination of weak hydrogen-bonding interactions and phase segregation to yield highly thermosensitive supramolecular polymers". In: *Journal of the American Chemical Society* 127.51 (2005), pp. 18202–18211.

[61] Yang, Y., Davydovich, D., Hornat, C.C., Liu, X., and Urban, M.W. "Leaf-inspired self-healing polymers". In: *Chem* 4.8 (2018), pp. 1928–1936.

[62] Ratner, B.D., Hoffman, A.S., Schoen, F.J., and Lemons, J.E. *Biomaterials science: an introduction to materials in medicine*. Elsevier, 2004.

[63] Lapprand, A., Boisson, F., Delolme, F., Méchin, F., and Pascault, J. "Reactivity of isocyanates with urethanes: Conditions for allophanate formation". In: *Polymer degradation and stability* 90.2 (2005), pp. 363–373.

[64] Lin, S.B., Hwang, K.S., Tsay, S.Y., and Cooper, S.L. "Segmental orientation studies of polyether polyurethane block copolymers with different hard segment lengths and distributions". In: *Colloid and Polymer Science* 263.2 (1985), pp. 128–140.

[65] Holt, W.L. "Compression cutting test for rubber". In: *Bureau of Standards Journal of Research* 12 (1934), pp. 489–499.

[66] Garcia, S.J., Malucelli, G., and Senardi, M. "The correlation between interfacial healing and microstructure in highly branched and hydrogen-bonded segmented polyurethanes". In: (2019).

[67] Xie, F., Zhang, T., Bryant, P., Kurusingal, V., Colwell, J.M., and Laycock, B. "Degradation and stabilization of polyurethane elastomers". In: *Progress in Polymer Science* (2019).

[68] Herrera, M., Matuschek, G., and Kettrup, A. "Thermal degradation of thermoplastic polyurethane elastomers (TPU) based on MDI". In: *Polymer degradation and stability* 78.2 (2002), pp. 323–331.

[69] Trovati, G., Sanches, E.A., Neto, S.C., Mascarenhas, Y.P., and Chierice, G.O. "Characterization of polyurethane resins by FTIR, TGA, and XRD". In: *Journal of Applied Polymer Science* 115.1 (2010), pp. 263–268.

[70] Chang, W.L. "Decomposition behavior of polyurethanes via mathematical simulation". In: *Journal of Applied Polymer Science* 53.13 (1994), pp. 1759–1769.

[71] Scott, G. "Initiation processes in polymer degradation". In: *Polymer degradation and stability* 48.3 (1995), pp. 315–324.

[72] Szycher, M. *Szycher's handbook of polyurethanes*. CRC press, 1999.

[73] Lee, H.S., Wang, Y.K., and Hsu, S.L. "Spectroscopic analysis of phase separation behavior of model polyurethanes". In: *Macromolecules* 20.9 (1987), pp. 2089–2095.

[74] H.S., Barbara. *Infrared Spectroscopy: Fundamentals and Applications*. J. Wiley & Sons, 2004.

[75] Li, Y., Gao, T., and Chu, B. "Synchrotron SAXS studies of the phase-separation kinetics in a segmented polyurethane". In: *Macromolecules* 25.6 (1992), pp. 1737–1742.

[76] Leung, L.M. and Koberstein, J.T. "Small-angle scattering analysis of hard-microdomain structure and microphase mixing in polyurethane elastomers". In: *Journal of Polymer Science: Polymer Physics Edition* 23.9 (1985), pp. 1883–1913.

[77] Chen, C.H.Y., Briber, R.M., Thomas, E.L., Xu, M., and MacKnight, W.J. "Structure and morphology of segmented polyurethanes: 2. Influence of reactant incompatibility". In: *Polymer* 24.10 (1983), pp. 1333–1340.

[78] Menard, K.P. *Dynamic Mechanical Analysis*. Boca Raton: CRC Press, 2008.

[79] Crawford, D.M., Bass, R.G., and Haas, T.W. "Strain effects on thermal transitions and mechanical properties of thermoplastic polyurethane elastomers". In: *Thermochimica acta* 323.1-2 (1998), pp. 53–63.

[80] Yanagihara, Y., Osaka, N., Iimori, S., Murayama, S., and Saito, H. "Relationship between modulus and structure of annealed thermoplastic polyurethane". In: *Materials Today Communications* 2 (2015), e9–e15.

[81] Vallance, M.A., Castles, J.L., and Cooper, S.L. "Microstructure of as-polymerized thermoplastic polyurethane elastomers". In: *Polymer* 25.12 (1984), pp. 1734–1746.

[82] Yi, J., Boyce, M.C., Lee, G.F., and Balizer, E. "Large deformation rate-dependent stress–strain behavior of polyurea and polyurethanes". In: *Polymer* 47.1 (2006), pp. 319–329.

[83] Coogan, T.J. and Kazmer, D.O. "In-line rheological monitoring of fused deposition modeling". In: *Journal of Rheology* 63.1 (2019), pp. 141–155.

[84] Serdeczny, M.P., Comminal, R., Pedersen, D.B., and Spangenberg, J. "Experimental and analytical study of the polymer melt flow through the hot-end in material extrusion additive manufacturing". In: *Additive Manufacturing* 32 (2020), p. 100997.

[85] Eceiza, A., Martin, M.D., De La Caba, K., Kortaberria, G., Gabilondo, N., Corcuera, M.A., and Mondragon, I. "Thermoplastic polyurethane elastomers based on polycarbonate diols with different soft segment molecular weight and chemical structure: mechanical and thermal properties". In: *Polymer Engineering & Science* 48.2 (2008), pp. 297–306.

[86] Utracki, L.A. and Wilkie, C.A. *Polymer blends handbook*. Vol. 1. Springer, 2002.

[87] Van Vliet, T. *Rheology and fracture mechanics of foods*. CRC Press, 2013.

[88] Goh, S.M., Charalambides, M.N., and Williams, J.G. "On the mechanics of wire cutting of cheese". In: *Engineering fracture mechanics* 72.6 (2005), pp. 931–946.

# Appendix A

# Fourier transform infrared spectroscopy results

FTIR is a fast and straightforward method to study the chemical bonds present in a polymer. Since the polymer was processed thermally and mechanically twice during the thesis, FTIR was used to gain an initial impression of the samples before the ATR image was made. In this chapter, the FTIR results are be presented. Appendix A.1 contains the FTIR spectra of the batches of CR1, appendix A.2 presents the FTIR spectrum of the filament compared to that of the bulk CR1 and appendix A.3 contains the FTIR spectra of each of the CR1 prints.

## A.1 CR1 quality check of the synthesised batches.

CR1 was synthesised in numerous batches and FTIR was used to make a quality check of the batches. Figure A.1 shows the normalised FTIR results of the batches of CR1 and a sample synthesised by Croda. The spectra show homogeneity throughout the spectrum and therefore the synthesis of the CR1 batches could be considered successful.

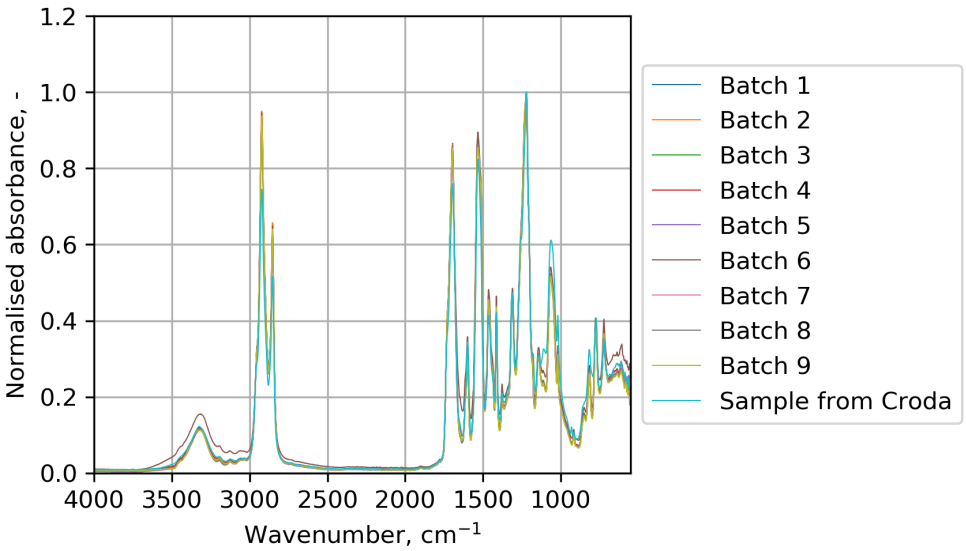


**Figure A.1:** FTIR analysis of the synthesised batches and a sample from Croda.

## A.2 Filament

Figure A.2 shows the FTIR results of the filament compared to the bulk polymer (CR1_1 from figure A.1). There is no significant difference in the spectra for bulk and filament. This suggested that there had been no significant degradation that altered the chemical structure, and that there was no blending with polymer that had previously been processed by the filament maker.

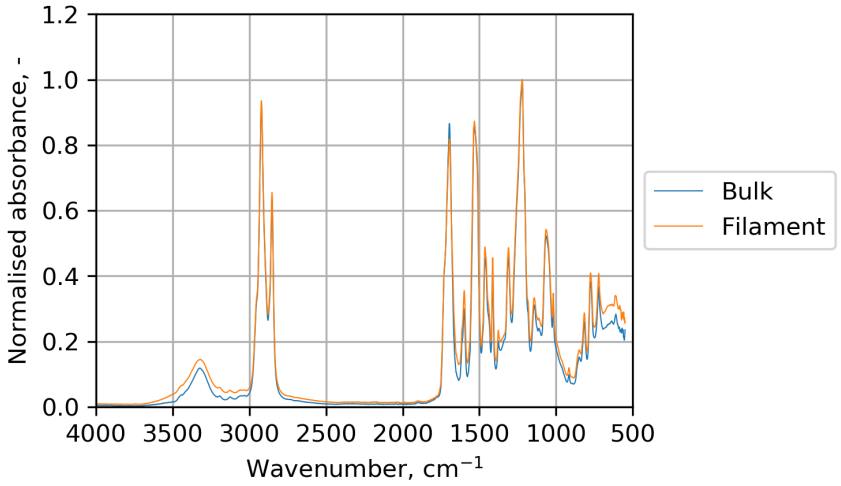


**Figure A.2:** FTIR analyses of the bulk polymer and the filament.

## A.3 Prints

Figure A.3 shows the FTIR spectra of the 3D printed parts, and of the filament. There was a good homogeneity across the spectra, with the exception of the amide I peak at 1700 $cm^{-1}$. The print CR1_230_5 has an additional peak at 1647 $cm^{-1}$. This peak was also seen in the ATR spectrum of the domains of this print and is further discussed in section 5.4.1.

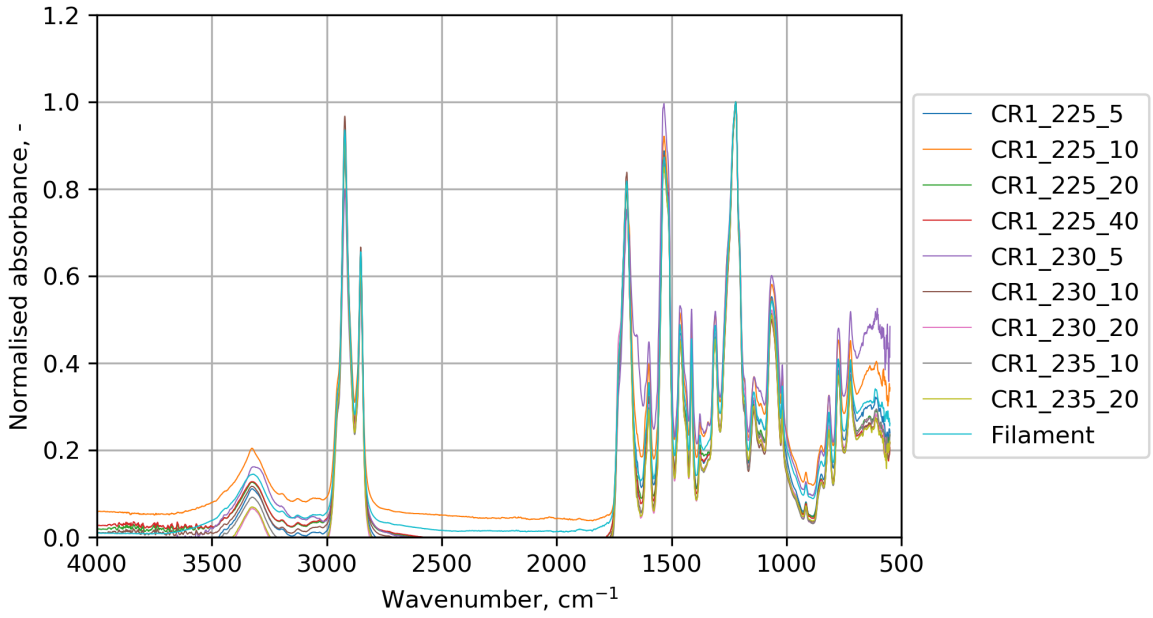


**Figure A.3:** FTIR analyses of the 3D printed CR1 and the CR1 filament.

# Appendix B

# Slicer settings

| **Speed** | | |
|---|---|---|
| Print speed | $V_{print}$ | mm/s |
| Infill speed | $V_{print}$ | mm/s |
| Wall speed | $V_{print}$ | mm/s |
| Outer wall speed | $V_{print}$ | mm/s |
| Inner wall speed | $V_{print}$ | mm/s |
| Travel speed | 80 | mm/s |
| Initial layer speed | $V_{print}$ | mm/s |
| Initial layer travel speed | 80 | mm/s |
| Number of slower layers | 0 | |
| Equilize filament flow | no | |
| Enable filament flow | no | |
| Enable acceleration control | no | |
| Enable jerk control | no | |
| **Travel** | | |
| Combing mode | all | |
| Max comb distance with no retract | 100 | mm |
| Retract before outer wall | no | |
| Avoid printed parts when travelling | yes | |
| Travel avoid distance | 0.625 | mm |
| Layer start X | 0 | mm |
| layer start Y | 0 | mm |

| **Cooling** | | |
|---|---|---|
| Enable print cooling | yes | |
| Fan speed | 100 | % |
| Regular fan speed | 100 | % |
| Maximum fan speed | 100 | % |
| Regular/maximum fan speed threshold | 10 | s |
| Initial fan speed | 100 | % |
| Regular fan speed at height | 0 | mm |
| Regular fan speed at layer | 1 | |
| Minimum layer time | 0 | s |
| Minimum speed | 0 | mm/s |
| Lift head | no | |
| **Support** | | |
| Generate support | no | |
| **Build plate adhesion** | | |
| Build plate adhesion type | none | |

| **Quality** | | |
|---|---|---|
| Layer height | 0.4 | mm |
| Initial layer height | 0.4 | mm |
| Line width | 0.8 | mm |
| Wall line width | 0.8 | mm |
| Outer wall line width | 0.8 | mm |
| Inner wall(s) line width | 0.8 | mm |
| Initial layer line width | 100 | % |
| **Shell** | | |
| Wall thickness | 0 | mm |
| Wall line count | 0 | |
| Outer wall wipe distance | 0 | mm |
| Top/bottom thickness | 0 | mm |
| Top thickness | 0 | mm |
| Top layers | 0 | |
| Bottom thickness | 0 | mm |
| Bottom layers | 0 | |
| Outer wall inset | 0 | mm |
| Optimise wall printing order | no | |
| Outer before inner walls | no | |
| Alternate extra wall | no | |
| Compensate wall overlaps | no | |
| Compensate outer wall overlaps | no | |
| Compensate inner wall overlaps | no | |
| Minimum wall flow | 0 | % |
| Fill gaps between walls | nowhere | |
| Filter out tiny gaps | yes | |
| Print thin walls | no | |
| Horizontal expansion | 0 | mm |
| Initial layer horizontal expansion | 0 | mm |
| Z seam alignment | sharpest corner | |
| Seam corner preference | hide seam | |
| Enable ironing | no | |

| **Infill** | | |
|---|---|---|
| Infill density | 100 | % |
| Infill line distance | $d_{infill}$ | mm |
| Infill pattern | zig zag | |
| Infill line directions | [90] | |
| Infill X offset | 0 | mm |
| Infill Y offset | 0 | mm |
| Extra infill wall count | 0 | |
| Infill overlap percentage | 0 | % |
| Infill overlap | 0 | mm |
| Infill wipe distance | 0 | mm |
| Infill layer thickness | 0.4 | mm |
| Gradual infill steps | no | |
| Infill before walls | no | |
| Minimum infill area | 0 | mm2 |
| Infill support | no | |
| **Material** | | |
| Printing temperature | $T_{print}$ | °C |
| Printing temperature layer | $T_{print}$ | °C |
| Initial printing temperature | $T_{print}$ | °C |
| Final printing temperature | $T_{print}$ | °C |
| Build plate temperature | 30 | °C |
| Build plate temperature initial layer | 30 | °C |
| Flow | 100 | % |
| Prime tower flow | 100 | % |
| Initial layer flow | 100 | % |
| Enable retraction | no | |
| Retract at layer change | no | |

# Appendix C

# Characterisation of CR1 samples

In chapter 5, the 3D printing of CR1 at various print-speeds and print-head temperatures was reported. Out of these samples, three were selected for mechanical testing. The quality of the other samples was also assessed, and is presented in this chapter. Appendix C.1 contains microscopic pictures of the cross-sections and sides of the 3D printed samples. Appendix C.2 contains the results of the ATR analyses of the prints.

## C.1 Microscopic pictures

Microscopic pictures were taken of the cross-sections of the 3D printed CR1 samples. Figure C.1 shows the microscopic pictures of the samples printed at 225 °C. Figure C.2 shows those of the samples printed at 230 °C and figure C.3 those of the samples printed at 235 °C. Table C.1 summarises the properties of the cross-sections of the 3D printed samples. The 3D printed samples were always taller than 4 mm, with the exception of the sample printed at 225 °C and 10 mm/s. This suggested that the polymer had swollen during the printing. Overall, the CR1_230_20 was considered to be the most regular sample. The sample had the cross-section with the fewest voids, the fewest visible boundaries and the side of the sample was the most regular. CR1_225_40 also had a comparatively regular side, but only 4 layers were printed under these conditions.

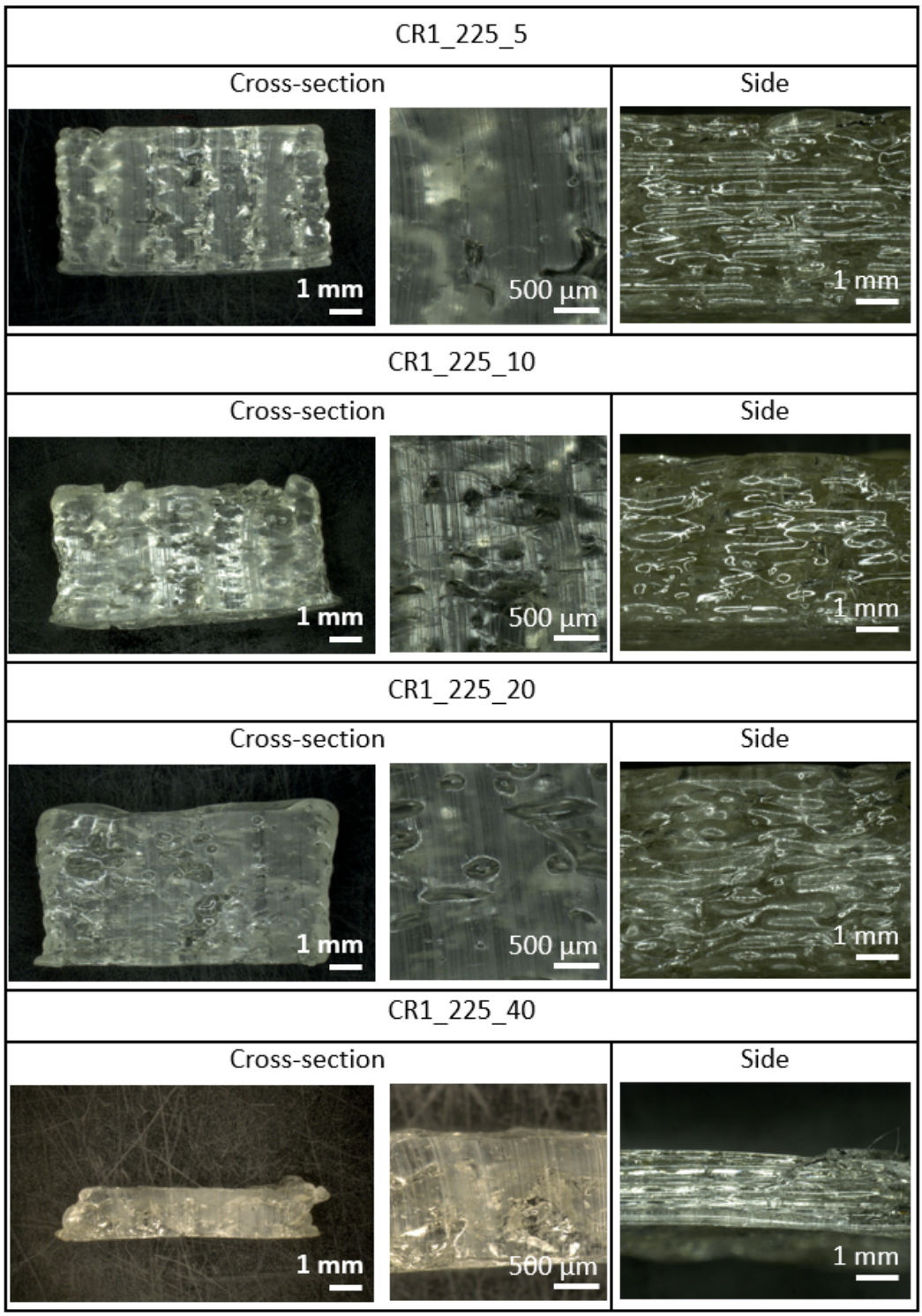


**Figure C.1:** Microscopic pictures of the samples printed at 225 °C: the cross-section (left), a close-up of the cross-section (middle) and the side (right)

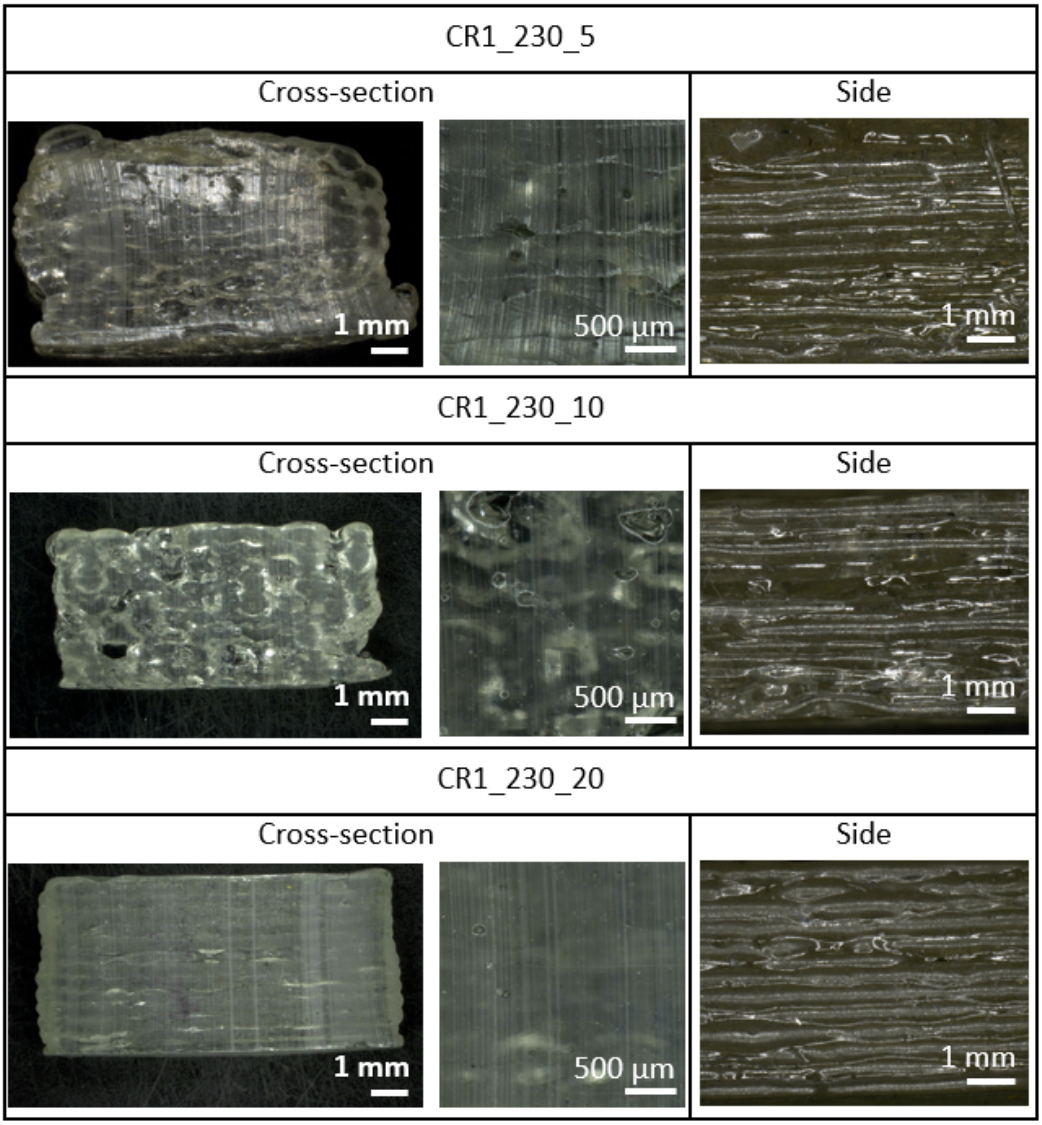


**Figure C.2:** Microscopic pictures of the samples printed at 230 °C: the cross-section (left), a close-up of the cross-section (middle) and the side (right)

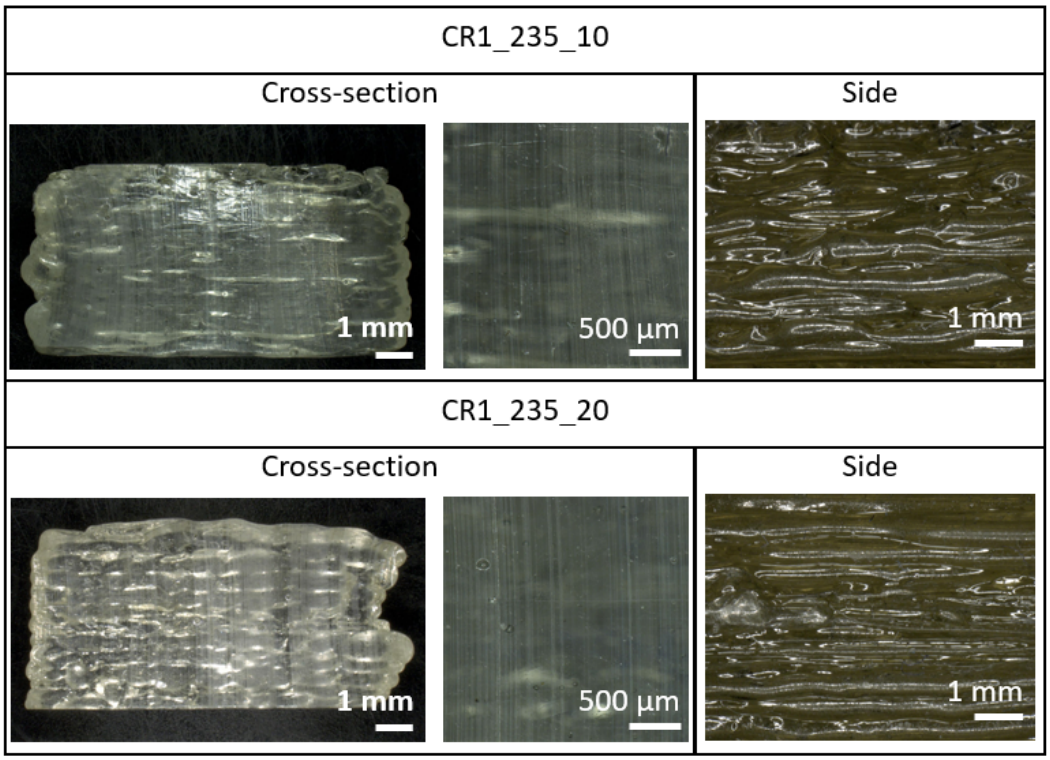


**Figure C.3:** Microscopic pictures of the samples printed at 235 °C: the cross-section (left), a close-up of the cross-section (middle) and the side (right)

**Table C.1:** Analysis of the microscopic pictures of the cross-sections of 3D printed CR1.

| Sample | width, mm | height, mm | Void content | Filament shape |
|---|---|---|---|---|
| CR1_225_5 | 8.2 | 4.5 | ++ | Visible, oval |
| CR1_225_10 | 8.1 - 8.7 | 4 | + | Visible, rhombus-like |
| CR1_225_20 | 9 | 4.3 | + | Not visible |
| CR1_240_40 | 8 | 1.5 | / | Not visible |
| CR1_230_5 | 9.1-10 | 4.5-6 | - | Visible, rhombus-like |
| CR1_230_10 | 8.5-9 | 4.5 | ++ | Visible, oval |
| CR1_230_20 | 9.2 - 9.6 | 4.7 | - - | Invisible |
| CR1_235_10 | 10 | 5 | - - | Invisible |
| CR1_235_20 | 9.3-10 | 4.8 | - - | Invisible |

## C.2 ATR imaging

Figure C.4 shows the results of ATR-imaging of the 3D printed CR1 at different printing conditions. Table C.2 summarises the analyses of 350 $\mu$m by 350 $\mu$m regions at the centre of the ATR images. Overall, the size and amount of the domains tended to increase with increasing printing temperature and increasing print-speed.

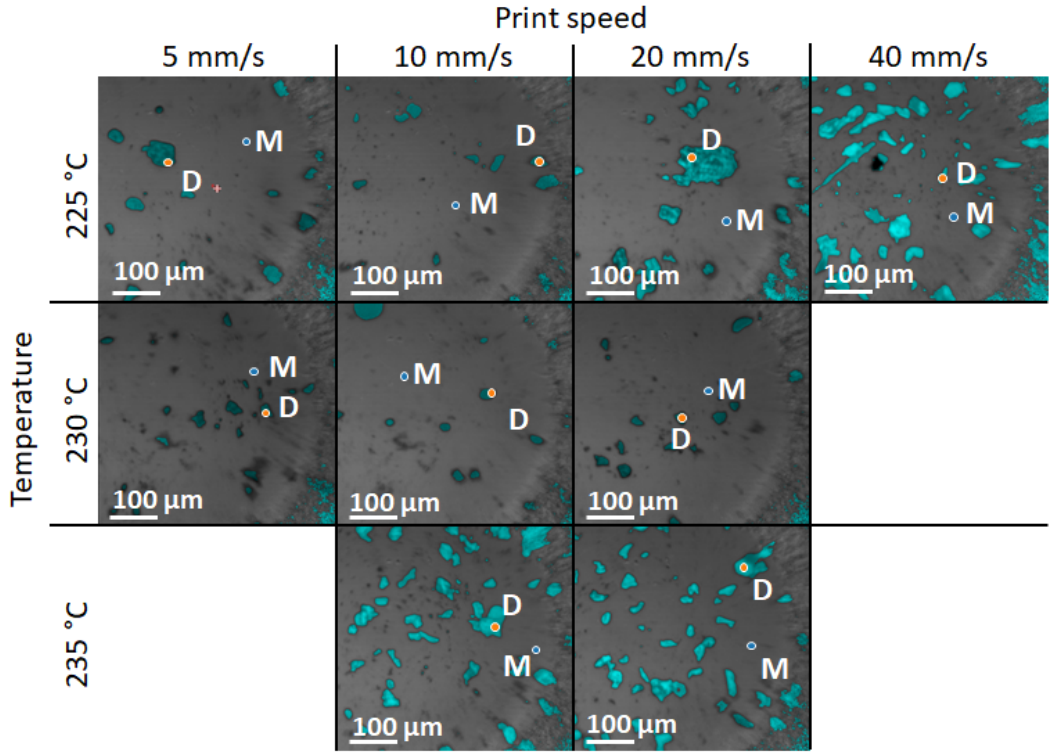


**Figure C.4:** ATR images of the 3D printed CR1 samples.

Comparing the FTIR spectra of the domains and the matrix of the prints in figure C.5, most of the spectra of the prints showed good overlap with those of the bulk. In some cases, a peak was observed at 2350 $cm^{-1}$. This peak emerged in the domains of CR1_225_20, CR1_225_40 and CR1_235_10, indicating the presence of carbon dioxide [68]. The presence of this peak could be attributed to carbon dioxide in the air. The peak at 3325 $cm^{-1}$ tended to shift to a lower wavelength in the spectra of the prints, indicating more hydrogen bonding in these prints. The print CR1_225_5 had an additional peak at 1854 $cm^{-1}$.

**Table C.2:** Analysis of the ATR images of untreated CR1, filament made of CR1 and 3D printed CR1.

| | Domains area % | Average domain size $\mu m^2$ | Number of domains - |
|---|---|---|---|
| CR1 bulk | 10.04 | 592 | 20 |
| CR1 filament | 10.01 | 592 | 19 |
| CR1_225_5 | 3.48 | 515 | 8 |
| CR1_225_10 | 1.89 | 213 | 10 |
| CR1_225_20 | 9.95 | 1305 | 9 |
| CR1_225_40 | 14.84 | 463 | 38 |
| CR1_230_5 | 2.47 | 183 | 16 |
| CR1_230_10 | 1.50 | 250 | 7 |
| CR1_230_20 | 3.23 | 310 | 12 |
| CR1_235_10 | 12.69 | 488 | 30 |
| CR1_235_20 | 12.06 | 485 | 29 |

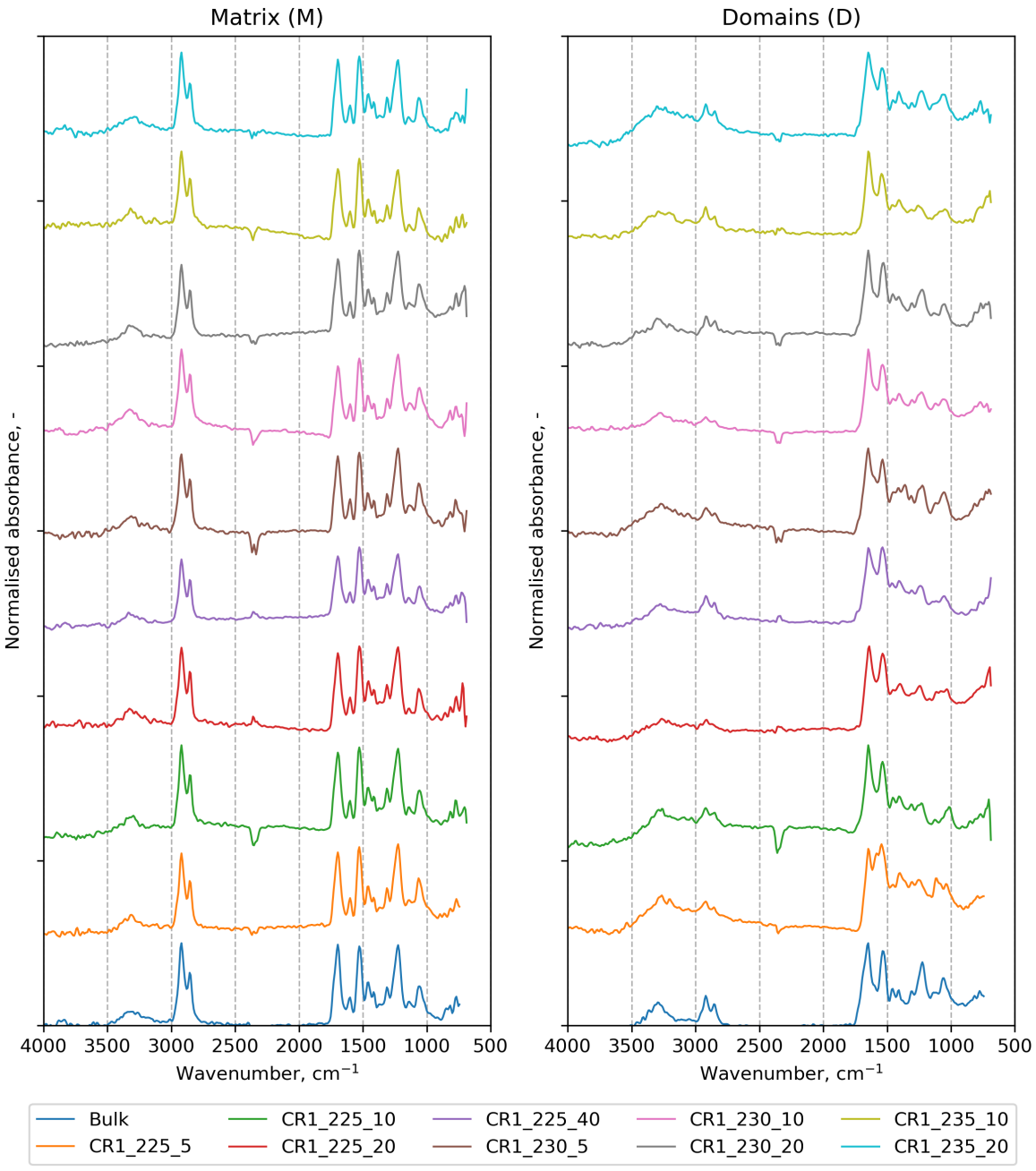


**Figure C.5:** ATR spectra of CR1 prints.

# Appendix D

# Trials of compression cut testing for 3D printed elastomers

In order to establish and verify the testing method of compression cutting for the 3D printed parts, several trials were conducted. To assess the tests ability to quantify the anisotropy of 3D printed parts, four different prints in Ninjaflex were tested. This chapter shows the results of these trials with Ninjaflex. Appendix D.1 provides some background information about the compression cut test and how it has been applied in the past. In appendix D.2, the test matrix for the trails was established. Appendix D.3 displays the results of the trials, which are discussed in appendix D.4. Finally, appendix D.5 presents some final remarks about the compression cut test used in this set-up.

## D.1 Background

Compression cut tests had already been reported on in literature. According to the work of Holt et al. [65], the compression cut test should show a phase of compression of the sample by the blade, followed by an abrupt failure when the blade cuts through the sample. The result of the test would be the force at which this abrupt failure occurs. However, based on the geometry of the blade that significantly differed from that used in the work of Holt et al., a different response were also to be expected. A similar test was also used to study the fracture mechanics of food [87]. In these tests, the force-displacement curve may be separated into three parts. The first part consisting of a linear compression response, followed by the second part: the initial cutting of the material. After this, cutting occurs at a constant force, and the fracture energy could be calculated by dividing this force by the width of the specimen. The test demonstrated by Holt[65] would be an example of a cut test applied to relatively stiff elastomers with a significant compression followed by abrupt failure. The test developed for food would be applicable to relatively soft materials with a small compression of the material underneath the blade, followed by cutting and more gradual failure. The response of the porous and flexible prints might lie anywhere between these two.

## D.2 Establishing the test matrix

There are various print settings that can be changed to improve the interlayer adhesion of 3D printed parts, such as layer orientation, print-bed temperature, print-head temperature and air-gap [12]. Within this work, two of them were considered that could easily be controlled and compared with the chosen test: the print-head temperature and the air-gap. Increasing the temperature of the print-head during printing should result in stronger interlayer adhesion [56, 55]. Additionally, reducing the distance between two deposited rows of polymer should result in a stronger interlayer adhesion, due to the increased contact area between two layers [56, 55]. Hence, one variable (temperature) influences the interlayer adhesion between deposited filaments, whereas the other (air-gap, reduced by reducing the infill distance) influences the interlayer adhesion of the print as a whole, due to an increased contact area. A higher print-head temperature combined with a smaller infill distance should yield the 'best' results.

The tensile strength of Ninjaflex in the direction parallel to the stacking of the layers was found to be 35% of that of Ninjaflex tested in the same direction as the deposited filaments [37]. This meant that there should also be a significant difference in the results of the compression cut test comparing the XZ direction to the YZ direction. Moreover, the initial compression of the sample prior to cutting could provide useful insights into the properties of the polymer since an anisotropy in the Young's modulus of Ninjaflex had also been reported, although anisotropy was less pronounced than that of the tensile strength (75%) [37].

4 combinations were established, shown in the test matrix in table D.1. The NF_225_0.8 sample was expected to show the worst performance, and the NF_235_0.5 sample should perform the best in terms of anisotropy, and of mechanical properties in general.

**Table D.1:** Test matrix of the trails of the compression cut test with Ninjaflex.

| | | **Temperature, °C** | |
|---|---|---|---|
| | | **225** | **235** |
| **Infill distance, mm** | **0.8** | NF_225_0.8 | NF_235_0.8 |
| | **0.5** | NF_225_0.5 | NF_235_0.5 |

Cutting through the XZ-plane, shown in figure 2.6a, was expected to yield the strongest result, since in this direction the resistance against the cutting depends primarily on the properties of the material itself. The other extreme is cutting through the XY-plane, shown in figure 2.6b. In this case, the blade cut in-between the layers as they were stacked. This direction was expected to have the lowest resistance against cutting, at least in the case of a regular thermoplastic material. The time between the deposition of the layers was expected to result in poor interlayer diffusion and therefore in a region that was weaker than the bulk polymer. It was expected that a self-healing polymer with the ability to form physical cross-links in-between the layers of a print at relatively low temperatures should have a lower anisotropy when the XY-plane and the XZ-plane were compared.

## D.3 Results

### D.3.1 Microscopic pictures

Prior to testing, microscopic pictures of the samples were taken of their cross sections and sides, which can be seen in figure D.1 - D.4.

- NF_225_0.8 (figure D.1) has the most and largest air-gaps, with some rows not touching their neighbours at all in the cross-section. There were some inhomogeneities on closer to the edge of the specimen, although the profile of the sample was mostly homogeneous.
- The cross section of NF_225_0.5 (figure D.2) shows barely any air-gaps. However, the relatively large overlap between rows of the print resulted in an overflow of material at the sides of the specimen. Moreover, towards the higher layers of the print, it results in errors that can be seen in the cross section as well as on the side.
- The air-gaps in NF_235_08 (figure D.3) grew smaller as the height of the print increased, along with an increase in the width of the sample. This was also visible on the side.
- A similar phenomenon could be seen in NF_235_05 (figure D.4), although less extreme. Between some rows, the air-gaps never fully closed, although the pattern of this sample was more regular than that of NF_235_08 and NF_225_0.5, which could also be seen on the side.

Overall, in terms of air-gaps, NF_225_0.8 had the most area of air-gaps, and NF_225_0.5 had the least. In terms of shape of the sample, NF_225_0.8 and NF_235_05 had the most regular shape, while the shape of NF_235_05 was the least regular.

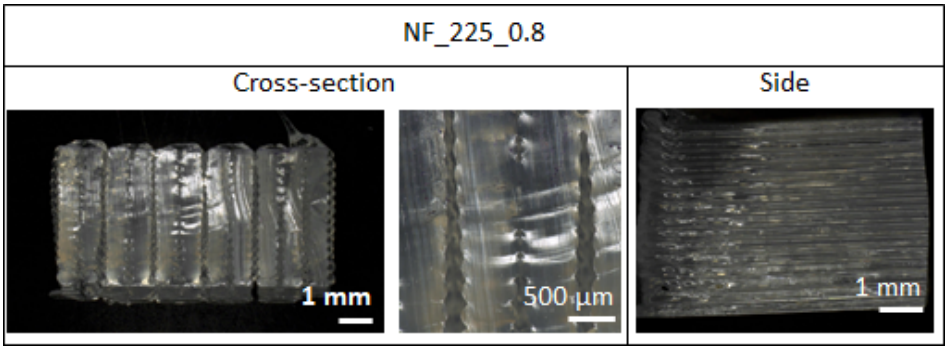


**Figure D.1:** Microscopic pictures of the Ninjaflex sample printed at 225 °C and 0.8 mm infill distance: the cross-section (left), a close-up of the cross-section (middle) and the side (right).

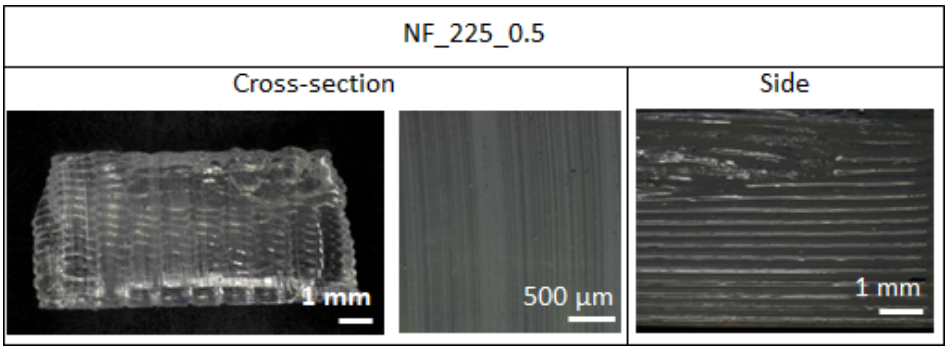


**Figure D.2:** Microscopic pictures of the Ninjaflex sample printed at 225 °C and 0.5 mm infill distance: the cross-section (left), a close-up of the cross-section (middle) and the side (right).

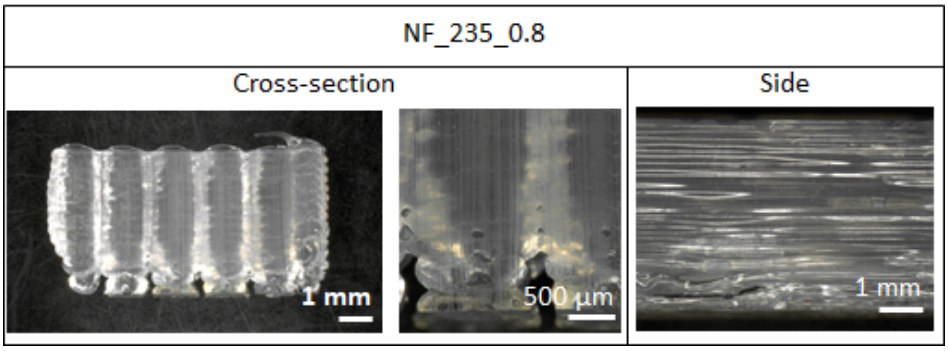


**Figure D.3:** Microscopic pictures of the Ninjaflex sample printed at 235 °C and 0.8 mm infill distance: the cross-section (left), a close-up of the cross-section (middle) and the side (right).

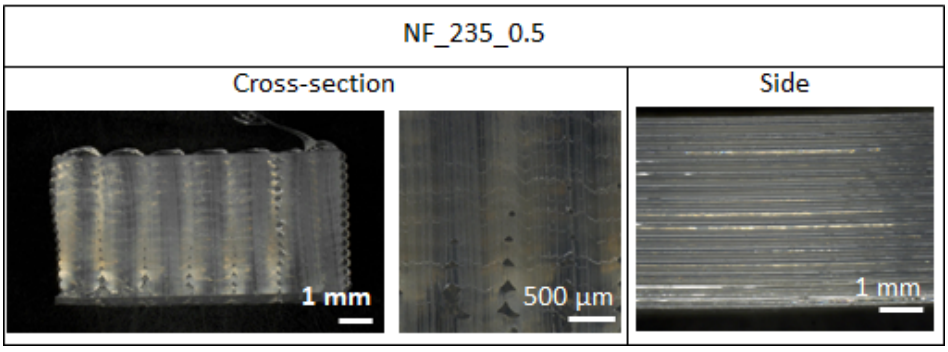


**Figure D.4:** Microscopic pictures of the Ninjaflex sample printed at 235 °C and 0.5 mm infill distance: the cross-section (left), a close-up of the cross-section (middle) and the side (right).

### D.3.2 Mechanical response

Once the samples had been analysed visually, they were tested using the compression cut test. The results of these tests can be seen in figure D.5. Clearly, the results did not resemble the results that were expected based on the work of Holt et al. [65]. However, comparing the results of the different samples, the following observations could be made.

- Initially, all samples showed a region of near-linear compression. At a certain amount of deformation, the curves started to deviate from this near-linear region.
- Upon this deviation, the force tended to stabilise.
- For the prints NF_225_0.8, NF_225_0.5 and NF_235_0.8, there was no significant or consistent difference between the curves of XZ and YZ samples.
- For the prints NF_225_0.8, NF_225_0.5 and NF_235_0.8, the initial compression of the XZ and YZ samples did not show a significant difference.
- For the prints NF_225_0.8, NF_225_0.5 and NF_235_0.8, the initial, near-linear part of the curve showed good reproducibility between samples, but the following part showed a poor reproducibility.
- For the NF_235_0.5 print, there was a significant difference between XZ- and YZ-response of both the near-linear part of the curves and the second part of the curves. Moreover, the curves showed a better reproducibility than those of the NF_225_0.8, NF_225_0.5 and NF_235_0.8 prints.

Next, the results could be quantified. Figure D.6 summarises the force at which the first peak in the force-displacement curve occurred. The average values of the XZ results and the YZ results were taken. It would be expected that the force of the XZ direction would be higher than that of the YZ direction.

- **NF_225_0.8**: YZ force was higher than the XZ force. Moreover, the force of its YZ direction was in fact higher than that of the NF_225_0.5 and NF_235_0.8 samples.
- **NF_225_0.5**: on average, the YZ force was 83% of the XZ force.
- **NF_235_0.8**: on average, the YZ force was 70% of the XZ force. The forces were also slightly lower than those of the NF_225_0.5 sample. Specifically, the XZ_1 sample showed a relatively high failure force.
- **NF_235_0.5**: on average, the YZ force was 81% of the XZ force. Compared to the other prints, the results of this print were the most replicable and the force-displacement curves showed the most resemblance to the original compression cut test.
- When constant cutting could be seen, in any sample but NF_235_0.5, there were 'bumps' in these responses, possibly caused by the layer-by-layer geometry of the prints. Comparing the constant forces, no significant between this force could be identified between the XZ and YZ directions of the samples. This suggested that the fracture energy in these directions was also not different.

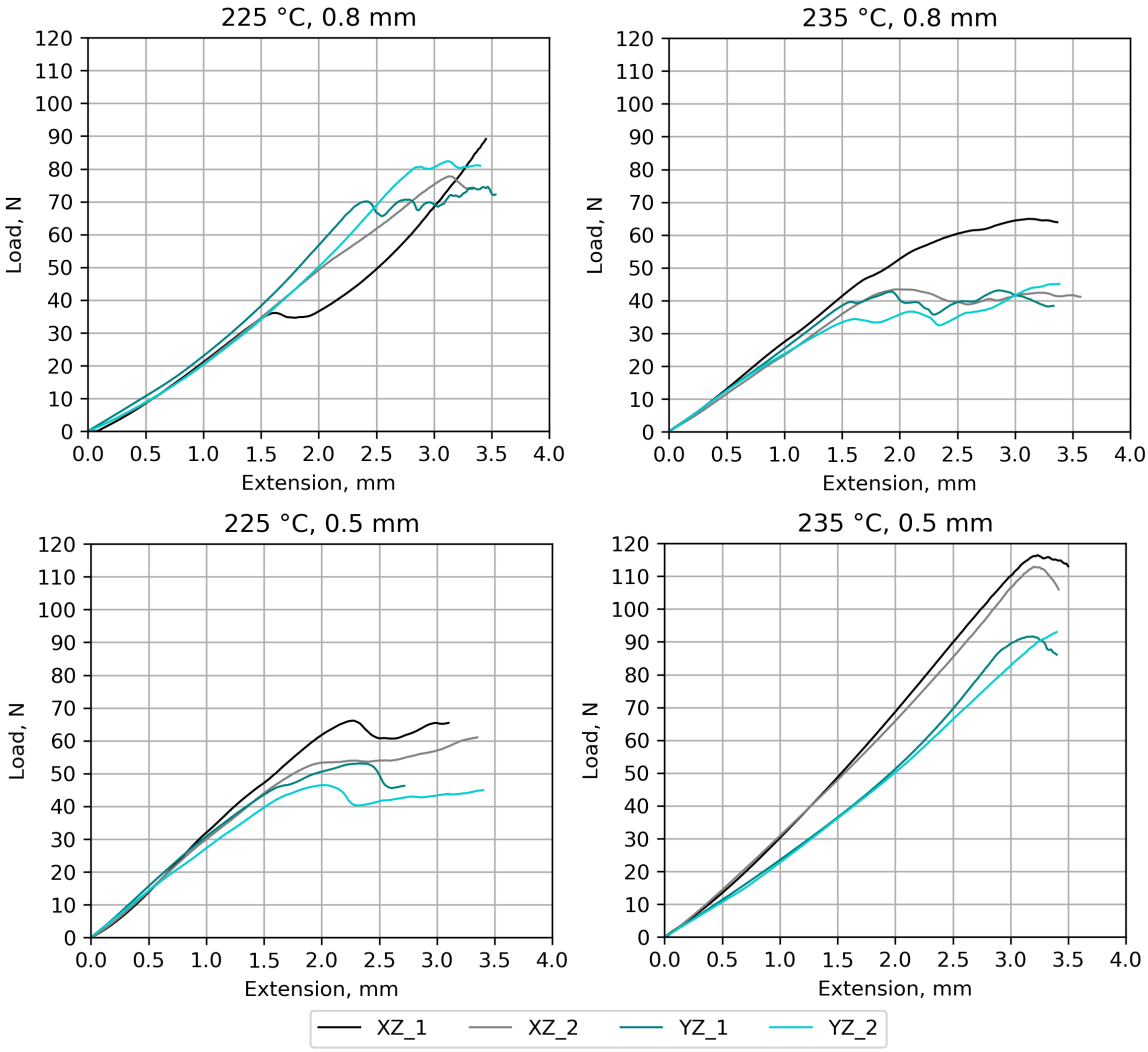


**Figure D.5:** Force-displacement curves of the compression cut test trials.

### D.3.3 Captured images during the test

In order to contextualise the results displayed in figure D.5, the microscopic images made during the test were also analysed. Stills from the captures made during the testing of each sample can be seen in figure D.7 - D.10. Microscopic pictures of the samples after the cut-test can be seen in figure D.11 - D.14. Combining these sets of images, several generic observations were made.

- During the test, there was an initial compression of the sample in its entirety. This was followed by the compression of the region surrounding the blade tip, while the edges of the specimens would tend to crowd away in tension.

- Once cutting occurred, the compressed and cut material on the sides of the blades tended to relax.

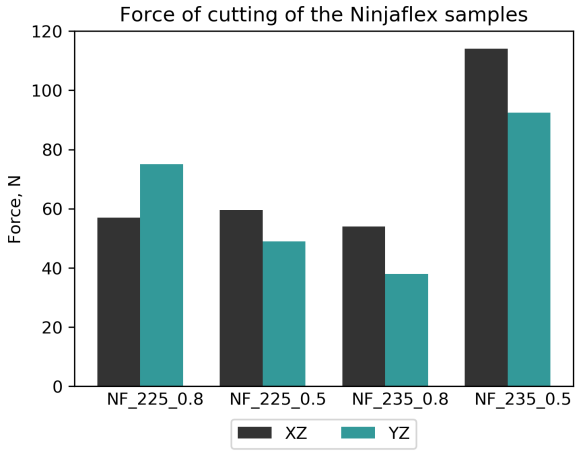


**Figure D.6:** Force of cutting of the 3D printed Ninjaflex samples.

- Asymmetric geometry caused a skewed propagation of the cuts.
  - In the XZ samples, this could mainly be seen in the angles of the sides, which resulted in an asymmetric deformation during the deformation and cutting during the test. For instance in the samples NF_235_0.8_XZ_1, NF_235_0.8_XZ_2.
  - In the YZ samples, the effect of irregular outline of the samples could also be seen in the NF_225_0.5_YZ_1 sample.
  - The higher porosity at the bottom of some of the samples caused a asymmetric deformation around the blade during the deformation and cutting during the test. This was especially prevalent in the samples with the 0.8 mm infill spacing. Figure D.11 and figure D.13 also show that the cut propagated through the filaments, instead of between the pores of the same layer.

## D.4 Discussion

In this section, the results of each print will be discussed. Overall, the samples showed a behaviour that was somewhere in-between the elastomers measured by Holt [65] and foods as measured by the wedge fracture test [87]. The cutting through the sample was gradual rather than abrupt, but there was still a large amount of deformation in the samples, due to the elastomeric nature of the material. In the NF_235_05 sample, this stage could not be reached with the current set-up.

### D.4.1 NF_225_0.8

This was the sample with the highest porosity, both in the amount and size of the air-gaps. Some rows of printed filament did not even touch one another towards the top and the bottom of the print. This resulted in significant issues during the test. The force-displacement curves of these samples were irregular, and the force of first failure of the YZ samples was on average

in fact higher than that of the average of the XZ samples. This was attributed to the early failure of the XZ_1 sample seen in figure D.5. Studying the microscopic pictures in figure D.11 stills of these tests in figure D.7, a possible explanation for these different forces could be the relatively poor quality of the samples. Specifically the YZ results could be related to the gaps between the filaments at the top and the bottom of the prints. Once loaded, these gaps would open (seen in figure D.7), reducing the stresses along the top of the sample and resulting in a higher failure force.

### D.4.2 NF_225_0.5

There was no significant difference in the mechanical response of the XZ samples and the YZ samples of the NF_225_0.5 print. In the initial, linear region of the force-displacement curve, the responses were similar. The generic shape of the results was also similar, although there was no clear distinction between the different directions, even though the deformations of the were regular with the exception of the YZ_2 sample. The sides of the print were irregular while the top wasn't, perhaps skewing the results of the YZ samples. In the end, a slight difference between the response of the YZ samples and the XZ samples could be quantified.

### D.4.3 NF_235_0.8

Similar to the NF_225_0.8 sample, the irregular geometry of the sample resulted in an irregular mechanical response. Studying the stills, in appendix D.3.3, the displacement of the sample during the testing was irregular. The resulting cut in figure D.5 was also tiled at an angle of almost 45°. The deformation and cut of the YZ_ sample were also irregular (appendix D.3.3 and figure D.13). Comparing the XZ_2 sample to the YZ_1 sample, there was no significant difference between the force of the peak.

### D.4.4 NF_235_0.5

Overall, this print appeared to have the highest quality and yield the highest quality result. This was based on the shapes of the samples, the regularity of their geometry and their force displacement curves. There was a clear difference between the responses of the XZ samples and those of the YZ samples in three aspects. First, the initial, linear compression of the sample was different. This might be due to the shape of the air-gaps in the print, which have a larger width compared to the height. Secondly, there was a difference in the force of first failure, which was higher for the XZ prints. The difference between the failure forces was the largest out of all the samples.

## D.5 Final remarks

Based on all of the observations presented in appendix D.3, it could be concluded that the compression cut test could not be used as a reliable tool to quantify the anisotropy of 3D printed parts made out of Ninjaflex. Only in the case of the print that was expected to have the highest quality, (235 °C and 0.5 mm infill distance), could any meaningful distinction be made

between the XZ samples and the YZ samples. For the other samples, there was no significant difference between the XZ samples and the YZ samples, and not even a significant difference between prints. Studying the cross-sections of these tests, as well as their deformation during testing, revealed that the results of these samples were to a large extent caused by flaws in the print, or high void concentrations.

Comparing the force-displacement curves and the resulting values to those of previously reported similar tests [65, 87, 88], it was concluded that the responses lied somewhere in-between those of the elastomers tested by Holt, and food. The print-settings had a significant influence on the response, where anisotropy could be seen only in the samples of the highest quality.

Based on these results, it was concluded that the test could be used to study some properties of some types of prints. The properties that could be compared were the compression behaviour at small displacements, as well as the performance of the print under a cutting force. The applicability would depend highly on the quality of the samples. Since the results of the 225 °C, 0.5 mm and the 235 °C, 0.8 mm samples were inconclusive, it appeared that only at prints of relatively high quality the test could yield useful results.

All in all, the compression cut test as demonstrated here should be used for qualitative comparison and as a comparative performance test. Due to the complex interplay of stresses and strains occurring during the test, it was not possible to make any meaningful statement about what was being measured. Ultimately, one would want to distinguish between the response of the material and the response resulting from the geometry of the print. Comparing the results of samples with a 0.5 mm infill distance to those of samples with a 0.8 mm infill distance already revealed that sample geometry would significantly impact the response. Nevertheless, the aim of the thesis was not to develop a testing method for small quantities 3D printed elastomers. Instead, these results were used to inform the testing of CR1-samples, and how their results should be interpreted.

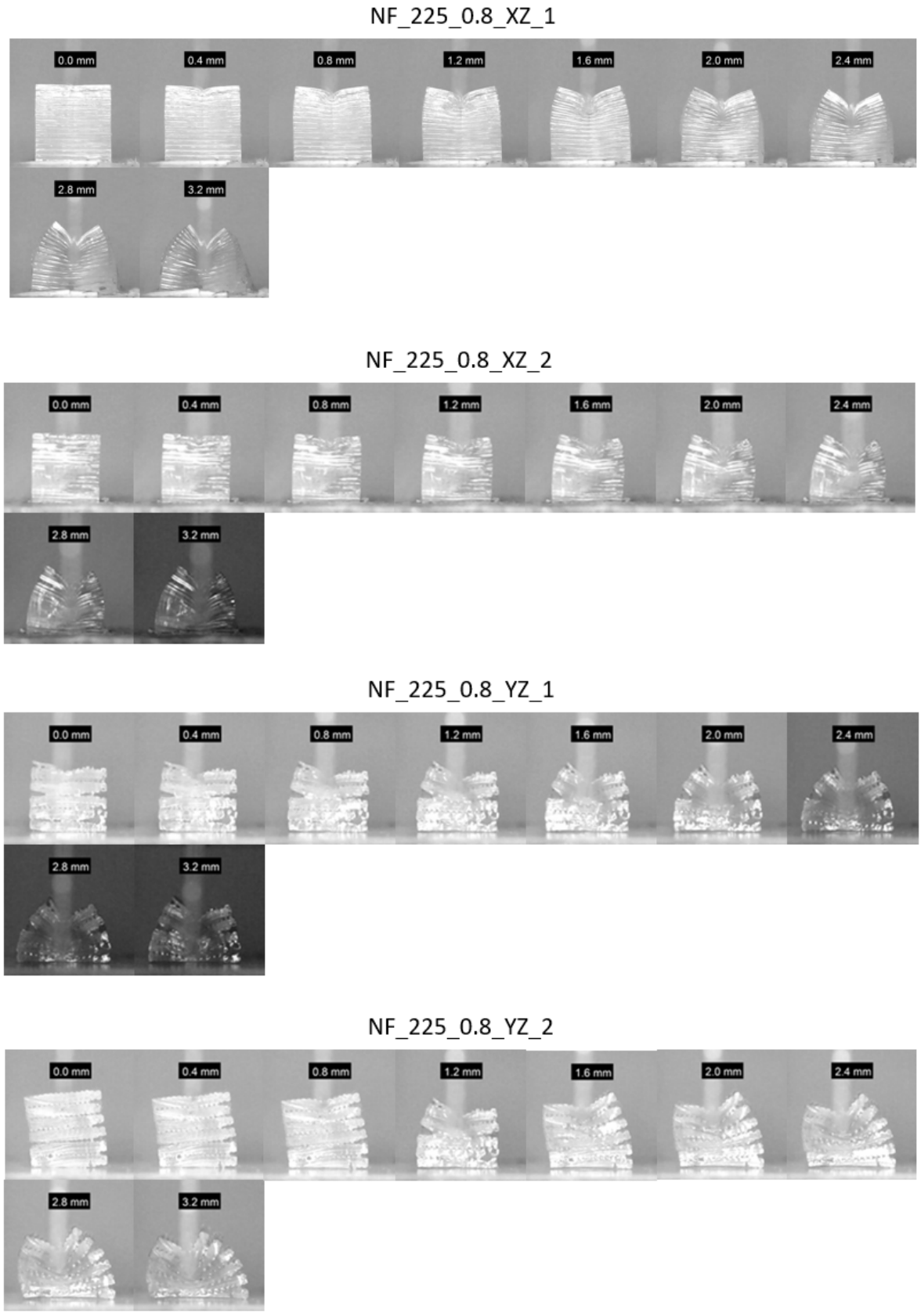


**Figure D.7:** Stills of compression cut test of the Ninjaflex samples printed at 225 °C with a 0.8 mm infill distance.

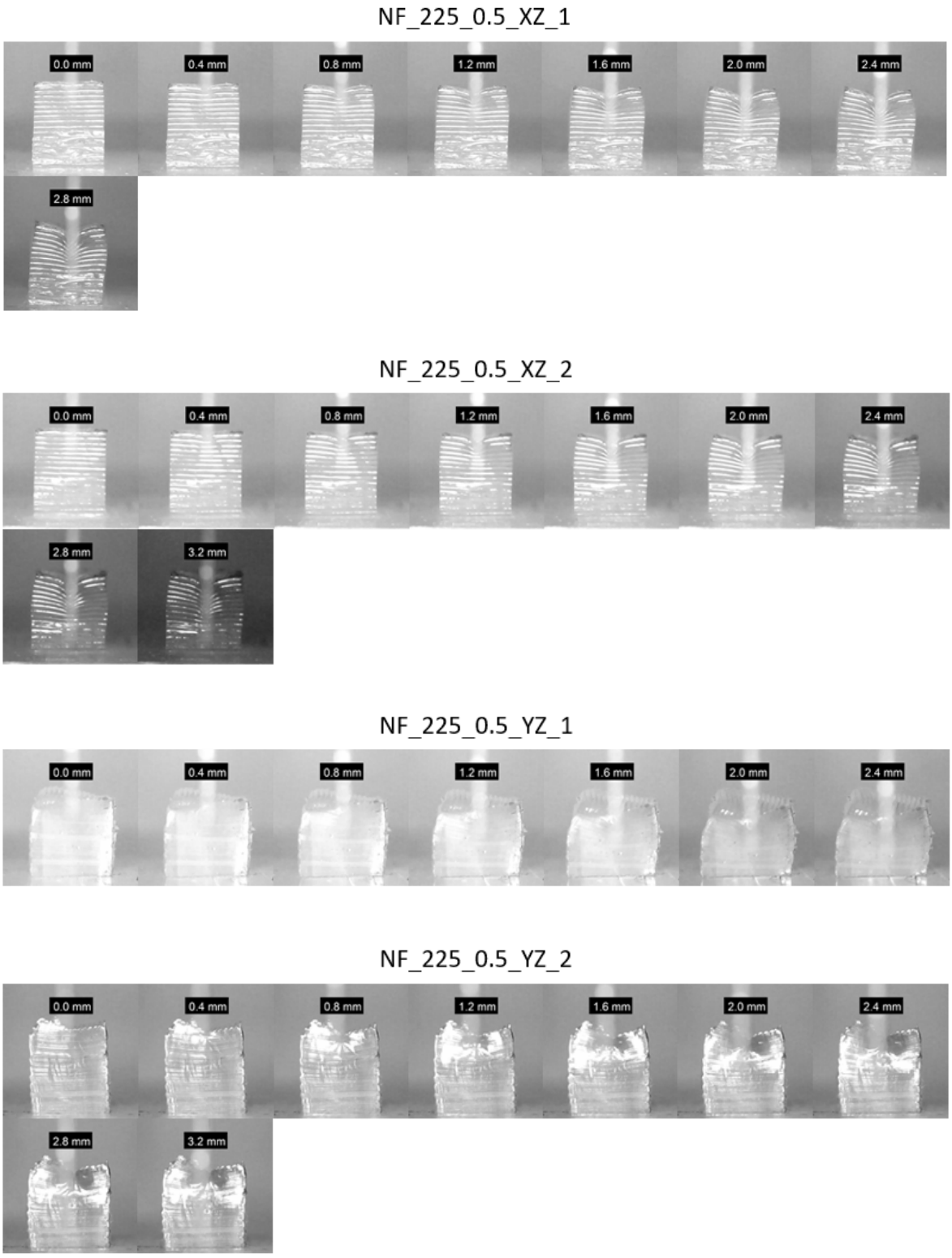


**Figure D.8:** Stills of compression cut test of the Ninjaflex samples printed at 225 °C with a 0.5 mm infill distance.

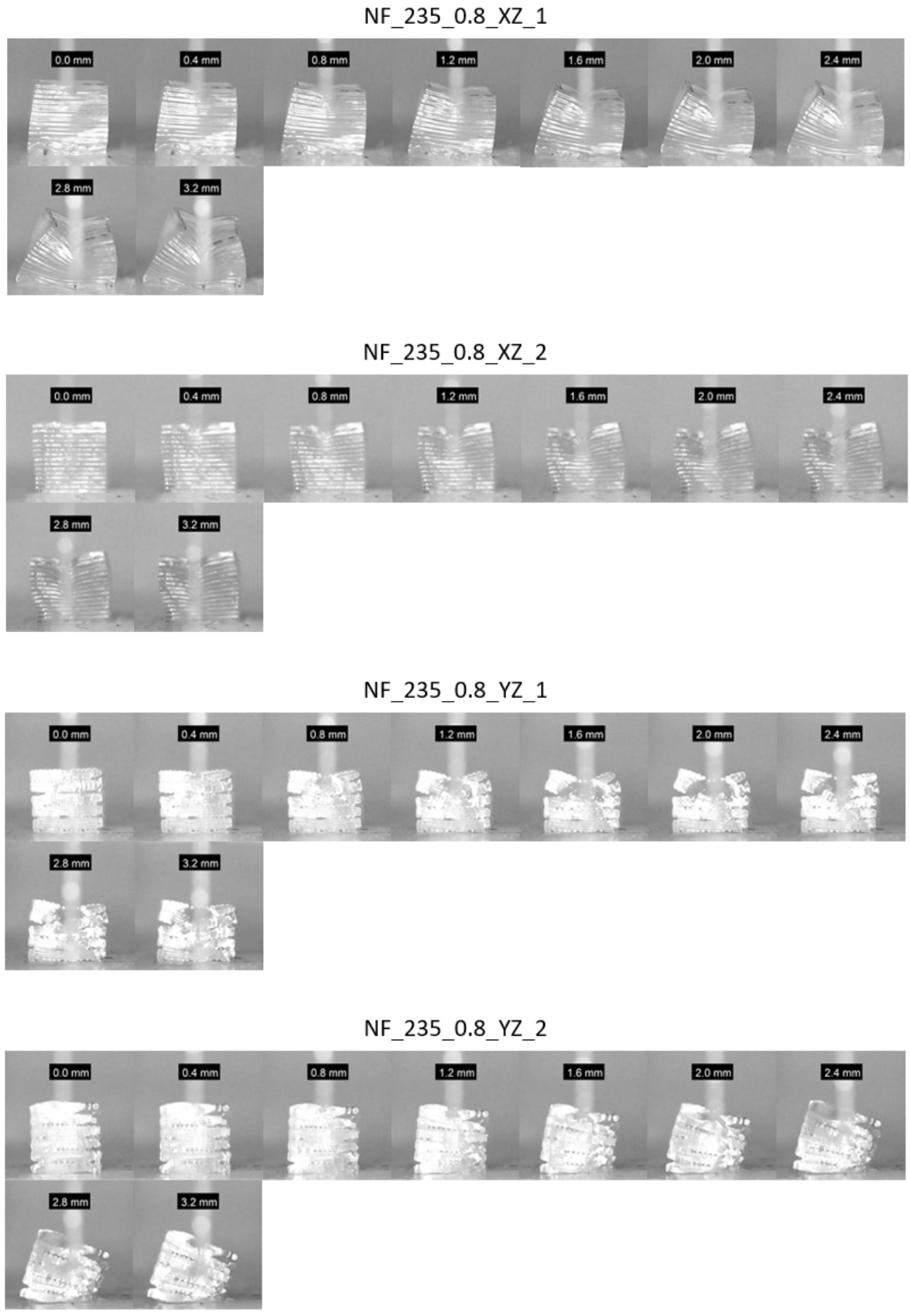


**Figure D.9:** Stills of compression cut test of the Ninjaflex samples printed at 235 °C with a 0.8 mm infill distance.

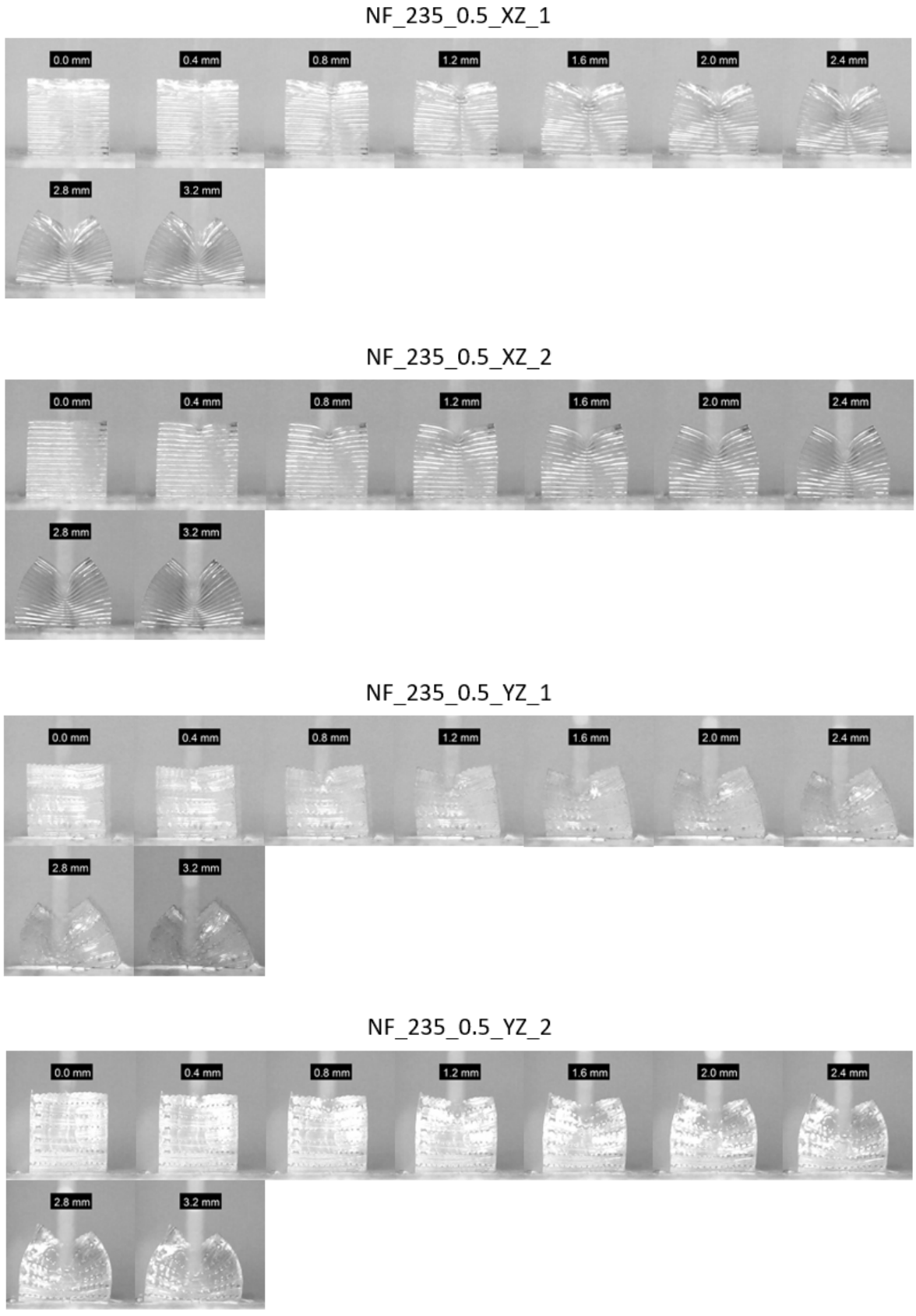


**Figure D.10:** Stills of compression cut test of the Ninjaflex samples printed at 235 °C with a 0.85 mm infill distance.

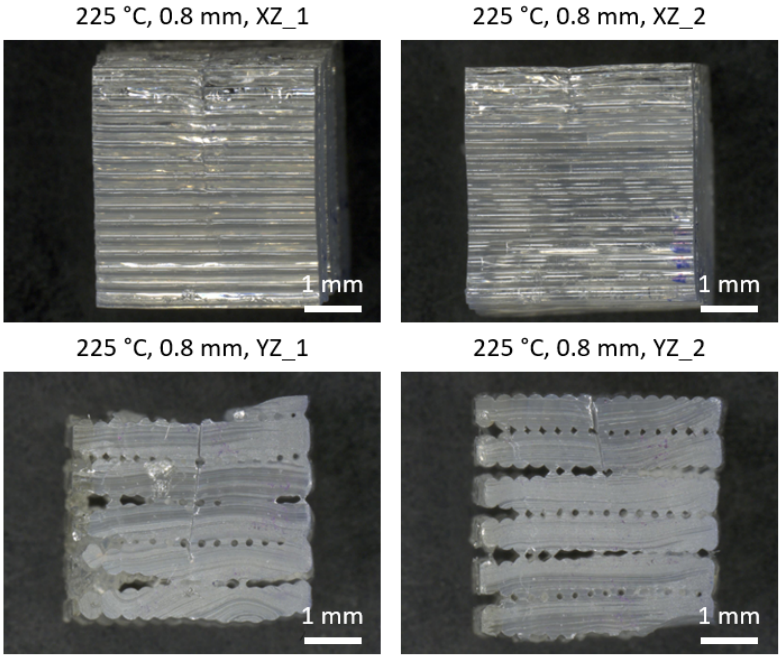


**Figure D.11:** Microscopic pictures of the NF_225_0.8 samples after cutting.

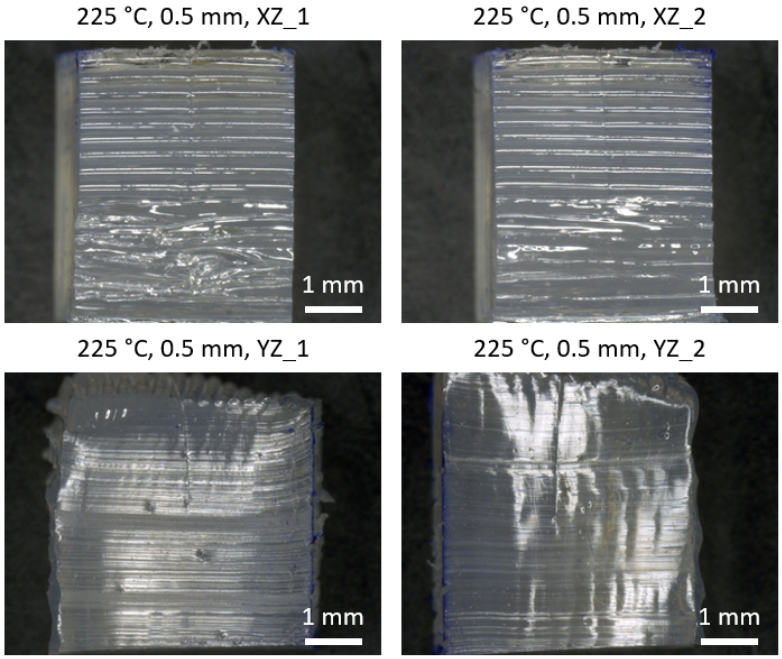


**Figure D.12:** Microscopic pictures of the NF_225_0.5 samples after cutting.

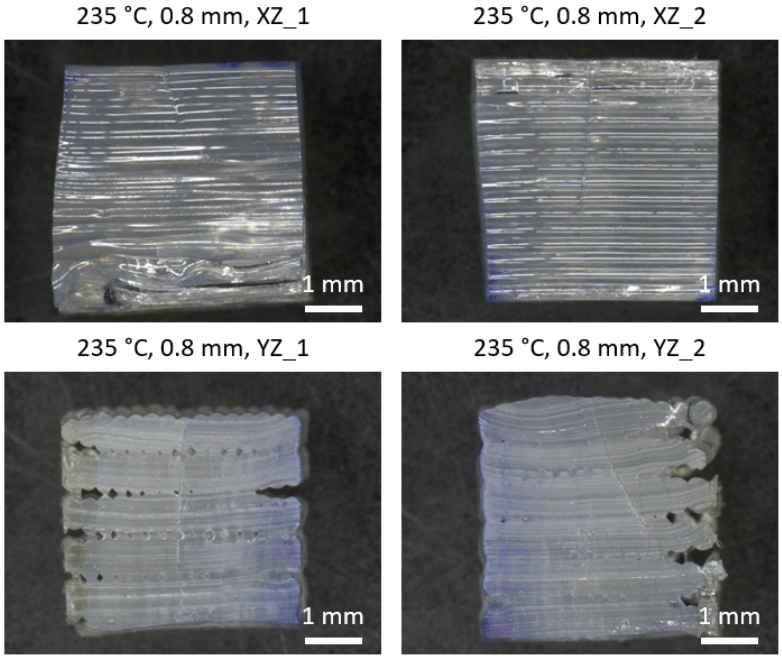


**Figure D.13:** Microscopic pictures of the NF_235_0.8 samples after cutting.

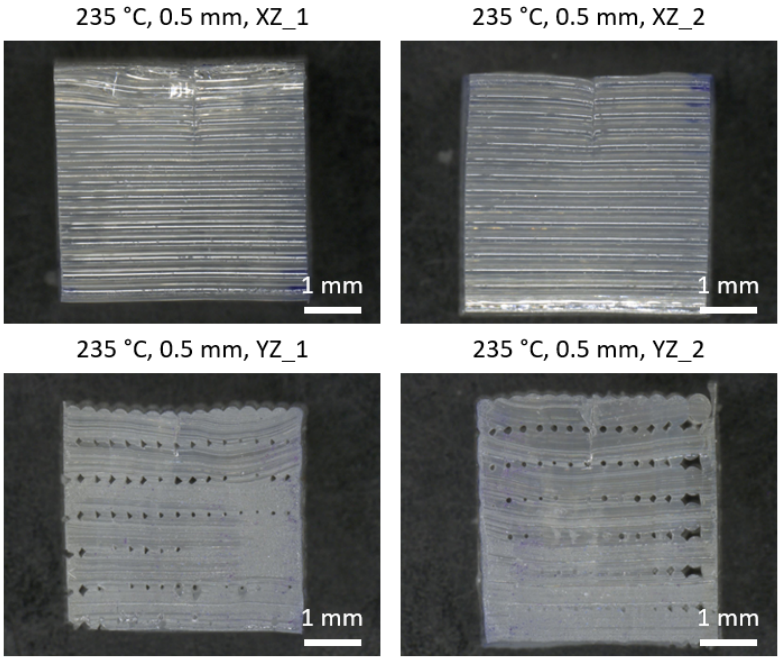


**Figure D.14:** Microscopic pictures of the NF_235_0.5 samples after cutting.

# Appendix E

# Microscopic pictures and stills of the compression cut test

This chapter presents the additional images of the compression cut test in section 5.5. Figure E.1 and E.2 show the images captured during the compression cut test of bulk CR1. Figure E.3 and E.4 show the images captured during the compression cut test of 3D printed CR1. Figure E.5 shows the images captured during the compression cut test of 3D printed Ninjaflex during the second cut. The stills of the first cut care shown in figure D.10. Figure E.5-E.8 show microscopic pictures of the tested samples of bulk CR1, 3D printed CR1 and Ninjaflex respectively.

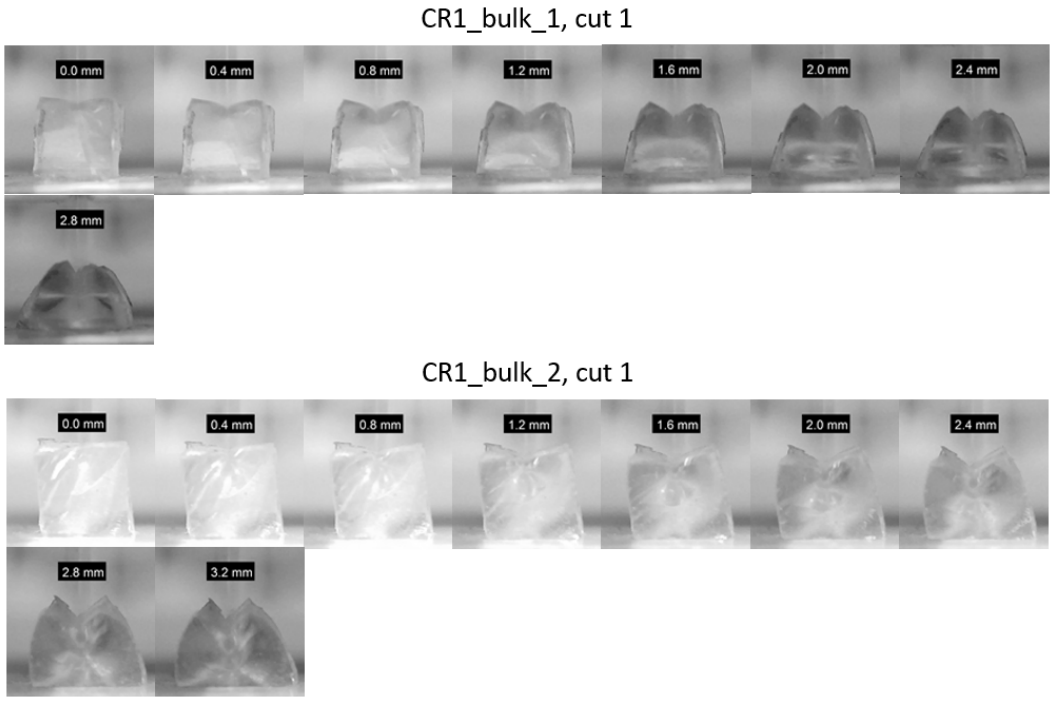


**Figure E.1:** Stills of the first cut test or the bulk CR1.

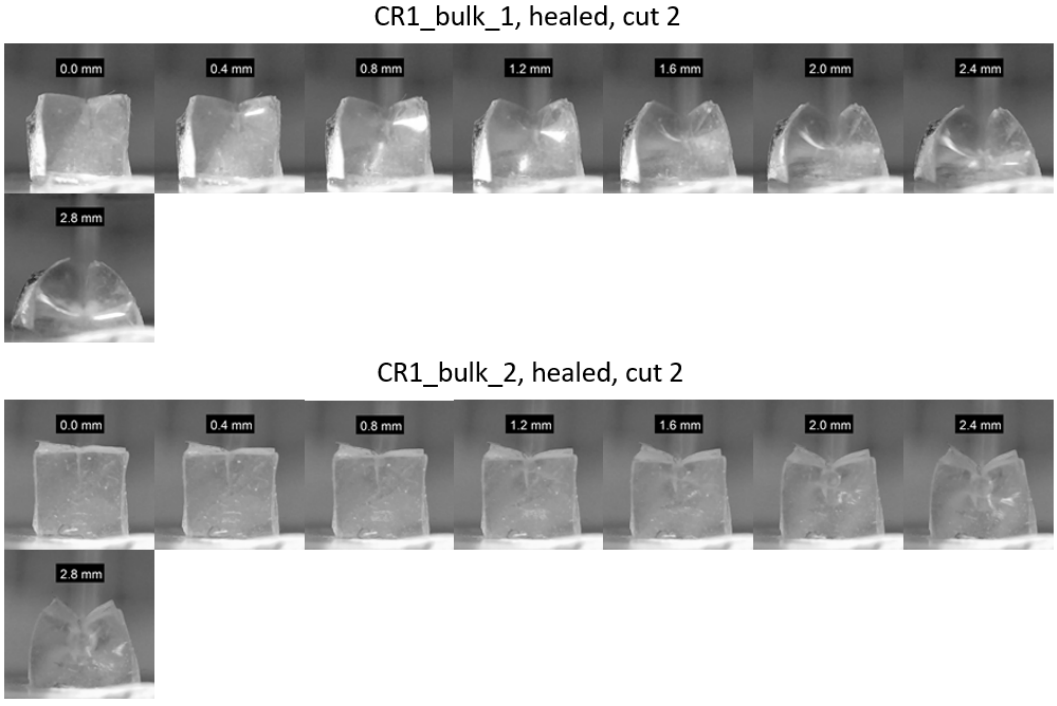


**Figure E.2:** Stills of the cut test or the bulk CR1 after healing.

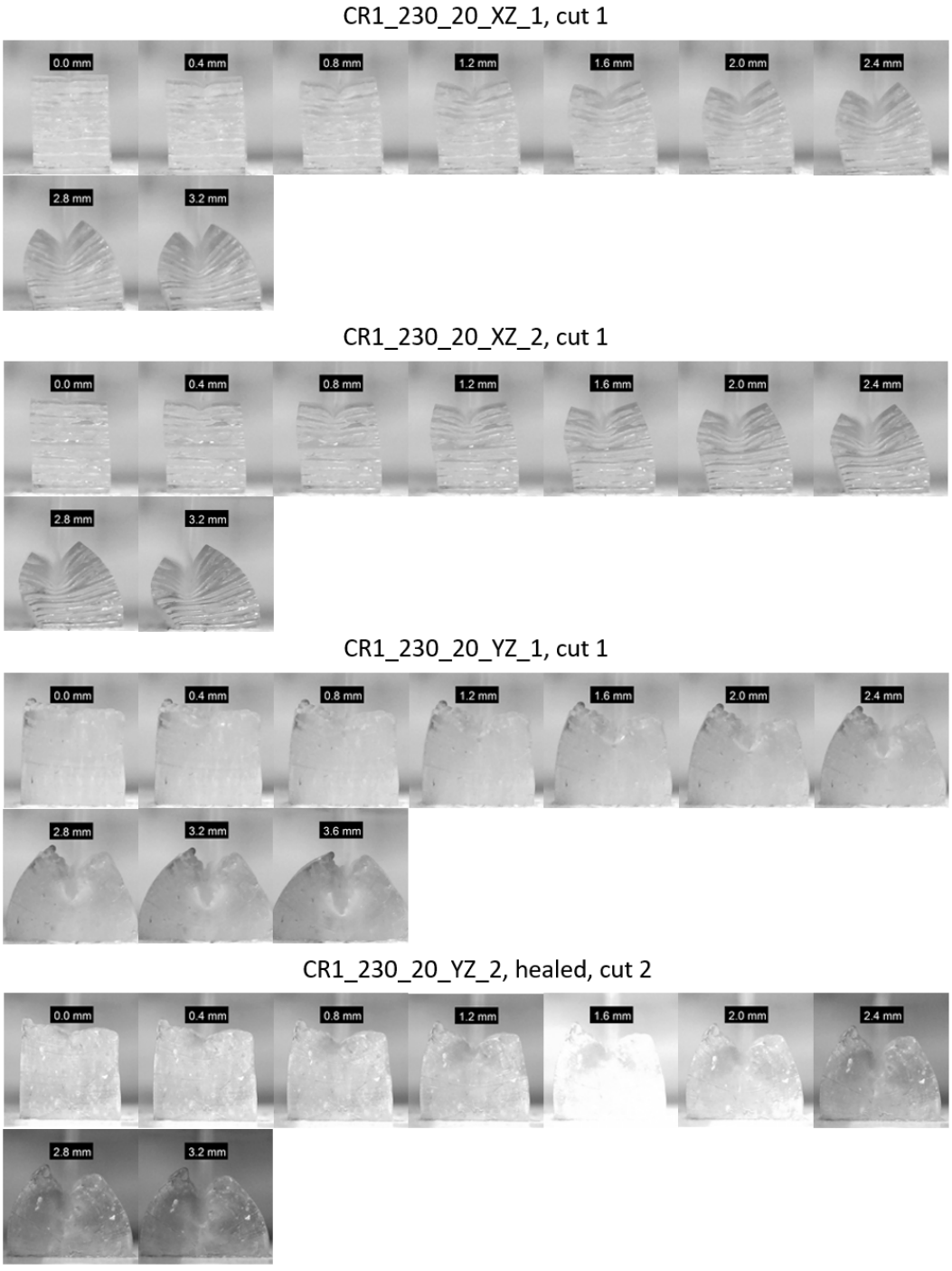


**Figure E.3:** Stills of the first cut test or the 3D printed CR1.

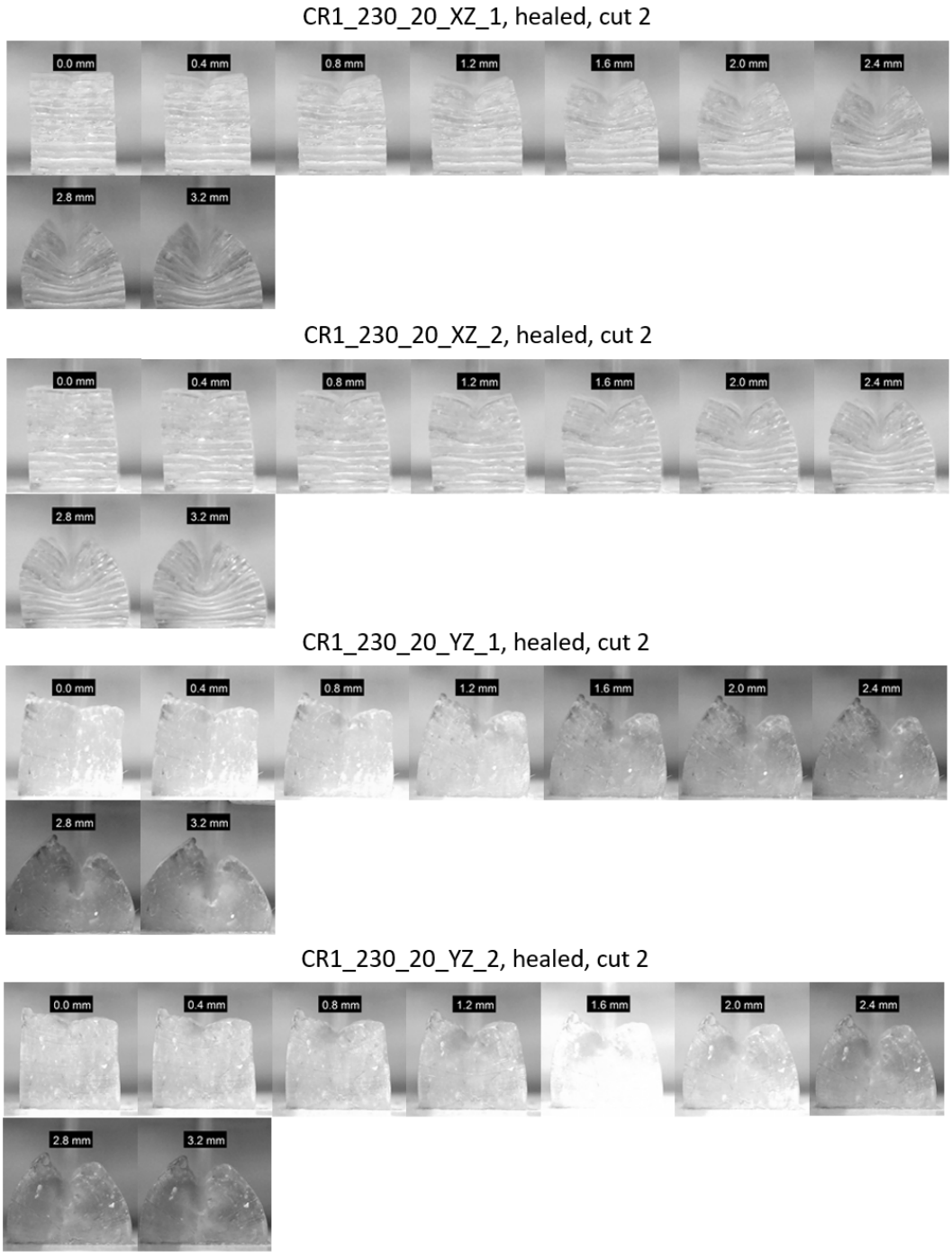


**Figure E.4:** Stills of the cut test or the 3D printed CR1 after healing.

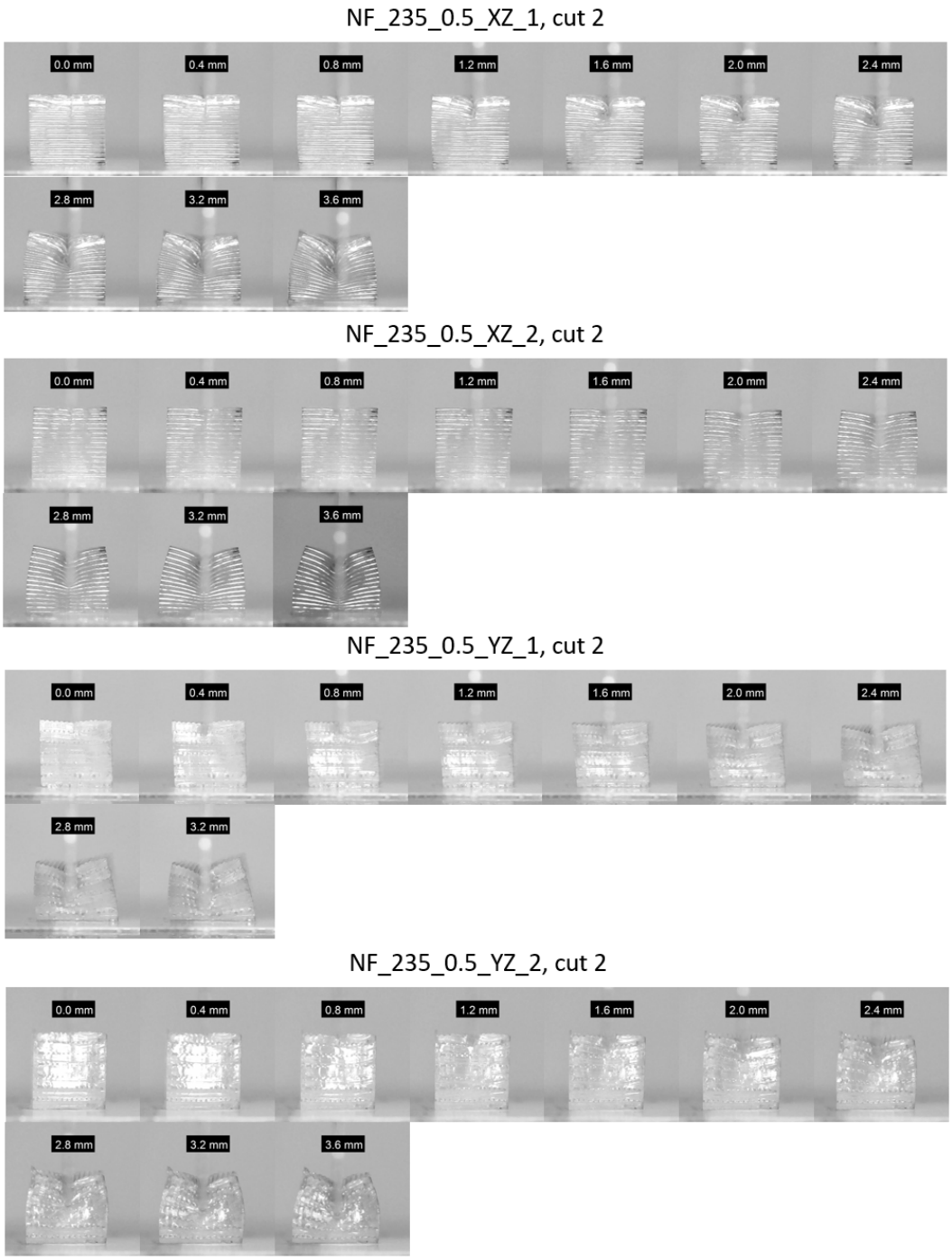


**Figure E.5:** Stills of the cut test or the 3D printed Ninjaflex samples after 'healing'.

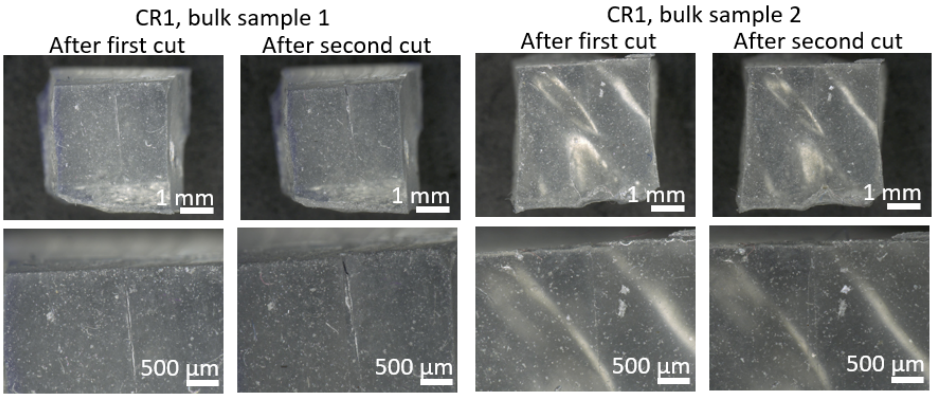


**Figure E.6:** Microscopic pictures of the CR1 bulk samples after first and second cut of the compression cut test.

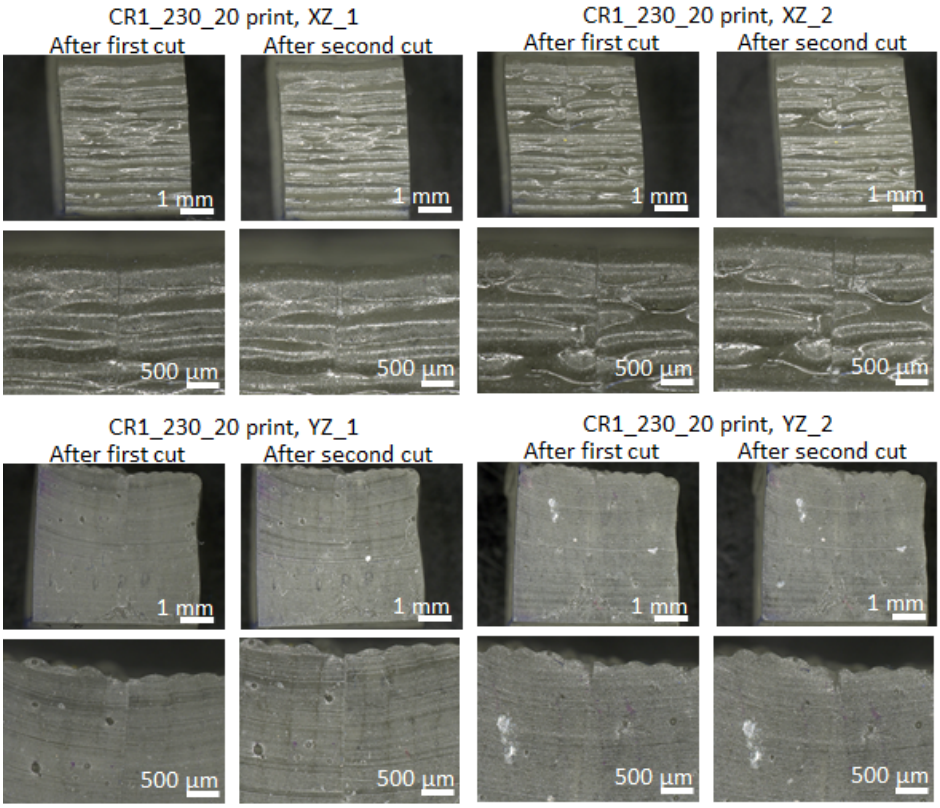


**Figure E.7:** Microscopic pictures of the 3D printed CR1 samples after first and second cut of the compression cut test.

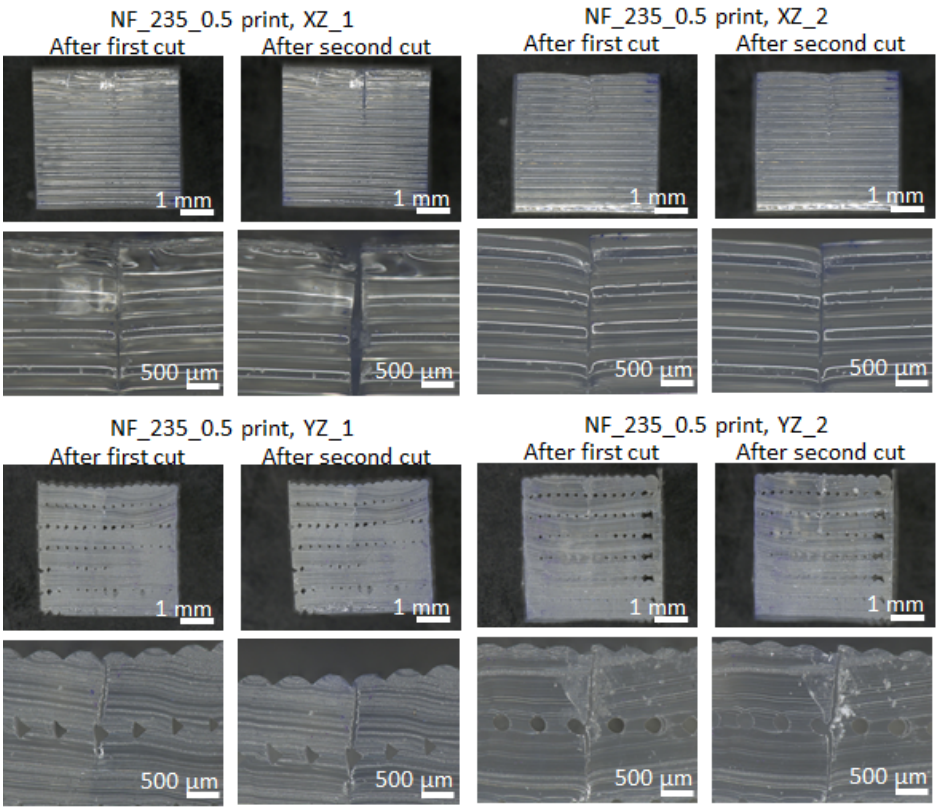


**Figure E.8:** Microscopic pictures of the 3D printed Ninjaflex samples after first and second cut of the compression cut test.